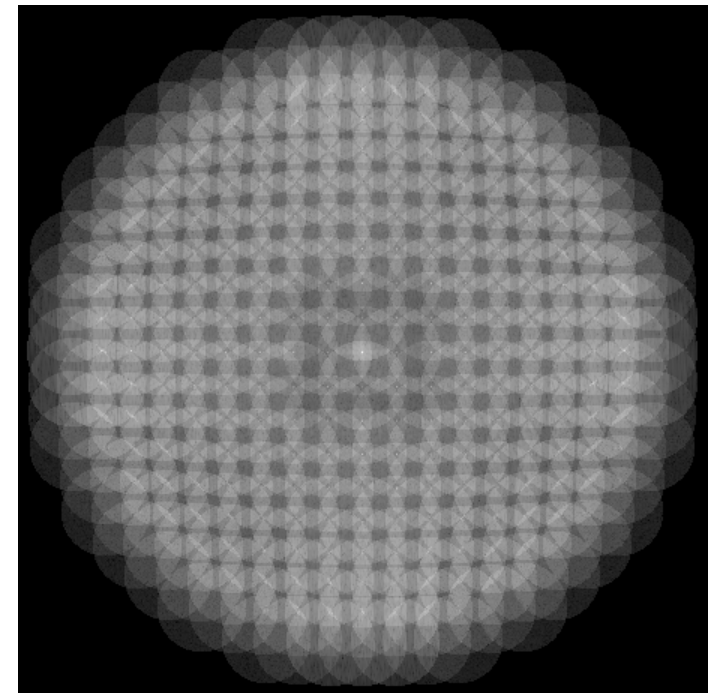Knut Olav Schnell

Fourier ptychography for computationally enhanced imaging in two and three dimensions

June 2019

Master's thesis

Master's thesis

2019

Knut Olav Schnell

NTNU
Norwegian University of
Science and Technology
Faculty of Natural Sciences
Department of Physics

NTNU
Norwegian University of
Science and Technology

NTNU
Norwegian University of
Science and Technology

NTNU
Norwegian University of
Science and Technology

Fourier ptychography for computationally enhanced imaging in two and three dimensions

Knut Olav Schnell

Nanotechnology
Submission date: June 2019
Supervisor: Dag W. Breiby, IFY
Co-supervisor: Muhammad Nadeem Akram, USN

Norwegian University of Science and Technology
Department of Physics

Summary

Fourier ptychography (FP) is a recently developed computational imaging technique that is able to extend the capabilities of a conventional optical microscope beyond the classical limit set by the applied optics hardware. FP effectively decouples the trade-off between field of view (FoV) and resolution, by using multiple low-resolution images with different illumination angles to synthesize a wide FoV high-resolution image with recovered phase information. FP has potential applications in biomedical sciences, where high space-bandwidth product (SBP) imaging systems are needed.

A custom-built Fourier ptychographic microscope (FPM) has been demonstrated to provide the expected resolution gain, by imaging a resolution test target. Using an objective with a 0.055 numerical aperture (NA) combined with illumination angles up to $21.1°$, the FPM achieves a full-pitch resolution of $1.56\,\mu\mathrm{m}$ with an illumination wavelength of $520\,\mathrm{nm}$. The resolution enhancement corresponds to increasing the NA of the system to 0.33.

The FPM has also been shown to be capable of quantitative phase imaging (QPI), by imaging known phase objects. However, faithfully reconstructing steep phase gradients and low-frequent phase information has proved to be challenging, and these limitations have been analyzed and discussed. A large FoV reconstruction of a $4\,\mu\mathrm{m}$ thick bone and cartilage sample has been performed to demonstrate a potential application of the microscope.

FP can also be used for 3D imaging. Here, a multislice approach is adopted to model a 3D sample, and an existing multislice FP algorithm has been implemented and tested. A modified version of the multislice FP algorithm is proposed, based on an imaging model with less approximations. Reconstructions performed with the proposed modifications demonstrate better convergence properties and reduced noise compared to the original algorithm, indicating that the proposed modification improves the performance of the multislice FP algorithm.

Sammendrag

(Norwegian summary)

Fourierptykografi (FP) er en nylig utviklet beregningsbasert avbildningsteknikk som kan forbedre egenskapene til et konvensjonelt optisk mikroskop utover de klassiske grensene som bestemmes av de optiske komponentene mikroskopet er satt sammen av. FP bryter effektivt sett koblingen mellom synsfelt (FoV) og oppløsning, ved å bruke flere lavoppløste bilder med ulike belysningsvinkler til å syntetisere et høyoppløst bilde med stort FoV og rekonstruert faseinformasjon. FP har potensielle bruksområder i biomedisinsk vitenskap, hvor avbildningssystemer med høy informasjonskapasitet trengs.

Et fourierptykografisk mikroskop (FPM) er konstruert, og det er vist at avbildningsteknikken forbedrer oppløsningen i samsvar med de forventede verdiene. Med et mikroskopobjektiv med $0{,}055$ numerisk aperture (NA), og belysningsvinkler opp til $21{,}1°$, oppnås en oppløsning på $1{,}56\,\mu m$ med belysning med bølgelengde $520\,nm$. Forbedringen i oppløsning tilsvarer å utvide NA for avbildningssystemet til $0{,}33$.

Det har også blitt demonstrert at mikroskopet er i stand til å rekonstruere fasen til det avbildede objektet kvantitativt, ved å avbilde kjente faseprøver. Det har vist seg å være utfordrende å rekonstruere bratte fasegradienter og lavfrekvent faseinformasjon. Disse begrensingene har blitt analysert og diskutert. En rekonstruksjon med stort FoV av en bein- og brusk-prøve har blitt gjort, for å demonstrere et potensielt bruksområde for mikroskopet.

FP kan også brukes for 3D-avbildning. Her har en multilags-modell blitt brukt for å beskrive en 3D-prøve, og en eksisterende algoritme har blitt implementert og testet. En modifisert versjon av multilags-FP er foreslått, basert på en avbildningsmodell med færre approksimasjoner. Rekonstruksjoner utført med de foreslåtte endringene viser forbedret konvergens og mindre støy sammenlignet med den opprinnelige versjonen av algoritmen. Dette indikerer at den foreslåtte endringen forbedrer ytelsen til multilags-FP-algoritmen.

Preface

This Master's thesis was written in partial fulfillment of a Master of Science (M.Sc.) degree in Nanotechnology, from the Norwegian University of Science and Technology (NTNU). The thesis is the concluding part the five year MTNANO study programme, with a specialization in nanoelectronics.

The reader is expected to be familiar with complex arithmetic and Fourier theory, as well as fundamentals of electromagnetism and wave theory. Additional relevant theory is introduced and discussed in the thesis.

Trondheim, June 1, 2019

Knut Olav Schnell

Contents

List of Tables

List of Figures

Abbreviations

AS	=	Angular spectrum
BF	=	Bright field
CTF	=	Coherent transfer function
DF	=	Dark field
DFT	=	Discrete Fourier transform
DoF	=	Depth of field
EPRY	=	Embedded pupil function recovery
FFT	=	Fast Fourier transform
FoV	=	Field of view
FP	=	Fourier ptychography
FPDT	=	Fourier ptychographic diffraction tomography
FPM	=	Fourier ptychographic microscope
FPT	=	Fourier ptychographic tomography
HDR	=	High dynamic range
LED	=	Light emitting diode
NA	=	Numerical aperture
OA	=	Optical axis
OPD	=	Optical path difference
OPL	=	Optical path length
OTF	=	Optical transfer function
PSF	=	Point spread function
PTF	=	Phase transfer function
QPI	=	Quantitative phase imaging
SBP	=	Space-bandwidth product
SNR	=	Signal-to-noise ratio
SSE	=	Sum of square errors
USAF	=	United States Air Force
WSI	=	Whole slide imaging

Chapter 1

Introduction

In recent years, the formerly established limits of optical imaging systems have been challenged by computational imaging methods [1–7]. Using the computational power of a modern computer, sophisticated algorithms are able to break the trade-off between large field of view (FoV) and high resolution in microscopy [1] and iteratively recover both the amplitude and the phase of optical fields [8].

In this thesis, the main focus is devoted to a computational imaging technique termed Fourier ptychography (FP), first proposed in 2013 by Zheng et al. [1]. With its basis in a lens-less imaging method termed ptychography [3], FP extends the imaging capabilities of a conventional microscope by collecting images with angularly diverse illumination, and iteratively synthesizing a high-resolution complex representation of the object being imaged [1, 8]. The angularly diverse illumination is typically provided using a light emitting diode (LED) matrix, consisting of a grid of partially coherent illumination sources, which replaces the normal illumination source of the microscope [1, 6, 9] — a cheap and relatively simple modification, with no moving parts.

In the years since the first publication, the field of FP has experienced an immense growth, with examples ranging from recovering pupil aberrations [7, 9], digital refocusing and correction of system parameters [10], high-speed quantitative phase imaging (QPI) [11, 12] and single-shot QPI [13], enhancing florescence microscopy [14], as well as three-dimensional imaging techniques [6, 15, 16].

1.1 Motivation

Optical microscopy is a simple and practical imaging method; it requires no a priori knowledge of the sample, little or no sample preparation, samples can be imaged in air or a solvent, so one does not have to worry about the sample surviving in a vacuum chamber, and it is a fast way of acquiring more knowledge about your sample. However, a microscope

using visible light of wavelength λ is subject to the well-known Rayleigh resolution limit,

$$\delta r = \frac{0.61\lambda}{NA_{\text{obj}}} \tag{1.1}$$

where δr is the minimum resolvable distance, and NA_{obj} is the numerical aperture (NA) of the microscope objective [17]. Increasing the NA of the objective will improve the resolution, and make smaller features visible, but an increase in the NA will also reduce the FoV of the microscope. Thus, one needs to choose either a good resolution, or a wide FoV. This trade-off is quantified in the space-bandwidth product (SBP), the product between the observable area of the sample with the collected bandwidth in the frequency domain.

FP is capable of breaking the link between FoV and resolution, by using a low-NA objective to capture multiple images with a large FoV, and taking advantage of the high-frequent information from high-angle illumination to synthesize a high resolution map of the sample. Thus, the SBP is increased beyond the normal limits. High-SBP imaging is desirable in biomedical sciences [1], for example. In the field of digital pathology, whole slide imaging (WSI), i.e. mechanically scanning the microscopy slide to acquire images of multiple sections and then patching the sections together [18], is an increasingly popular imaging method [18], demonstrating the need for high-SBP imaging systems. With the FP technique, high-SBP images can be obtained without any mechanical scanning [19], making FP a suitable choice for digital pathology. Another application for FP is large-scale cell screening, where a large number of cells are studied (typically $> 10^6$) [20], introducing the need for a large FoV in high-resolution imaging systems.

Another key feature of FP is the quantitative phase retrieval. The phase of an optical field describes how the light is delayed when propagating through an object. As optical detectors only measure the intensity of the incoming light, the phase information is lost in conventional microscopy. The need to observe phase objects, i.e. objects that do not absorb light (they are transparent), yet only delays it, prompted the invention of the Zernike phase contrast microscope in 1934 [21]. Phase contrast microscopes have found many applications, but an important limitation is the lack of quantitativity; the resulting images highlight the regions where the light has been delayed, but they cannot be used to determine how much it has been delayed [22].

For both diagnostic and therapeutic purposes, knowledge of the optical properties of biological tissues is vital [23]. Using a QPI technique to create accurate and quantitative phase maps of a thin object, allows calculating important optical parameters from the phase map [24], such as scattering rates, anisotropy factors and the real part of the refractive index.

A conventional microscope produces a 2D image of the sample. While a 2D image is sufficient in many cases, the object being imaged may have a 3D structure, and a 2D approximation may be inadequate [6, 25, 26]. For such samples, 3D imaging techniques are needed. 3D ptychography [5, 27], optical tomography [28], multiphoton microscopy [29], light-sheet-based microscopy [30], as well as confocal microscopy [31] are techniques that permit 3D microscopy. However, all the mentioned techniques require mechanical scanning or rotation of the sample (or the detector/illumination) to acquire the 3D information, limiting the speed of acquisition as well as introducing uncertainties in motor positions, etc. 3D FP uses only angularly diverse illumination to extract the 3D information. Using a

static LED matrix to provide the illumination, the acquisition speed is simply limited by the readout speed of the camera.

1.2 Aim of work

The aim of this project is building and implementing a Fourier ptychographic microscope (FPM) platform, capable of surpassing the limits of the applied optics. The microscope is intended to be an asset for the X-ray group at NTNU. In this project, the quantitativity of recovered phase information will be tested, and the observed resolution enhancement compared to the theoretically expected values.

In addition, the FPM platform will be demonstrated on a 2D biological sample, to highlight potential applications of the technique, and demonstrate the benefits of FP imaging.

A modification to an existing 3D FP algorithm is proposed. The algorithm is based on a multislice model for the 3D sample, using concepts similar to 3D ptychography [32]. The project aims to determine the fitness of this modified algorithm compared to the original version.

1.3 Thesis structure

First, the theoretical foundation for FP imaging is presented and discussed, important concepts being propagation of light, the concept of coherence, and modeling the imaging process. Thereafter, the inner workings of FP techniques are presented, both for 2D and 3D modalities. A modification to the 3D algorithm is proposed, based on the previously described imaging theory.

Chapter 4 presents the experimental details of the FPM used to collect FP datasets, and also addresses sampling requirements and other concerns related the the discretization of the algorithms necessary to implement them on a computer. The subsequent chapter presents the results obtained using the FPM, as well as results based on open source datasets of a quasi-3D sample. The performances of the reconstruction algorithms are compared to the theoretically expected results, and compared with other imaging models.

A conference paper was written and submitted, describing the modified 3D algorithm, and the paper is attached as Appendix A.

1.4 Disclosures

Sections 2.3, 3.1, 4.1, and 4.2.2 were originally written as a part of the author's project thesis (course code TFY4520). The current versions of the sections are modified to reflect the theme of this thesis.

Figures appearing in this thesis have been created and/or edited using Inkscape [33] and ImageJ [34]. Plots have been created using Matlab [35].

Chapter 2

Wave optics and imaging theory

This chapter will present a theoretical background for FP, starting the description with fundamental wave optics, origination from Maxwell's equations and the scalar formulation of wave optics. Important concepts, such as coherence and optical imaging will be discussed.

2.1 Fundamental wave optics

2.1.1 Maxwell's equations

Maxwell's equations serve as a fundament for the theory of wave optics [17]. With the electric field and magnetic field given by $\mathcal{E}$ and $\mathcal{H}$, respectively, Maxwell's equations are

$$\nabla \times \mathcal{E} = -\mu \frac{\partial \mathcal{H}}{\partial t} \tag{2.1a}$$

$$\nabla \times \mathcal{H} = \epsilon \frac{\partial \mathcal{E}}{\partial t} \tag{2.1b}$$

$$\nabla \cdot \epsilon \mathcal{E} = 0 \tag{2.1c}$$

$$\nabla \cdot \mu \mathcal{H} = 0, \tag{2.1d}$$

in a medium with no free charges, where ϵ and μ respectively denote the electric permittivity and magnetic permeability, ∇ being the vectorial differential operator, and t being the time coordinate [17, 21]. Both $\mathcal{E}$ and $\mathcal{H}$ are vectorial quantities, so $\mathcal{E}$ can be expressed as $\mathcal{E}_x \hat{\mathbf{x}} + \mathcal{E}_y \hat{\mathbf{y}} + \mathcal{E}_z \hat{\mathbf{z}}$, with $\hat{\mathbf{x}}$, $\hat{\mathbf{y}}$ and $\hat{\mathbf{z}}$ being Cartesian unit vectors.

From Maxwell's equations and known vector identities, it is possible to derive a wave equation for the electric field, namely [17]

$$\nabla^2 \mathcal{E} - \frac{n^2}{c^2} \frac{\partial^2 \mathcal{E}}{\partial t^2} = 0, \tag{2.2}$$

where the refractive index, n, is given by $\sqrt{\epsilon/\epsilon_0}$ and the speed of light, c, is defined as $(\mu_0 \epsilon_0)^{-1/2}$, and $\nabla^2 = \nabla \cdot \nabla$. An equivalent equation can be derived for the $\mathcal{H}$ field, but the derivation has been left out for the sake of simplicity.

Equation (2.2) must hold for each of the vector components of the $\mathcal{E}$ field. An important approximation that is made in the rest of the thesis is the *scalar approximation*: the vectorial nature of the fields are ignored, and a single, scalar, equation is used to treat all the components of the $\mathcal{E}$ and $\mathcal{H}$ fields [17], namely

$$\nabla^2 u - \frac{n^2}{c^2}\frac{\partial^2 u}{\partial t^2} = 0, \tag{2.3}$$

where $u = u(\mathbf{r}, t)$ represents an arbitrary field component, with $\mathbf{r}$ being the spatial coordinate.

2.1.2 Helmholtz equation

Assuming a sinusoidal time dependence of the electromagnetic field and monochromatic light, u can be generally expressed as

$$u(\mathbf{r}, t) = A(\mathbf{r})\cos(\omega t + \phi), \tag{2.4}$$

where ω is the temporal angular frequency of the wave, A is the real-valued amplitude and ϕ is a phase offset. A frequency of ω corresponds to a free-space wavelength (i.e. in vacuum) of $\lambda = 2\pi c/\omega$. This wave can be represented using phasor notation [17],

$$U(\mathbf{r}) = A(\mathbf{r})e^{i\phi}, \tag{2.5}$$

so that

$$u(\mathbf{r}) = \text{Re}\left\{U(\mathbf{r})e^{iwt}\right\}, \tag{2.6}$$

where $\text{Re}\{\cdot\}$ denotes the real part. Inserting this into Equation (2.3), yields a famous result known as the Helmholtz equation [17]:

$$(\nabla^2 + k^2)U(\mathbf{r}) = 0, \tag{2.7}$$

where $k = \omega n/c = nk_0$ is the angular wave number of the wave. k_0 denotes the free-space wave number.

2.1.3 Phase and optical path length

The phase, ϕ, of a field described by the phasor U, as given by Equation (2.5), can be computed from U as [36]

$$\phi = \arg U = \tan^{-1}\left[\frac{\text{Im}\{U\}}{\text{Re}\{U\}}\right], \tag{2.8}$$

where $\arg$ is short for argument.

A concept closely linked to the phase of a wave field is the optical path length (OPL). The speed of light in a medium with refractive index n is given by c/n. The OPL accounts for the varying speed of light, as it represents the path distance in vacuum equivalent to the
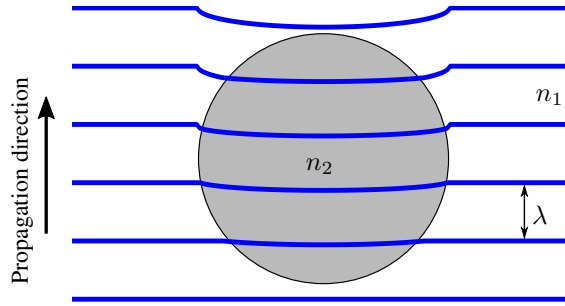
Figure 2.1: Phase delay from transmission through sphere, when the sphere has a higher refractive index than the medium, $n_2 > n_1$. The blue lines represent the wavefronts, separated by the wavelength, λ.

distance traveled in a medium [21]. For light following a curve $\mathcal{C}$, the OPL, denoted Λ, is given by [21]

$$\Lambda = \int_{\mathcal{C}} n \, \mathrm{d}s \,, \tag{2.9}$$

where $\mathrm{d}s$ is the differential line element and n is the position-dependent refractive index. Retaining the assumption of monochromatic light with wavelength, λ, a wave following the path $\mathcal{C}$ will acquire a phase [21]

$$\phi = \frac{2\pi}{\lambda} \Lambda = k_0 \Lambda, \tag{2.10}$$

where the initial phase of the wave is assumed to be 0.

The example in Figure 2.1 shows how the wavefront of a plane wave is modulated when traversing through a spherical object with slightly higher refractive index than the surrounding medium. This modulation is a result of different OPLs for the path through the sphere and the path outside the sphere. If the diameter of the sphere is given by d, the OPL of the path through the middle of the sphere is $\Lambda_2 = n_2 d$, while the OPL outside the sphere is $\Lambda_1 = n_1 d$. The two paths have different OPLs, resulting in an optical path difference (OPD), denoted $\Delta\Lambda$, of

$$\Delta\Lambda = \Lambda_1 - \Lambda_2 = (n_1 - n_2)d. \tag{2.11}$$

Similarly, the phase difference, $\Delta\phi$, between the two paths is

$$\Delta\phi = k_0 \Delta\Lambda. \tag{2.12}$$

The OPL perspective provides a simple model for calculating the phase modulation resulting from transmission through an object. However, for a more complete model of transmission, one needs to account for *diffraction*.

2.1.4 Diffraction

Diffraction may be described as the "deviation of light from rectilinear propagation"[21]. In the theory regarding diffraction, an important foundation is the *Huygens-Fresnel principle*, which states
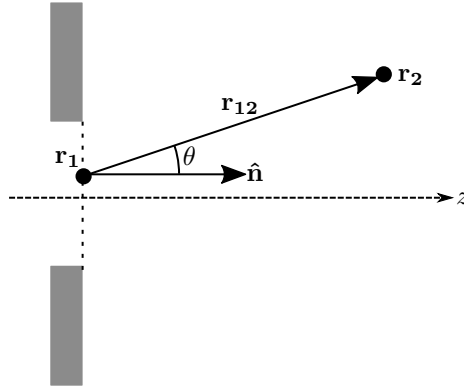
Figure 2.2: Schematic explanation of the vectorial quantities of the Rayleigh-Sommerfeld formulation.

> Every unobstructed point of a wavefront, at a given instant, serves as a source
> of spherical secondary wavelets (with the same frequency as that of the pri-
> mary wave). The amplitude of the optical field at any point beyond is the
> superposition of all these wavelets (considering their amplitudes and relative
> phases). [21]

The *Rayleigh-Sommerfeld formulation of diffraction* is a mathematical treatment of the Huygens-Fresnel principle [17]. The key result of the theory (the first Sommerfeld solution) can be expressed compactly as [17, 37]

$$U(\mathbf{r_2}) = -\frac{1}{2\pi} \iint\limits_{S} U(\mathbf{r_1}) \left(ik - \frac{1}{r_{12}} \right) \frac{e^{ikr_{12}}}{r_{12}} \cos\theta \, \mathrm{d}S \,, \tag{2.13}$$

where $\mathbf{r_2}$ is the observation point, $\mathbf{r_1}$ is a point in the plane denoted by S, and r_{12} is the distance between these points. θ is the angle between $\mathbf{r_0}$ and the plane normal, $\hat{\mathbf{n}}$. See figure 2.2 for a graphical explanation of the different quantities. Equation (2.13) expresses the field at a point $\mathbf{r_2}$ as a function of the field distribution across S. This implies that if the field is known across S, it can be calculated at an arbitrary position (assuming that no other sources contribute to the field at this position).

2.2   Propagation

Equation (2.13) expresses how an electromagnetic field propagates through free space. Assuming the optical axis is the $\hat{\mathbf{n}}$-direction, and that the z-axis is parallel to $\hat{\mathbf{n}}$, one may rewrite (2.13) in Cartesian coordinates to explicitly express the field at an arbitrary z-position, U_2, as a function of the field at $z = 0$, U_1 [17]:

$$U_2(x,y) = -\frac{z}{2\pi} \int\limits_{-\infty}^{\infty}\!\!\!\int U_1(\xi,\eta) \left(ik - \frac{1}{r_{12}} \right) \frac{e^{ikr_{12}}}{r_{12}^2} \, \mathrm{d}\xi \, \mathrm{d}\eta \,, \tag{2.14}$$

where $\cos\theta$ has been rewritten as z/r_{12}, (ξ, η) are the coordinates in the $z = 0$ plane, and r_{12} is given by

$$r_{12} = \sqrt{z^2 + (x - \xi)^2 + (y - \eta)^2}. \tag{2.15}$$

The integral limits have also been changed from the limited source area S to infinity, to account for sources across the entire xy plane.

However, using Equation (2.14) directly in computational optics is time-consuming, and faster methods are needed.

2.2.1 Angular spectrum method

The angular spectrum method may be derived using Fourier theory and the Helmholz equation (see ref. [17]), but here it will be derived from Equation (2.14). The first step is recognizing (2.14) as a 2D convolution of U_1 with some h_{AS}, defined as [17]

$$h_{AS}(x, y) = \frac{z}{2\pi}\left(\frac{1}{r_{12}} - ik\right)\frac{e^{ikr}}{r^2}, \tag{2.16}$$

where $r = \sqrt{z^2 + x^2 + y^2}$. With these definitions, U_2 may be expressed as [17]

$$U_2(x, y) = \iint\limits_{-\infty}^{\infty} U_1(\xi, \eta)h(x - \xi, y - \eta)\,\mathrm{d}\xi\,\mathrm{d}\eta \equiv U_1(x, y) \circledast h(x, y), \tag{2.17}$$

where $\circledast$ denotes the 2D convolution operation. Applying the convolution theorem of Fourier theory [36], one may reformulate the convolution operation as [37]

$$U_2(x, y) = \mathcal{F}^{-1}\left\{\mathcal{F}\left\{U_1(x, y)\right\} H_{AS}(f_x, f_y)\right\}. \tag{2.18}$$

where $H_{AS}(f_x, f_y) = \mathcal{F}\left\{h_{AS}(x, y)\right\}$, and $\mathcal{F}\{\cdot\}$ and $\mathcal{F}^{-1}\{\cdot\}$ respectively denote the 2D Fourier transform and inverse Fourier transform. (f_x, f_y) are the spatial frequency coordinates[1], defined implicitly through the definition of the 2D Fourier transform [17]:

$$\mathcal{F}\left\{f(x, y)\right\} = \iint\limits_{-\infty}^{\infty} f(x, y)\exp\{i2\pi(f_x x + f_y y)\}\,\mathrm{d}x\,\mathrm{d}y, \tag{2.19}$$

which is provided for clarity, as multiple definitions exist. The transfer function, H_{as}, can be found analytically by calculating the Fourier transform of h_{AS} [17]:

$$H_{AS}(f_x, f_y) = \mathcal{F}\left\{h(x, y)\right\} = \exp\left(ikz\sqrt{1 - (\lambda f_x)^2 - (\lambda f_y)^2}\right). \tag{2.20}$$

An important quality of the angular spectrum method, is that no additional approximations are made, i.e. the propagation formulation is valid for arbitrarily small values of z, and is thus suitable when small propagation distances are needed.

---

[1]Linear frequency coordinates, (f_x, f_y), will be used interchangeably with angular frequency coordinates, (k_x, k_y), and the relationship between the two paradigms is $(k_x, k_y) = 2\pi(f_x, f_y)$.

2.2.2 Fresnel propagation

Assuming $r_{12} \gg \lambda$, the Rayleigh-Sommerfeld diffraction solution, Equation (2.14), simplifies to

$$U_2(x,y) = \frac{z}{i\lambda} \iint\limits_{-\infty}^{\infty} U_1(\xi,\eta) \frac{e^{ikr_{12}}}{r_{12}^2} \, \mathrm{d}\xi \, \mathrm{d}\eta \,, \tag{2.21}$$

The Fresnel approximation regards eliminating the square root expression for r_{12} [37] using a Taylor series expansion to the first order for the square root [38]:

$$\sqrt{1+x} \approx 1 + \frac{1}{2}x. \tag{2.22}$$

Using this approximation in Equation (2.15) yields [37]

$$r_{12} \approx z \left[1 + \frac{1}{2} \left(\frac{x-\xi}{z} \right)^2 + \frac{1}{2} \left(\frac{y-\eta}{z} \right)^2 \right]. \tag{2.23}$$

The given approximation is inserted into Equation (2.14) to obtain an approximate propagation formula. In the denominator of the integrand, the r_{12}^2 term is approximated even more crudely, as $r_{12}^2 = z^2$, since the error introduced by this is small in general [17]. The resulting formula describing Fresnel propagation is [17]

$$U_2(x,y) = \frac{e^{ikz}}{i\lambda z} \iint\limits_{-\infty}^{\infty} U_1(\xi,\eta) \exp\left\{ i\frac{k}{2z} \left[(x-\xi)^2 + (y-\eta)^2 \right] \right\} \mathrm{d}\xi \, \mathrm{d}\eta \,. \tag{2.24}$$

The Fresnel approximation is valid as long as [17]

$$z^3 \gg \frac{\pi}{4\lambda} \left[(x-\xi)^2 + (y-\eta)^2 \right]_{\mathrm{max}}^2 \,, \tag{2.25}$$

where $[\cdot]_{\mathrm{max}}$ indicates the maximum value of the expression within the brackets.

Equation (2.24) can, in a similar fashion to the angular spectrum method, be interpreted as a convolution of U_i with another function h_{Fres} given by [17]

$$h_{\mathrm{Fres}}(x,y) = \frac{e^{ikz}}{i\lambda z} \exp\left[i\frac{k}{2z}(x^2+y^2) \right] \tag{2.26}$$

and the corresponding transfer function H_{Fres}, found by Fourier transforming h_{Fres} [17]

$$H_{\mathrm{Fres}}(f_x, f_y) = e^{ikz} \exp\left[-i\pi\lambda z(f_x^2 + f_y^2) \right]. \tag{2.27}$$

Using the transfer function, propagation with the Fresnel approximation may be described as

$$U_2(x,y) = \mathcal{F}^{-1} \left\{ \mathcal{F} \left\{ U_1(x,y) \right\} H_{\mathrm{Fres}}(f_x, f_y) \right\}. \tag{2.28}$$

This approach to propagation will be described as *Fresnel transfer function propagation*.

Another approach to simplify Equation (2.24) is by moving the *quadratic phase exponential*, $\exp\left[ik/2z\left(x^2 + y^2\right)\right]$, outside of the integral [17], yielding

$$
U_2(x, y) = \frac{e^{ikz}}{i\lambda z} \exp\left[i\frac{k}{2z}(x^2 + y^2)\right] \times
$$

$$
\int\!\!\!\int\limits_{-\infty}^{\infty} U_1(\xi, \eta) \exp\left[i\frac{k}{2z}(\xi^2 + \eta^2)\right] \exp\left[-i\frac{2\pi}{\lambda z}(x\xi + y\eta)\right] \mathrm{d}\xi\,\mathrm{d}\eta. \quad (2.29)
$$

Substituting with $(f_x, f_y) \leftarrow (x/\lambda z\ ,\ y/\lambda z)$ reveals that the integral is a Fourier transform of the input field multiplied with a quadratic phase exponential [17]. With this realization, Equation (2.29) can be reformulated as

$$
U_2(x, y) = \frac{e^{ikz}}{i\lambda z} \exp\left[i\frac{k}{2z}(x^2 + y^2)\right] \times
$$

$$
\mathcal{F}\left\{U_1(\xi, \eta) \exp\left[i\frac{k}{2z}(\xi^2 + \eta^2)\right]\right\}\Bigg|_{\substack{f_x = x/z\lambda \\ f_y = y/z\lambda}} \quad (2.30)
$$

Throughout this thesis, the approach described by Equation (2.30) will be termed *Fresnel transform propagation*. A notable advantage of (2.30), compared to the angular spectrum method, is that only a single Fourier transform is necessary. The drawback is that $r_{12} \gg \lambda$ is assumed, so (2.30) is not valid for short propagation distances.

2.2.3 Fraunhofer propagation

The Fraunhofer approximation is a further approximation of the Fresnel transform propagation, given by Equation (2.30). If

$$
z \gg \frac{k}{2}[\xi^2 + \eta^2]_{\max}, \quad (2.31)
$$

then the exponential expression inside the integrand in Equation (2.30) will be ~ 1 over the integration range, resulting in the *Fraunhofer propagation formula* [17]

$$
U_2(x, y) = \frac{e^{ikz}}{i\lambda z} \exp\left[i\frac{k}{2z}(x^2 + y^2)\right] \mathcal{F}\left\{U_1(\xi, \eta)\right\}\Bigg|_{\substack{f_x = x/z\lambda \\ f_y = y/z\lambda}}. \quad (2.32)
$$

Equation (2.32) shows that in the Fraunhofer region, i.e. for the z values fulfilling the inequality given in Equation (2.31), the field is proportional to the Fourier transform of the input field, multiplied by a phase factor.

The Fraunhofer approximation criterion, Equation (2.31), sometimes demands large observation distances to hold. A numerical example illustrates the criterion better: using green light with $\lambda = 520\,\mathrm{nm}$ and considering a circular region in the object plane with a radius of $100\,\mathrm{\mu m}$, the Fraunhofer criterion states $z \gg 12\,\mathrm{cm}$. As microscope objectives often have working distances below $5\,\mathrm{cm}$, the criterion is clearly not fulfilled in this example. However, the condition for Fresnel diffraction, Equation (2.25), is fulfilled much more

easily, and will in this case be $z^3 \gg 1\,\mathrm{cm}^3$, assuming a lens diameter of $1\,\mathrm{cm}$. Note that the approximations may yield appropriate results even if the conditions are not completely met [17]. This example illustrates that the Fresnel formulation of diffraction may be a more suitable choice to model imaging with a microscope.

2.3 Coherence

Ideal optics are often split into two disciplines: coherent and incoherent. However, the electromagnetic fields produced by real radiation sources are often found somewhere between these two regimes [21]. This section will proceed to quantify the degree of coherence for an electromagnetic field.

For illumination described by an electric field, $E(\mathbf{x}, t)$, propagating in the z-direction, with $\mathbf{x} = (x, y)$ being the coordinates in the transversal plane and t being the time, the mutual coherence function is defined as [39–41]

$$\Gamma(\mathbf{x_1}, \mathbf{x_2}, \tau) = \langle E(\mathbf{x_1}, t + \tau) E^*(\mathbf{x_2}, t) \rangle_T, \tag{2.33}$$

where * denotes the complex conjugate and $\langle \cdot \rangle_T$ the average over some time interval, T, which is long compared to the coherence time (defined later). τ denotes a time difference. The complex degree of coherence, γ, is the normalized mutual coherence function [21, 40]

$$\gamma(\mathbf{x_1}, \mathbf{x_2}, \tau) = \frac{\Gamma(\mathbf{x_1}, \mathbf{x_2}, \tau)}{\sqrt{I(\mathbf{x_1}, t) I(\mathbf{x_2}, t)}}, \tag{2.34}$$

where $I(\mathbf{x}, t) = \Gamma(\mathbf{x}, \mathbf{x}, 0)$ denotes the intensity of the radiation[2]. Completely coherent illumination is described by $|\gamma(\mathbf{x_1}, \mathbf{x_2}, \tau)| = 1$, while incoherent illumination is characterized by $|\gamma(\mathbf{x_1}, \mathbf{x_2}, \tau)| = 0$ [21]. For $0 < |\gamma(\mathbf{x_1}, \mathbf{x_2}, \tau)| < 1$, the field is described as *partially coherent*.

Coherence theory is often divided into two classes of coherence, *temporal* and *spatial* [21]. Temporal coherence is described by $\gamma(0, 0, \tau)$, while $\gamma(\mathbf{x_1}, \mathbf{x_2}, 0)$ describes spatial coherence [40]. It should be noted that splitting the coherence function in a temporal and a spatial part is an approximation.

2.3.1 Temporal Coherence

The temporal (or longitudinal) part of the normalized coherence function, $\gamma(0, 0, \tau)$, may be interpreted as the autocorrelation of the electric field. It describes to which degree the phase relationship between the electric field at two different times is preserved [40]. Temporal coherence is characterized by the coherence time, t_c, describing how long time the phase relationship is expected to remain constant. The coherence time is calculated from the degree of coherence as

$$t_c = \int_{-\infty}^{\infty} |\gamma(0, 0, \tau)|^2 \, d\tau. \tag{2.35}$$

---

[2]Some multiplicative factors have been left out in the expression for the intensity, as they are not of interest in this project.

The coherence time is related to the the frequency spread of the radiation source, $\Delta\nu$, which is important, as real radiation sources never are completely monochromatic [21, 40]. This relationship is approximately given by [21]:

$$t_{\mathrm{c}} \approx \frac{1}{\Delta\nu}. \tag{2.36}$$

For a quasimonochromatic source, i.e. a source where $\Delta\nu$ is much smaller than the mean frequency of the source, $\bar{\nu}$, the coherence time may be interpreted as the average period that the electric field oscillates sinusoidally with a certain frequency [21].

The coherence length, l_{c}, describes the spatial distance, over which the phase of the light is expected to remain correlated [21]. It is related to the coherence time through

$$l_{\mathrm{c}} = c t_{\mathrm{c}}, \tag{2.37}$$

where c is the speed of light and a refractive index of $n = 1$. has been assumed. Combining (2.37) with $\lambda = c/\nu$, and Equation (2.36), a first order relation between the wavelength spread, $\Delta\lambda$, and $\Delta\nu$ is

$$\Delta\lambda \approx \left|\frac{\partial\lambda}{\partial\nu}\right|_{\nu=\bar{\nu}} \Delta\nu = \frac{c}{\bar{\nu}^2}\bar{\Delta}\nu \approx \frac{\bar{\lambda}^2}{c t_{\mathrm{c}}} = \frac{\bar{\lambda}^2}{l_{\mathrm{c}}} \tag{2.38}$$

where $\bar{\lambda}$ is the average wavelength.

2.3.2   Spatial Coherence

Spatial (or transversal) coherence describes the phase relationship between two points in the transversal plane [40].

The complex degree of spatial coherence, $\gamma(\mathbf{x_1}, \mathbf{x_2}, 0)$, is related to the intensity distribution of the radiation source. According to the van Cittert-Zernike theorem, the complex degree of spatial coherence is given by the normalized Fourier transform of the intensity distribution of the source, when $|\mathbf{x_1} - \mathbf{x_2}|$ and the linear dimensions of the source are small compared to the distance from the radiation source to the considered transversal plane, illustrated by l in Figure 2.3 [21, 41].

A consequence of the van Cittert-Zernike theorem, is that the *area of coherence*, A_{c}, in the xy plane of Figure 2.3 and the emitting area of the radiation source, A_{s}, are approximately related through [21, 39]

$$A_{\mathrm{c}} \approx \frac{l^2 \bar{\lambda}^2}{A_{\mathrm{s}}}, \tag{2.39}$$

where l is the distance from the source and $\bar{\lambda}$ is the average wavelength of the source. Note that A_{c} increases with increasing distance from the source, because at larger distances, the differences in illumination angle from the different points in the source become smaller [21]. This estimate is an important quantity when dealing with partially coherent sources; to be able to treat the illumination as coherent in the xy plane, one has to consider an area that is smaller than A_{c}.

For real illumination sources, such as LEDs, one can measure A_{s}, and use Equation (2.39) to calculate how large an area that may be assumed to be spatially coherent.
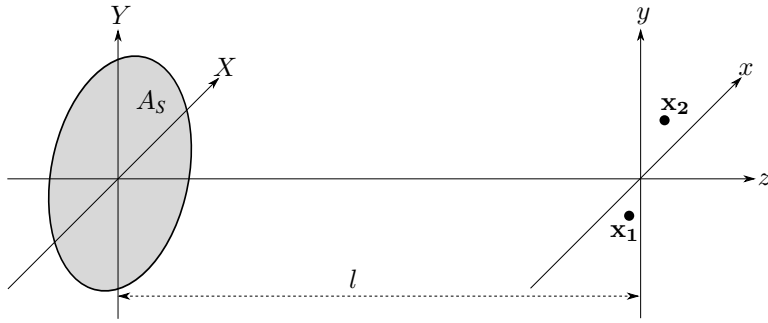
Figure 2.3: Illustration of the important quantities of the van Cittert-Zernike theorem. The figure displays a simple example. The gray area denoted A_s in the XY plane is the emitting area. The degree of coherence is considered in the xy plane, specifically between the points $\mathbf{x_1}$ and $\mathbf{x_1}$.

2.4 Coherent imaging

2.4.1 Multiplicative approximation

In conventional 2D imaging models, the sample may be specified as a 2D complex transmittance $t(x, y)$ [17], where transmission through the sample is modeled as [17]

$$U_o^+(x, y) = t(x, y) U_o^-(x, y), \tag{2.40}$$

where U_o^+ and U_i^- respectively denote the light fields just after and just before the sample. Interpreting t as a phasor $t = |t| e^{\arg(t)}$, it is evident that the phase of the object, $\arg(t)$, accounts for a phase delay of the transmitted field respective to the incoming field, and the amplitude, $|t|$, is understood as an attenuation of the field.

2.4.2 Multislice model

Modeling transmission through a three-dimensional object may be done using a multislice approach [42]. The 3D object is split into a finite number of 2D slices, so that the multiplicative approximation is valid for each slice [5]. To transfer the wave from one slice to the other, a propagation scheme is employed [42]. Let $q_n(x, y)$ describe the nth slice, and $\mathcal{P}_d\{\cdot\}$ denote a free space propagation operation over a distance d in the z-direction. Then, the field just before slice n, f_n, will be given recursively by [6, 42]

$$f_n(x, y) = \mathcal{P}_{\Delta z}\{q_{n-1}(x, y) f_{n-1}(x, y)\}, \quad n = 2, 3, \ldots, N \tag{2.41}$$

where Δz is the distance between two slices, and N is the number of slices. The starting point of the recursion, f_1, is given by the illumination at the input field.

It is also convenient to assign a name to the product of q_n and f_n. In this thesis, this product will be designated g_n, given explicitly by

$$g_n(x, y) = q_n(x, y) f_n(x, y), \quad n = 1, 2, \ldots, N. \tag{2.42}$$

g_n describes the field just after each slice. Note that Equation (2.41) now can be reformulated as

$$f_n(x, y) = \mathcal{P}_{\Delta z}\{g_{n-1}(x, y)\}. \tag{2.43}$$

The angular spectrum method (see subsection 2.2.1) can be derived without assuming $z \gg \lambda$ [17], and is thus a suitable choice of propagation scheme if Δz is small. Then $\mathcal{P}_{\Delta z}\{\cdot\}$ may be expressed explicitly as

$$\mathcal{P}_{\Delta z}\{\cdot\} = \mathcal{F}^{-1}\left\{\exp\left(ik\Delta z\sqrt{1 - (\lambda f_x)^2 - (\lambda f_y)^2}\right)\mathcal{F}\{\cdot\}\right\} \tag{2.44}$$

Equation (2.41) describes a multiply-and-propagate operation [6]: At first, the complex field just before the slice, f_n, is multiplied by the complex transmittance of that slice, q_n, to obtain the field just after the slice, g_n. Then, the propagation operation is applied to g_n, to move the field to the next slice. The field just after the last slice, g_N, will be the exit field of the 3D sample.

In order to compare the resulting field with a field that is obtained using a microscope, the plane of focus becomes an important factor. If the plane of focus is offset from the last slice of the multislice model by z_p, the field observed at the plane of focus will be given by [6]

$$U_o(x, y) = \mathcal{P}_{z_p}\{g_N(x, y)\}, \tag{2.45}$$

where $z_p < 0$ when the plane of focus is within the 3D object.

When $\Delta z \to 0$ and $N \to \infty$, while keeping the product, $\Delta z N$, equal to the thickness of the sample, the multislice model has been shown to be a rigorous model for 3D scattering [42]. However, from a computational perspective, a finite Δz must be selected, introducing an important approximation [42].

Another important limitation of the multislice model, is that it does not account for the backscattered field, since the propagation operation has a designated direction (here: positive z-direction). However, the multislice approach has been shown to accurately model small-angle reflection [43].

Compared to the multiplicative approximation, the multislice model has the important advantage that diffraction effects within the 3D sample is accounted for, through the applied propagation scheme. In addition, multiple scattering events may also be modeled, as the exit field from slice number n, g_n, is used in its entirety as the input field for the next slice through Equation (2.43), i.e. including the scattered components. The number of potential scattering events in the model is then the same as the number of slices, N.

2.4.3   Single lens imaging

Konda [44] has developed an FP framework utilizing the Fresnel diffraction formulation to model imaging with a single thin lens. See Figure 2.4 for an illustration of the planes of interest. Let U_o be the exit field of the object. Propagating U_o, using Fresnel transform propagation, Equation (2.30) to a lens positioned a distance z_1 from the object produces a field just before the lens, $U_L^-(u, v)$, given by

$$U_L^-(u, v) = \exp\left[i\frac{k}{2z_1}(u^2 + v^2)\right]\mathcal{F}\left\{U_o(\xi, \eta)\exp\left[i\frac{k}{2z_1}(\xi^2 + \eta^2)\right]\right\}, \tag{2.46}$$
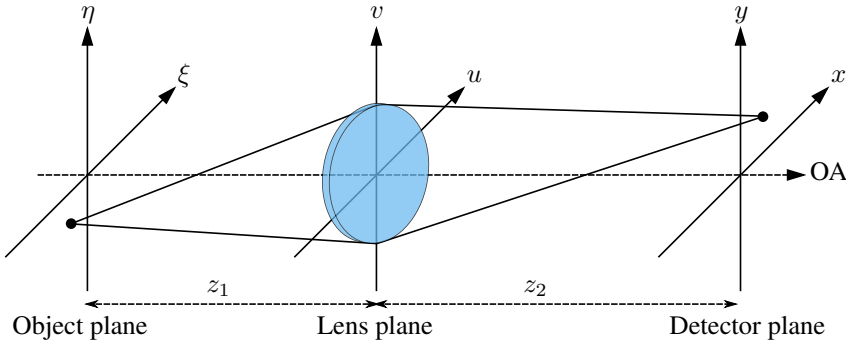
Figure 2.4: The geometry of single lens imaging. OA denotes the optical axis.

where (ξ, η) and (u, v) are the object space and lens space coordinates, respectively, and the Fourier transform is evaluated at $(f_\xi, f_\eta) = (u/\lambda z_1, v/\lambda z_1)$. k denotes the length of the wave vector of the illumination, $k = 2\pi/\lambda$, and λ denotes the wavelength. Throughout the derivation, preceding constants will be dropped for convenience of notation, as they only contribute to a constant scaling factor of the amplitude which is not of interest in this work.

To find the light field just after the lens, U_L^-, must be multiplied with the transfer function of a negative lens [17, 44], given by

$$P(u, v) \exp\left[i\frac{k}{2f}(u^2 + v^2)\right],$$

for a lens with focal length f, where (u, v) is the detector plane coordinates. P is the pupil function of the lens, accounting for the finite aperture of the lens. For an ideal lens, P is 1 when $\sqrt{x^2 + y^2} < w/2$ when w is the diameter of the lens, and 0 otherwise. The resulting complex field, U_L^+ becomes

$$U_\mathrm{L}^+(u, v) = P(u, v) \exp\left[-i\frac{k}{2f}(u^2 + v^2)\right] \exp\left[i\frac{k}{2z_1}(u^2 + v^2)\right] G_\mathrm{o}(u, v), \quad (2.47)$$

where the Fourier transform in Equation (2.46) has been renamed as $G_\mathrm{o}(u, v)$ for convenience of notation.

Reapplying the propagation scheme of Equation (2.30) to find the field at the detector plane, U_D, located z_2 from the lens plane results in

$$U_\mathrm{D}(x, y) = \exp\left[i\frac{k}{2z_2}(x^2 + y^2)\right] \times$$
$$\mathcal{F}\left\{P(u, v) \exp\left[i\frac{k}{2}(u^2 + v^2)\left(\frac{1}{z_1} + \frac{1}{z_2} - \frac{1}{f}\right)\right] G_\mathrm{o}(u, v)\right\}, \quad (2.48)$$

where (x, y) are the coordinates in the detector plane. The quadratic phase factors in the Fourier transform argument will cancel out if the following equation is satisfied

$$\frac{1}{z_1} + \frac{1}{z_2} - \frac{1}{f} = 0, \quad (2.49)$$

which is know as the *lens law* or *Gaussian lens formula* originating from geometrical optics [17, 21]. If the imaging system is in focus, Equation (2.49) must hold [45]. Assuming that there is no defocus, the field at the detector plane becomes

$$U_D(x, y) = \exp\left[i\frac{k}{2z_2}(x^2 + y^2)\right]\mathcal{F}\left\{P(u, v)G_o(u, v)\right\},\tag{2.50}$$

leading to an intensity distribution, $I_D = |U_D|^2$ given by

$$I_D(x, y) = \left|\mathcal{F}\left\{P(u, v)\mathcal{F}\left\{U_o(\xi, \eta)\exp\left[i\frac{k}{2z_1}(\xi^2 + \eta^2)\right]\right\}\right\}\right|^2,\tag{2.51}$$

where $(f_\xi, f_\eta) = (u/\lambda z_1 , v/\lambda z_1)$ and $(f_u, f_v) = (x/\lambda z_2 , y/\lambda z_2)$. It is important to keep in mind that the two Fourier transforms in Equations (2.50) and (2.51) operate on different coordinates. The innermost transform operates on a function of (ξ, η), with resulting frequency coordinates (f_ξ, f_η), while the outermost transform operates on (u, v) and the corresponding output frequencies are (f_u, f_v)

Note that Equation (2.51) will yield an inverted image of the object, due to the negative magnification. The outermost $\mathcal{F}\{\cdot\}$ may be replaced with $\mathcal{F}^{-1}\{\cdot\}$ to re-invert the images to obtain the same orientation as the actual object[3], but the lens will in reality invert the image.

Since the imaging equation derived here is based on Fresnel propagation, it will be termed *Fresnel imaging*.

2.4.4 Imaging as a convolution

In the expression for the field at the detector plane, Equation (2.48), two quadratic phase factors area present; one given in object coordinates and one in detector coordinates. The latter may be ignored when the intensity on the detector plane is the interesting quantity [17], as can be seen from Equation (2.51). The object phase factor, $\exp\left[ik(\xi^2 + \eta^2)/2z_1\right]$, may be ignored if it is close to constant over the integration range[4]. Note that this last step is equivalent to the Fraunhofer approximation presented in subsection 2.2.3, and for a fixed z_1, the Fraunhofer criterion may be fulfilled if the FoV is small. Due to this connection, the resulting imaging formalism will henceforth be termed *Fraunhofer imaging*. The resulting detector field is given by

$$U_D(x, y) = \mathcal{F}\left\{P(u, v)\mathcal{F}\left\{U_o(\xi, \eta)\right\}\right\},\tag{2.52}$$

with the pupil function $P(u, v)$ being 0 for (u, v) outside the pupil and unity inside the pupil. Remembering that the outermost Fourier transform can be replaced with an inverse transform only at the expense of inverting the image about the z axis, Equation (2.52) may be recognized as low-pass filtering the object field. The magnification of the system,

---

[3]If a function, $A(x, y)$, is defined as a Fourier transform of another function, $U(u, v)$, inverting A results in $A(-x, -y) = \mathcal{F}\{U(u, v)\}(-x, -y) = \iint_{-\infty}^{\infty} U(u, v)e^{2\pi i(ux+vy)} \, du \, dv = \mathcal{F}^{-1}\{U(u, v)\}(x, y)$, i.e. replacing the Fourier transform with its inverse.

[4]Or if it is close to constant over the significant region of the point spread function (defined later), and the intensity is the quantity of interest. See ref. [17] for a discussion on this approach.
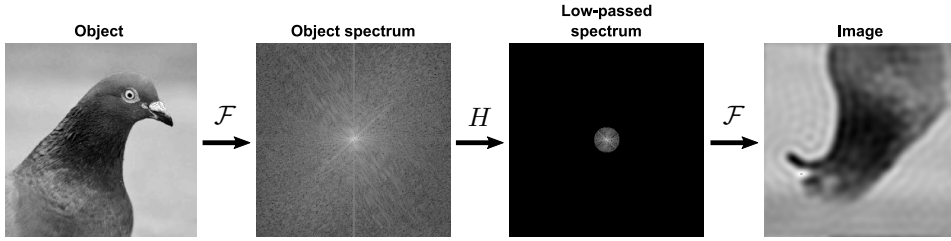
Figure 2.5: Simulated coherent imaging. The imaging process is modeled as low-pass filtering with the transfer function, H. The transfer function effectively silences all frequency information above f_c, and the resulting image has a poorer resolution compared to the actual object. Due to the abrupt coherent cutoff, a ringing effect may be observed around the sharp features in the image.

$M = -z_2/z_1$ is also implicitly included in the equation through the scaling of the frequency coordinates. Using the magnification, one may define the perfect rescaled image predicted by geometrical optics, U_g as

$$U_g(x, y) = U_o\left(\frac{x}{M}, \frac{y}{M}\right), \tag{2.53}$$

which will further simplify the imaging equation to

$$U_D(x, y) = \mathcal{F}^{-1}\left\{H(f_x, f_y)\mathcal{F}\left\{U_g(x, y)\right\}\right\}, \tag{2.54}$$

where H is the coherent transfer function (CTF) of the imaging system, defined as

$$H(f_x, f_y) = P(-\lambda z_2 f_x, -\lambda z_2 f_y) = \begin{cases} 0 & \sqrt{f_x^2 + f_y^2} > w/2\lambda z_2 \\ 1 & \sqrt{f_x^2 + f_y^2} < w/2\lambda z_2 \end{cases}, \tag{2.55}$$

assuming a circular pupil with diameter w. Equation (2.54) may also be recognized as a convolution operation,

$$U_D(x, y) = h(x, y) \circledast U_g(x, y), \tag{2.56}$$

where $h = \mathcal{F}^{-1}\{H\}$ is the point spread function (PSF) of the imaging system, defined as

$$h(x, y) = \iint\limits_{-\infty}^{\infty} P(\lambda z_2 f_x, \lambda z_2 f_y)\exp[-i2\pi(f_x x + f_y y)]\,\mathrm{d}f_x\,\mathrm{d}f_y, \tag{2.57}$$

which is the Fraunhofer diffraction pattern of the pupil function [17].

The CTF imposes a strict cutoff in the frequency domain of the object, as visualized in Figure 2.5. The cutoff frequency, f_c, is given by

$$f_c = \frac{w}{2\lambda z_2}. \tag{2.58}$$

As the resolution of objective lenses normally is specified in terms of NA, defined as the ratio of lens radius to z_1 (assuming the refractive index is 1), it would be convenient to find

an expression for the cutoff frequency in terms of z_1 instead of z_2. This can be achieved by expressing imaging equation, Equation (2.56), as a function of object coordinates (ξ, η), resulting in

$$U_{\mathrm{D}}(M\xi, M\eta) = h(M\xi, M\eta) \circledast U_{\mathrm{o}}(\xi, \eta).$$ (2.59)

From Fourier theory, it is known that $\mathcal{F}\{U(ax, ay)\}(f_x, f_y) = \frac{1}{a^2}\mathcal{F}\{U(x,y)\}\left(\frac{f_x}{a}, \frac{f_y}{a}\right)$ [17], so the object domain cutoff frequency becomes

$$f_{\mathrm{c}} = \frac{w}{2\lambda z_1} = \frac{NA}{\lambda},$$ (2.60)

or equivalently $k_{\mathrm{c}} = k_0 NA$ in wave vector notation.

2.4.5 Aberrations

For real optical systems, a more general formulation of the pupil function is needed, to account for imperfections in the system. Wavefront errors, i.e. phase distortions, are modeled using a *generalized pupil function* [17], $\mathcal{P}$, described by

$$\mathcal{P}(x, y) = P(x, y) \exp[ikW(x, y)],$$ (2.61)

where W is an OPD representing how the wavefront deviates from an ideal spherical wave [17]. The generalized pupil function may replace the ordinary pupil function, P, to account for aberrations in both Fraunhofer and Fresnel imaging models [17, 44].

Zernike polynomials are commonly used to describe aberrations [46]. The Zernike polynomials are a set of orthogonal 2D polynomials defined on a unit circle, and are well suited to describe optical aberrations as the different modes describe known aberration types [46]. To determine the presence of various forms of aberrations, a Zernike decomposition may be performed, representing a known aberration, W, as a polynomial expansion of Zernike modes, as is done in ref. [9].

Onwards in this thesis, the pupil function may be written as a function of frequency coordinates (e.g. (f_x, f_y)) where it is convenient. In such cases, it is simply shorthand notation for $\mathcal{P}(\lambda z_1 f_x, \lambda z_1 f_y)$, or another similar choice of arguments suitable for the case in question.

2.5 Metrics of imaging systems

The quality of an imaging system may be quantified in multiple ways. In this thesis, mainly two quantities will be of interest; the full-pitch resolution and the SBP.

2.5.1 Full-pitch resolution

The full-pitch resolution, which is the recommended resolution measure for coherent microscopy [47], describes the period of the highest spatial frequency the imaging system is capable of collecting [47]. With a cutoff frequency defined by Equation (2.60), the full-pitch resolution, δr, is given by the inverse of the cutoff frequency,

$$\delta r = \frac{\lambda}{NA}.$$ (2.62)

From Equation (2.62) it can be seen the the resolution scales linearly with wavelength, and inversely with numerical aperture.

2.5.2 Space-bandwidth product

The SBP is a measure of the information capacity of an imaging system [48]. There exists multiple definitions of the SBP [48, 49]. The definition that will be used in this thesis is [17, 48]

$$\text{SBP} = L_x L_y B_x B_y = \text{FoV} \times (2f_\text{c})^2,$$
(2.63)

i.e. the product between the collected area in the space and frequency domain, as the name implies. $L_{x,y}$ and $B_{x,y}$ are the lengths and bandwidths in the respective directions, and FoV denotes the field of view of the imaging system. SBP is commonly given in units of megapixels (MPix) [50], as it may be interpreted as the number of pixels required to sufficiently sample the signal transmitted by the optical system [51], when the sampling is done at the Nyquist frequency [17]

$$\Delta x = \frac{1}{B_x} = \frac{1}{2f_\text{c}},$$
(2.64a)

$$\Delta y = \frac{1}{B_y} = \frac{1}{2f_\text{c}},$$
(2.64b)

where Δx and Δy denote the sampling period in the respective directions. The sampling periods specified by Equations (2.64a) and (2.64b) also serve as upper limits for sampling grid periods [37]. Failure to fulfill this requirement leads to *aliasing*, i.e. higher frequencies are wrongly interpreted as lower frequency signals [37].

3

Fourier ptychography algorithms

After the first FP article was published in 2013 [1], a number of algorithms and studies of FP has surfaced. This chapter presents relevant algorithms and related theory, before analyzing the inherent potential resolution gain provided by angularly diverse illumination.

3.1 2D Fourier ptychography

FP is a method of achieving both high resolution and wide FoV at the same time, resulting in a large SBP [1]. The imaging technique relies on collecting multiple low resolution images under different illumination angles, to collect more information about the sample. The different images are then input to an iterative phase retrieval algorithm, to provide a high resolution, wide FoV image with recovered phase.

3.1.1 Angled illumination

Under the assumption that the sample is a 2D thin layer, the interaction between sample and illumination is multiplicative (as discussed in subsection 2.4.1). When the illumination source is sufficiently far away from the object, and a limited field of view is assumed, the illumination may be modeled as plane waves ($\exp(i\mathbf{k} \cdot \mathbf{r})$, with $\mathbf{k}, \mathbf{r}$ as the wave vector and position vector, respectively). Assuming Fraunhofer imaging, described by Equation (2.59) and ignoring the effect of magnification, the image formed under oblique plane wave illumination can be expressed as[50]

$$U_{\mathrm{i}}(x,y) = h(x,y) \circledast \left[t_{\mathrm{o}}(x,y)e^{i(k_{xm}x+k_{ym}y)} \right], \tag{3.1}$$

where t_{o} represents the complex transmittance of the sample, h is the PSF of the imaging system, and k_{jm} is the wave vector component in the $\widehat{j}$-direction of the mth acquired image. Applying a Fourier transform to (3.1), the result is

$$G_{\mathrm{i}}(k_x, k_y) = \mathcal{P}(k_x, k_y)T_{\mathrm{o}}(k_x - k_{xm}, k_y - k_{ym}), \tag{3.2}$$
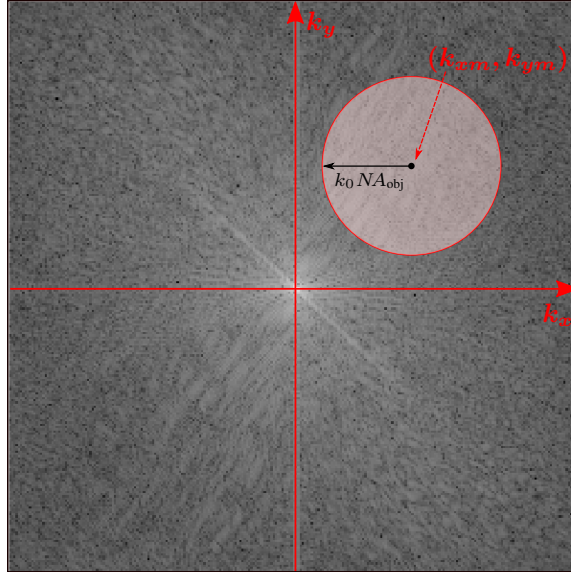
Figure 3.1: 2D transfer function for angled illumination. The incident plane wave shifts the Fourier spectrum of the sample by (k_{xm}, k_{ym}). The transferred frequencies from the sample spectrum are those contained within the red circle centered in (k_{xm}, k_{ym}).

using the frequency shifting theorem. T_o is the Fourier transform of t_o. This shows that a change in the angle of illumination corresponds to a shift in the Fourier domain.

As $\mathcal{P}$ provides an absolute cutoff for frequencies larger than $k_0 NA_\mathrm{obj}$ as per Equation (2.61), each image collected corresponds to a certain area of the objects Fourier domain. More precisely: the area enclosed by a circle with center in (k_{xm}, k_{ym}) and a radius of NAk_0, a result that is illustrated in Figure 3.1. The images acquired under angled illumination, I_m, are related to the Fourier spectrum of the object, T_o by

$$I_m(x,y) = \left| \mathcal{F}^{-1} \left\{ \mathcal{P}(k_x, k_y) T_\mathrm{o}(k_x - k_{xm}, k_y - k_{ym}) \right\} \right|^2. \tag{3.3}$$

The direction of the plane waves is given by the geometry of the experimental setup. For an LED array positioned a distance z_{LED} from the sample and oriented perpendicularly to the optical axis, one may calculate the wave vector components using

$$\begin{bmatrix} k_{xm} \\ k_{ym} \end{bmatrix} = -\frac{k_0}{\sqrt{z_{LED}^2 + x_m^2 + y_m^2}} \begin{bmatrix} x_m \\ y_m \end{bmatrix}, \tag{3.4}$$

where (x_m, y_m) are the transversal coordinates of the mth illumination source in the plane of the LED array. If the center of the reconstructed area is offset from the optical axis by (ξ, η) in the sample plane, Equation (3.4) will have to be modified according to

$$\begin{bmatrix} x_m \\ y_m \end{bmatrix} \leftarrow \begin{bmatrix} x_m - \xi \\ y_m - \eta \end{bmatrix}, \tag{3.5}$$

where $\leftarrow$ denotes a substitution.

3.1.2 FP reconstruction algorithm

The method consists of acquiring M intensity measurements (images) of the sample, with varying illumination angles. Intensity measurements are denoted I_m with $m = 1, 2, ..., M$, and are assumed to be related to the sample spectrum through Equation (3.3). As each unique illumination angle corresponds to a shift in the frequency domain (as shown in Figure 3.1), acquiring multiple images with different illumination angles retrieves information about high-frequent parts of the spectrum, that is normally lost in the imaging process.

The large spatial frequency coverage cannot be straightforwardly combined to one high-resolution representation of the object, as the information is encoded within M intensity images. To cope with this problem, an iterative computational algorithm is applied, based on a computational model of the imaging system, and enforcing the known conditions: the intensity images.

The following algorithm was developed by Zheng et al. [1], and will henceforth be termed the *regular* FP algorithm. See Figure 3.2 for an illustration of the algorithm.

First, initialize a high resolution image, t_o, representing the complex transmittance of the object being imaged. t_o may either be initialized from one of the measurements $\sqrt{I_m}$ using interpolation to increase the pixel number, or just as a flat object (i.e. an array of 1's). The following three steps are performed for all M measurements:

1. Simulate imaging with a plane wave described by (k_{xm}, k_{ym}) to obtain a guess for the field at the image plane, U_m:

$$U_m(x, y) = \mathcal{F}^{-1}\left\{ \mathcal{P}(k_x, k_y) T_o(k_x - k_{xm}, k_y - k_{ym}) \right\}. \tag{3.6}$$

2. Enforce the intensity constraint. The actual measurement is equal to the square of the field amplitude, $I_m = |U_m|^2$, so the known information is imposed on the simulated field as:

$$\widehat{U}_m = \sqrt{I_m}\frac{U_m}{|U_m|}, \tag{3.7}$$

where $\widehat{U}_m$ denotes the updated field.

3. Update the object spectrum, T_o using the intensity constrained field:

$$\widehat{T}_o(k_x, k_y) = T_o(k_x, k_y)[1 - P(k_x + k_{xm}, k_y + k_{ym})] +$$
$$\frac{P(k_x + k_{xm}, k_y + k_{ym}) \mathcal{F}\left\{\widehat{U}_m\right\}(k_x + k_{xm}, k_y + k_{ym})}{\mathcal{P}(k_x + k_{xm}, k_y + k_{ym})}, \tag{3.8}$$

and replace T_o with $\widehat{T}_o$.

Steps 1-3 constitute one iteration of the algorithm. The algorithm may be performed for a predetermined number of iterations, or until convergence is reached.
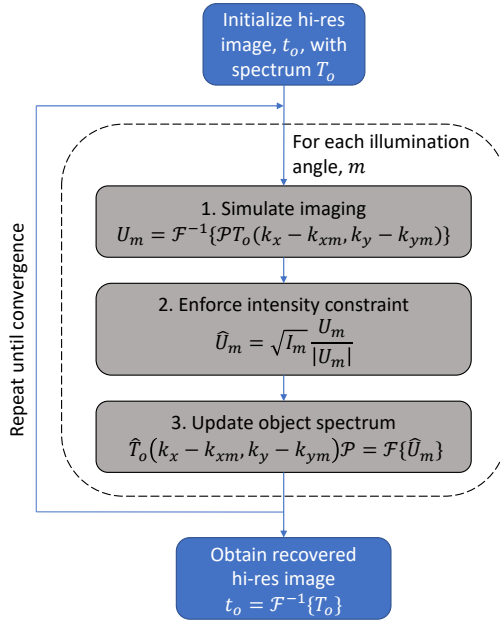
Figure 3.2: Flowchart describing the reconstruction algorithm. $\widehat{T}_{\mathrm{o}}$ denotes an updated variable, and after step 3, T_{o} is set to the updated version, $\widehat{T}_{\mathrm{o}}$, before going on to the $(m+1)$th illumination angle. See Equation (3.8) for an implementation-friendly formulation of the equation in step 3.

3.1.3   EPRY algorithm

The embedded pupil function recovery (EPRY) algorithm is designed to jointly recover the generalized pupil function and the high resolution complex object [9]. Multiple versions of the algorithm exists [7, 9], but in this thesis the attention will be focused on the algorithm developed by Ou et al. [9].

The steps of the algorithm are equivalent to that of the regular FP algorithm, except for step 3, where the object spectrum is updated. Following the same notation as in subsection 3.1.2, step 3 in the EPRY algorithms may be described by three sub-steps [9]:

3a. Update the object spectrum, T_{o} using the new field guess, $\widehat{U}_m$, and the previous guess of the pupil function, $\mathcal{P}$

$$\widehat{T}_{\mathrm{o}}(k_x, k_y) = T_{\mathrm{o}}(k_x, k_y) + \alpha_1 \frac{\mathcal{P}^*(k_x + k_{xm}, k_y + k_{ym})}{|\mathcal{P}|^2_{\max}} \times$$
$$\left[\mathcal{F}\left\{\widehat{U}_m\right\}(k_x + k_{xm}, k_y + k_{ym}) - \mathcal{P}(k_x + k_{xm}, k_y + k_{ym})T_{\mathrm{o}}(k_x, k_y)\right]. \quad (3.9)$$

3b. Use the same updating scheme to arrive at a new guess for the pupil function, $\mathcal{P}$

$$\widehat{\mathcal{P}}(k_x, k_y) = \mathcal{P}(k_x, k_y) + \alpha_2 \frac{T_o^*(k_x - k_{xm}, k_y - k_{ym})}{|T_o|_{\max}^2} \times$$

$$\left[\mathcal{F}\left\{\widehat{U}_m\right\}(k_x, k_y) - \mathcal{P}(k_x, k_y)T_o(k_x - k_{xm}, k_y - k_{ym}) \right]. \quad (3.10)$$

3c. Force the pupil function to be 0 in the region where $H_{\mathrm{coh}} = 0$, as this region corresponds to an aperture stop in the microscope objective. Replace T_o and $\mathcal{P}$ with $\widehat{T}_o$ and $\widehat{\mathcal{P}}$, respectively.

α_1 and α_2 are convergence parameters, both of which are set equal to 1 in this thesis.

The updating steps are similar to those presented in ref. [4] for conventional ptychography. The steps are also closely related to the updating procedure described in subsection 3.2.2 by Equation (3.22), which is investigated in further detail in Appendix B. Note that an alternative strategy for integrated pupil recovery, termed Gauss-Newton FP, uses this approach [7].

3.1.4 Simulated FP imaging

An example of the efficiency of the described algorithm is shown in Figure 3.3. An imaging system with $NA_{\mathrm{obj}} = 0.055$ and sampling pixel size of $1.1\,\mu m$ is simulated by generating low resolution amplitude-only measurements using Equation (3.3) assuming no aberrations and with illumination from a 15×15 LED matrix with a $6\,mm$ gap between LEDs, and a wavelength of $520\,nm$, positioned $12\,cm$ from the sample. The complex object was then reconstructed using 5 iterations of the regular FP algorithm. A complex image of 256×256 pixels was used as input, created using two arbitrary real images, I_a and I_b, combining them into a complex transmittance, $t_{\mathrm{sim.}} = I_a \exp(iI_b)$. The simulated low resolution images were 64×64 pixels. 10 iterations of the regular FP algorithm was performed.

The simulation clearly shows that both amplitude and phase are recovered by the algorithm, albeit with minor deviances. It is also clear that the low resolution images display a distinctively lower image quality. Using this setup, a large section of the original Fourier spectrum is recovered, corresponding well with the observation that the object reconstruction is good.

3.1.5 Quantified resolution enhancement

Applying a 2D FP algorithm, one is able to map out a much larger portion of the sample's Fourier plane than what is possible with conventional imaging using the same microscope setup [50]. This is equivalent to synthetically increasing the NA of the system[1] [52]:

$$NA_{\mathrm{sys}} = NA_{\mathrm{obj}} + NA_{\mathrm{illu}}, \quad (3.11)$$

where NA_{sys}, NA_{obj} and NA_{illu} denote the synthetic, objective and illumination numerical aperture, respectively. The latter is defined as

$$NA_{\mathrm{illu}} = \sin\left(\max_m \theta_m\right), \quad (3.12)$$

---

[1]This will be shown rigorously in section 3.3.
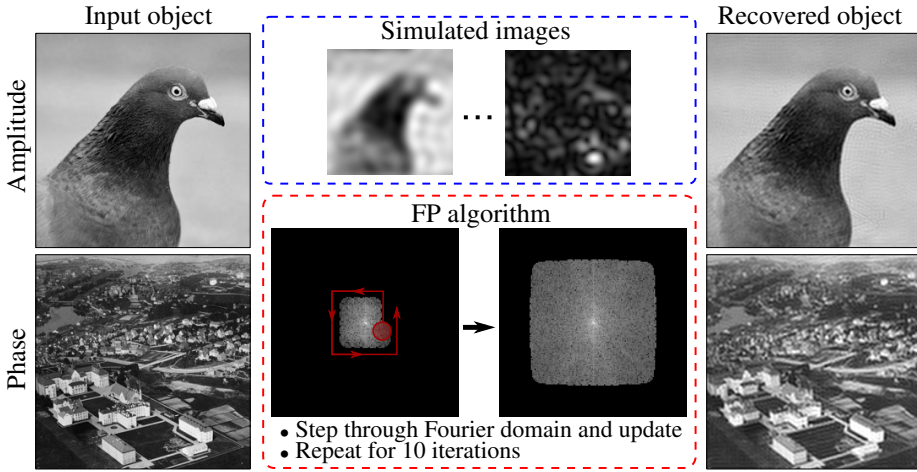
Figure 3.3: Simulated Fourier ptychography imaging. The left column shows the complex input image, with the phase and amplitude separately displayed. In the dashed blue rectangle, two simulated low resolution images are shown, corresponding to different angles of illumination. Within the dashed red rectangle, the reconstruction order is illustrated, as well as the final recovered Fourier power spectrum. The right column displays the reconstructed result using the regular FP algorithm. *Aerial photo over Gløshaugen* is owned by Municipal Archives of Trondheim, licensed under CC BY 2.0.

where θ_m is the angle of illumination relative to the optical axis for the mth image, and the refractive index of the surrounding media is assumed to be 1. Following Equation (2.62), the full-pitch resolution of the reconstruction becomes

$$\delta r = \frac{\lambda}{NA_{\mathrm{obj}} + NA_{\mathrm{illu}}}. \tag{3.13}$$

The theoretical enhancement factor of the SBP can be calculated from NA_{sys} [53], as the numerical aperture of the system is proportional to the cutoff frequency, per Equation (2.60). Since the cutoff frequency is increased in both x and y directions, the theoretical SBP enhancement factor becomes [53]

$$\frac{\mathrm{SBP_{FP}}}{\mathrm{SBP}} = \left(\frac{NA_{\mathrm{sys}}}{NA_{\mathrm{obj}}} \right)^2 = \left(1 + \frac{NA_{\mathrm{illu}}}{NA_{\mathrm{obj}}} \right)^2. \tag{3.14}$$

Considering a system with $NA_{\mathrm{obj}} = 0.055$ and $NA_{\mathrm{illu}} = 0.30$, corresponding to a $17.5°$ maximum illumination angle, the SBP enhancement factor would be 42. However, this enhancement factor is compared to coherent imaging. The incoherent transfer function, or the optical transfer function (OTF), would have a cutoff frequency of $2f_c$, and thus twice the bandwidth in both x- and y-directions [17]. Comparing the SBP gain of FP with incoherent imaging thus provides a more realistic measure of the increase in performance. The SBP gain compared with incoherent microscopy can be found by

$$\frac{\mathrm{SBP_{FP}}}{\mathrm{SBP_{incoh.}}} = \left(\frac{1}{2} + \frac{NA_{\mathrm{illu}}}{2NA_{\mathrm{obj}}} \right)^2, \tag{3.15}$$
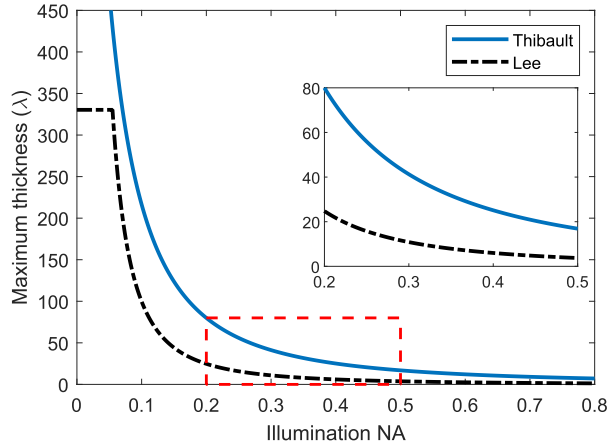
Figure 3.4: Comparison of two different thickness criteria, using $NA_{obj} = 0.055$. The inset displays a zoomed version of the part enclosed by the dashed rectangle.

and for the described experiment, Equation (3.15) yields a factor of 10.

3.1.6 Validity of 2D approximation

However, for larger samples it becomes necessary to account for the finite thickness of the sample [25]. Here, two different criteria for the validity of the multiplicative approximation will be presented.

The first criterion, found by Thibault et al. based on analysis of the Helmholtz equation [25], later refined by numerical simulations [54] is stated as

$$T \leq \frac{5.2\delta r^2}{\lambda},\tag{3.16}$$

where T is the thickness of the sample and δr is the resolution. It is worth noticing that this relation is derived based on an assumption that the input field is a plane wave in the z-direction [25], which is not the case for FP. The effect of angularly diverse illumination may be introduced by using the theoretically predicted full-pitch resolution of the reconstructed object, given by Equation (3.13).

The second criterion, developed by Lee et al. [26], is treated in the FP framework by Ou et al. [55], arriving at

$$T \leq \frac{\lambda}{2}\left(1 - \sqrt{1 - NA_{max}^2}\right)^{-1},\tag{3.17}$$

where NA_{max} is the largest of NA_{obj} and NA_{illu}. In most cases, $NA_{illu} > NA_{obj}$. The criterion stated by Equation (3.17) is derived assuming Fraunhofer propagation [26].

The thickness criteria are compared in Figure 3.4. It can be seen that the criterion proposed by Lee et al., based on Fraunhofer propagation, is much stricter than the maximum

thickness proposed by Thibault et al. In ref. [55], it is argued that the criterion given by Equation (3.17) is valid for samples with large structural variations in the z-direction, while samples with a more uniform distribution along z can be modeled as 2D samples even if the criterion is violated.

3.2 3D Fourier ptychography

The reconstruction scheme for 3D samples presented in this section is developed by Tian and Waller [6], based on the ptychographic 3D procedure in ref. [5], using a multislice model of the sample to (see subsection 2.4.2). The aim of the method is to arrive at a set of object slices $\{q_n\}$ that minimizes the error, E, described by [6]

$$E\left(\{q_n\}\right) = \sum_m \sum_{x,y} \left|I_m(x,y) - I_m^{\text{sim.}}(x,y)\right|^2,\tag{3.18}$$

where I_m denotes the measurement acquired with the mth LED, and $I_m^{\text{sim.}}$ is the image simulated using a multislice model and an input illumination corresponding to a plane wave originating from the mth LED.

The recombination is based on an iterative gradient descent procedure [6], and in order to reduce the risk of the algorithm being stuck in local minima, a good initial object guess is provided by performing a light field refocusing [2] step for each of the layers of the sample [6].

3.2.1 Light field refocusing

Light field refocusing is a geometrical refocusing algorithm that, like Fourier ptychography, relies on angularly diverse illumination [2]. When the sample is displaced by a distance δz from the focus plane, and the illumination has a nonzero angle with respect to the optical axis, the field at the focus plane will be shifted [2]. Light field refocusing back-shifts each image by the correct amount, and superimposes all the collected images [6]:

$$I_{\delta z}(x,y) = \sum_n I_m\left(x - x_m \frac{\delta z}{z_{\text{LED}}}, y - y_m \frac{\delta z}{z_{\text{LED}}}\right),\tag{3.19}$$

where $I_{\delta z}$ is the light field refocused image, and (x_m, y_m) are the coordinates of the nth LED respective to the optical axis.

The geometrical reasoning for the shifts of $x_m \delta z / z_{\text{LED}}$ is illustrated in Figure 3.5. The observed x-position in the focus plane deviates from the actual position by δx_m. By similarity of the two triangles in the figure, the shift can be expressed

$$\delta x_m = x_m \frac{\delta z}{z_{\text{LED}}},\tag{3.20}$$

and similarly for the y-coordinates.

The initial 3D object guess is then found by computing the light field refocusing result for each of the slices [6],

$$q_n(x,y) = \sqrt{I_{\delta z_n}(x,y)},\tag{3.21}$$
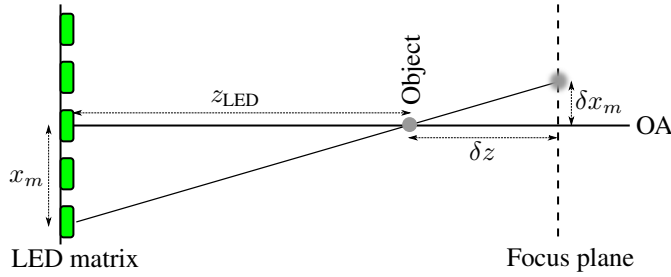
Figure 3.5: Image shift from off-axis LEDs when the object is placed a distance δz away from the focus plane. OA is short for optical axis.

where q_n is the slice guess and δz_n is the distance from the focus plane to the nth slice. Note that the light field refocusing method produces a pure amplitude guess, i.e. the phase is assumed to be zero for all (x, y) in all N slices in the initial guess.

3.2.2 Updating step

In the reconstruction algorithm, the slices of the object, as well as the pupil function and output spectrum are updated repeatedly to reach convergence [6]. The updating function, $\mathcal{U}$, is a gradient descent procedure described by [6] to estimate the value of a function ψ, given an update in the product of ψ with another function ϕ. If $\gamma = \psi\phi$ then [6]:

$$\widehat{\psi} = \mathcal{U}\left(\psi, \phi, \gamma, \widehat{\gamma}\right) = \psi + \frac{|\phi|\phi^*(\widehat{\gamma} - \gamma)}{|\phi|_{\max}(|\phi|^2 + \delta)}, \tag{3.22}$$

where $\widehat{\gamma}$ denotes the updated product value, * denotes the complex conjugate, and δ is a regularization constant to avoid division by zero.

For further discussion and analysis of the gradient descent step described by Equation (3.22), the reader is referred to Appendix B.

3.2.3 Reconstruction algorithm

When describing the reconstruction algorithm, the notation used in subsection 2.4.2 will be used to describe the field at different positions. Hat notation, $\widehat{\cdot}$, denotes an updated version of the variable.

In the description of the algorithm, G will denote the Fourier spectrum of the exit field of the multislice model, H is a defocus term in Fourier space, as given by the angular spectrum method (Equation (2.20)), and C denotes the complex field after the lens, i.e. the frequency spectrum of the field reaching the detector:

$$C = G H \, \mathcal{P} \, . \tag{3.23}$$

The same variable names that were used in subsection 2.4.2 will be used to describe the quantities in the multislice model: q_n, f_n and g_n denote respectively the transmittance of

the nth slice, the field just before the slice and the field just after the slice. The slices are separated by a distance Δz.

For all the m different images in the dataset, corresponding to m unique illumination angles, the following steps are performed to update the current guess of the object slices, $\{q_n\}$ [6]:

1. Simulate transmission through a multislice model, Equations (2.42)–(2.43), with an input field described by a plane wave,

$$f_1(x, y) = \exp[i(k_{xm}x + k_{ym}y)], \tag{3.24}$$

   where the k-vector components are given by the position of the mth LED, per Equation (3.4), arriving at an exit field, g_N, and the corresponding Fourier spectrum, $G = \mathcal{F}\{g_N\}$. Using Fraunhofer imaging, Equation (2.54), the field at the detector plane, $U^{(m)}$ is found through

$$U^{(m)} = \mathcal{F}^{-1}\{C\} = \mathcal{F}^{-1}\{GH\,\mathcal{P}\}. \tag{3.25}$$

   This step yields a simulated image of the current object guess, $I_m^{\text{sim.}} = |U^{(m)}|^2$.

2. Replace the amplitude of the simulated field with the measured amplitude.

$$\widehat{U}^{(m)} = \sqrt{I_m}\,\frac{U^{(m)}}{|U^{(m)}|} \tag{3.26}$$

3. Perform a Fourier transform to obtain a new estimate for the Fourier spectrum at the lens plane,

$$\widehat{C}^{(m)} = \mathcal{F}\left\{\widehat{U}^{(m)}\right\}. \tag{3.27}$$

4. Update G and $\mathcal{P}$ based on the new estimate for C

$$\widehat{G}^{(m)} = \mathcal{U}\left(G^{(m)}, \mathcal{P}, C^{(m)}/H, \widehat{C}^{(m)}/H\right), \tag{3.28}$$

$$\widehat{\mathcal{P}} = \mathcal{U}\left(\mathcal{P}, G^{(m)}, C^{(m)}/H, \widehat{C}^{(m)}/H\right). \tag{3.29}$$

5. Perform an inverse Fourier transform to find the exit field of the multislice sample:

$$\widehat{g}_N^{(m)} = \mathcal{F}^{-1}\left\{\widehat{G}^{(m)}\right\}. \tag{3.30}$$

6. Update the slices of the object, as well as the fields before each slice,

$$\widehat{q}_n^{(m)} = \mathcal{U}\left(q_n^{(m)}, f_n^{(m)}, g_n^{(m)}, \widehat{g}_n^{(m)}\right), \tag{3.31}$$

$$\widehat{f}_n^{(m)} = \mathcal{U}\left(f_n^{(m)}, q_n^{(m)}, g_n^{(m)}, \widehat{g}_n^{(m)}\right), \tag{3.32}$$

   And back-propagate the field just before each slice with a distance Δz to get the field just after the last slice,

$$\widehat{g}_n^{(m)} = \mathcal{P}_{-\Delta z}\{f_n^{(m)}\}. \tag{3.33}$$

7. For the first slice, keep the input illumination constant,

$$\widehat{f}_1^{(m)} = f_1^{(m)}. \tag{3.34}$$

8. Let all the updated variables replace the current version of the variables,

$$p \leftarrow \widehat{p}, \tag{3.35}$$

for a general variable p.

Performing these steps for all m images completes one iteration of the algorithm. After each iteration the convergence can be quantified using Equation (3.18), and multiple iterations can be performed to reach acceptable convergence.

This algorithm will be termed *TW-3D*, named after the initials of the authors.

Note a minor deviation from the algorithm presented in ref. [6]: Propagation from the lens plane to the detector plane is modeled as inverse Fourier transform instead of a Fourier transform, to incorporate the fact that the camera software often automatically performs an inversion operation when transferring the image to the computer.

3.2.4 Proposed modification to the algorithm

The TW-3D algorithm relies on Fraunhofer imaging theory (see subsection 2.4.4) to model the imaging process, i.e. the lens pupil provides a discrete cutoff in the Fourier spectrum of the sample. As previously discussed, the Fraunhofer approximation is only valid for large propagation distances, and/or small FoV. The new proposed algorithm uses Fresnel imaging theory to model the imaging, e.g. Equation (2.50), and is thus subject to fewer assumptions than the algorithm described by Tian and Waller [6].

The following changes to the algorithm are proposed:

1. Modify the imaging simulation to use the Fresnel imaging model. In practice, this means multiplying the exit field with an object space quadratic phase factor,

$$\exp\left[i\frac{k}{2z_1}(x^2 + y^2)\right], \tag{3.36}$$

resulting in the exit field field "Fresnel spectrum" being found as

$$G^{(m)} = \mathcal{F}\left\{g_N^{(m)} \exp\left[i\frac{k}{2z_1}(x^2 + y^2)\right]\right\}, \tag{3.37}$$

as given by Equation (2.46).

5. To find the updated exit field, $\widehat{g}_N^{(m)}$, back-propagate the lens field using Fresnel propagation, i.e. introduce an additional multiplication with the conjugate phase factor.

$$\widehat{g}_N^{(m)} = \mathcal{F}^{-1}\left\{\widehat{G}^{(m)}\right\} \times \exp\left[-i\frac{k}{2z_1}(x^2 + y^2)\right] \tag{3.38}$$
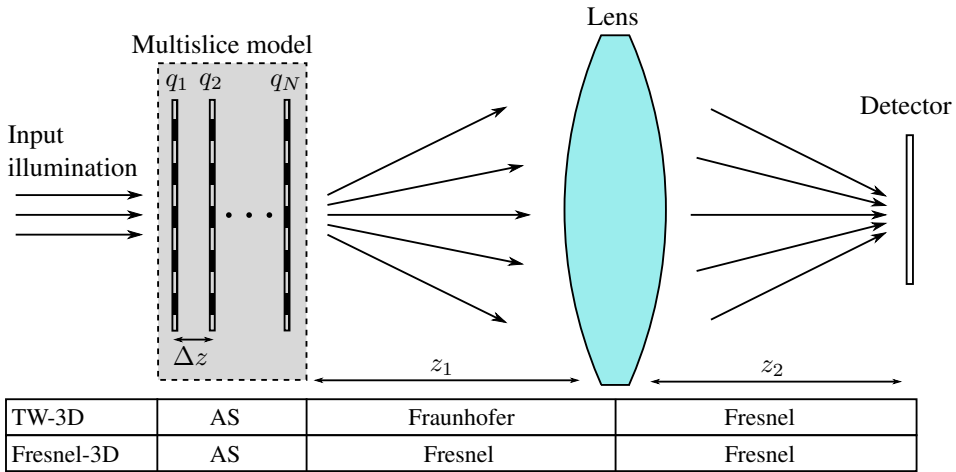
Figure 3.6: 3D imaging models used in the TW-3D and Fresnel-3D algorithms. The table describes the propagation methods used in the different parts of the model. AS is short for angular spectrum. The sketch is not to scale.

Note that preceding multiplicative factors have been dropped. The detector plane phase factor is also ignored, as it will cancel out when back-propagating the detector field to the object plane. The modification is inspired by a similar modification by Konda [44] for 2D FP.

The modified version of the algorithm will be named *Fresnel-3D*, to emphasize that Fresnel imaging theory is used. An illustration of the imaging model for 3D imaging is shown in Figure 3.6, where the similarities and differences between the Fresnel and Fraunhofer imaging models are highlighted.

As the Fresnel-3D algorithm is based on the TW-3D algorithm, with less approximations, it is expected to produce results that are equal or better than what is obtained with TW-3D. The quadratic phase factor, (3.36), will be approximately constant over a small region close to the optical axis, where

$$(x^2 + y^2) \ll \frac{\lambda z_1}{\pi}, \tag{3.39}$$

and thus the Fresnel-3D and TW-3D algorithms will be practically equivalent for this region. Considering larger areas, or small areas positioned further away from the optical axis, the impact of the Fresnel phase factor will be much larger as the phase of (3.36) is proportional to the square of the distance to the optical axis. For such regions, the results are expected to differ between the two algorithms. Note that for imaging systems without significant aberrations, the Fraunhofer approximation will be valid for larger regions, due to the small significant region of the PSF (as discussed in ref. [17]).
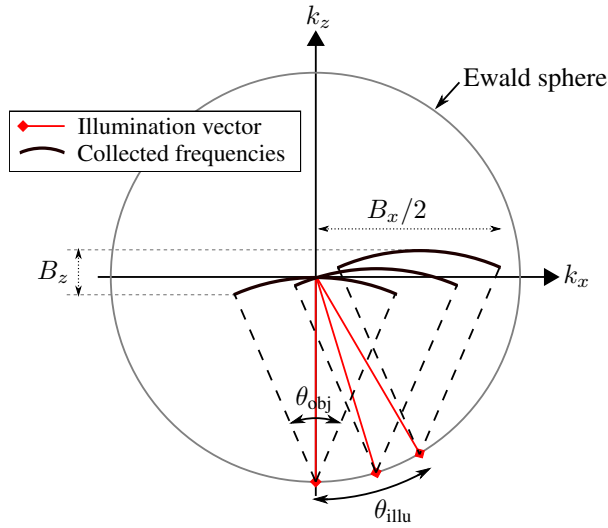
Figure 3.7: 3D resolution analysis based on a single scattering approximation and three illumination angles. The angles are related to the respective NAs through $NA_{\mathrm{obj}} = \sin\theta_{\mathrm{obj}}$ and $NA_{\mathrm{illu}} = \sin\theta_{\mathrm{illu}}$, assuming the refractive index of the media is 1. The radius of the Ewald sphere is k_0, and B_x and B_z represent the collected bandwidths in the respective directions. The multi-image analysis is inspired by those in refs. [6, 15].

3.3 Resolution analysis

To analyze the resolution for both 2D and 3D FP, a model based on single scattering and Fraunhofer imaging will be used, as is done in refs. [6, 15].

A useful construct for analyzing 3D scattering is the *Ewald sphere* [56]. A graphical resolution analysis for multislice FP based on the Ewald sphere and the 3D CTF [57] is shown in Figure 3.7, assuming a small illumination source area, A_s. The illustration shows the captured frequency information in the (k_x, k_z) plane. Each circle arc represents the part of the 3D Fourier transform of the sample that contributes to the intensity image for the given illumination angle. The same solid angle of frequencies are always collected by the pupil, leading to different parts of the spectrum being collected for different illumination angles [15]. When multiple illumination angles are used, a larger portion of the object frequency domain is collected, contributing to an extended bandwidth compared to what is obtained with a single image.

For a pupil with rotational symmetry about the z axis, the circle arcs represent spherical caps in (k_x, k_y, k_z) space [57]. This means that the overlap of collected frequencies between different illumination angles are larger than what is seen in Figure 3.7.

Based on the analysis in Figure 3.7, the collected frequency bandwidths can be expressed as

$$B_x = B_y = 2k_0(NA_{\mathrm{illu}} + NA_{\mathrm{obj}}), \tag{3.40}$$

$$B_z = k_0\left(2 - \sqrt{1 - NA_{\mathrm{obj}}^2} - \sqrt{1 - NA_{\mathrm{illu}}^2}\right), \tag{3.41}$$
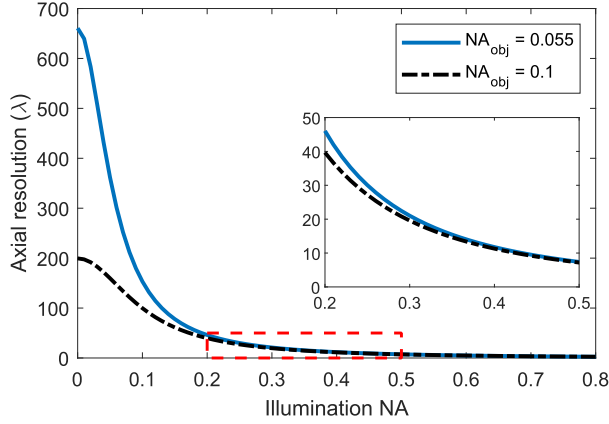
Figure 3.8: Obtainable axial resolution using 3D FP, evaluated in terms of wavelength (λ), plotted against illumination NA. The inset displays a zoom-in of the section enclosed by the dotted rectangle.

where B_j represents the angular bandwidth in the j-direction, and a circularly symmetrical pupil is assumed. Equation (3.40) may be recognized as equivalent to Equation (3.11), when noticing that the synthetic numerical aperture of the system, NA_{sys}, is half the bandwidth in the transversal directions. Thus the expected resolution gain of 2D FP has been proved, and it can be seen from Equation (3.40) that the obtained resolution with FP is equivalent to the resolution that would be obtained using an objective with a larger NA of $NA_{sys} = NA_{obj} + NA_{illu}$.

The same lateral bandwidth is expected for 3D FP. However, the axial resolution behaves quite differently from the transversal directions. In the axial direction, the resolution gain is lower than what is obtained by extending the NA of the system, as an objective with a numerical aperture of $NA_{obj}+NA_{illu}$ would yield a bandwidth of $k_0(1-\sqrt{1 - (NA_{obj} + NA_{illu})^2})$ [6]. This difference can be attributed to the different nature of the transversal and axial directions in the imaging setup; the pupil function imposes a finite limit in a transversal plane, and the image acquisition is also done in a transversal plane.

The half-pitch resolution in the axial direction, can be found by dividing 2π with the bandwidth[2]:

$$\delta z = \frac{\lambda}{2 - \sqrt{1 - NA_{obj}^2} - \sqrt{1 - NA_{illu}^2}}. \tag{3.42}$$

To illustrate the obtainable resolution in the z direction, Equation (3.42) is plotted versus NA_{illu} for two different objective lenses in Figure 3.8. It is evident from the plot that for small NA_{illu}, the different objectives yield vastly different axial resolutions, but this difference quickly diminishes for larger NA_{illu}.

Note that the resolution analysis presented in this subsection assumes that the collected frequency information is combined perfectly in the reconstruction process. For this to be the case, sufficient overlap between neighboring illumination angles is required. For 2D FP,

---

[2]The factor 2π arises because the bandwidths are given in angular frequency.

the overlap requirement has been studied through simulations, revealing that the overlap between neighboring circles in the Fourier domain should be at lest 35% in the lateral plane [58]. The FP setup may be modified by adjusting z_{LED} to fulfill this criterion. No similar criterion has been found for multislice FP. However, it is reasonable to assume that at least the same transversal overlap should be required.

The Fresnel-3D algorithm does not make the assumption of Fraunhofer imaging, nor does it assume single scattering. Thus, the resolution analysis is not directly applicable to the Fresnel-3D reconstruction model. The analysis does, however, provide an indication to what could be expected in terms of lateral and axial resolution.

Chapter 4

Experimental

The experimental setup employed in this project is based on a setup designed by Kringeland during his master studies [59].

This chapter proceeds to present the experimental setup, along with numerical aspects of FP, and implementation details.

4.1 Microscope Components

The microscope setup is shown in figure 4.1. The setup is horizontal; which is in contrast to normal vertically aligned microscopes, but more in line with most X-ray imaging setups. Building the microscope on an optical table makes it easy to vary the sample-to-LED distance, z_{LED}, and the focus may be adjusted using a stepper motor to move the microscope in the axial direction.
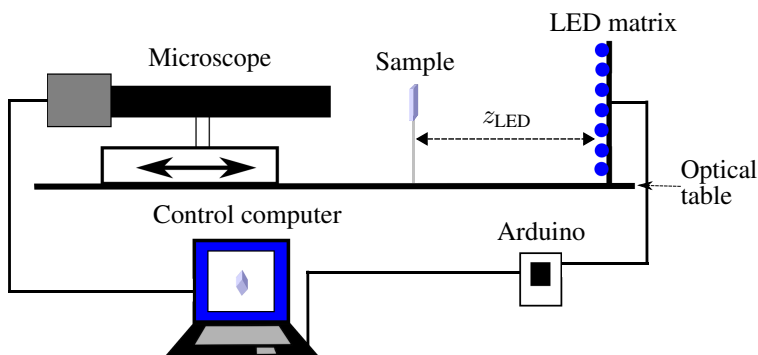
Figure 4.1: Sketch of the experimental setup. Figure adapted from [59] with permission.
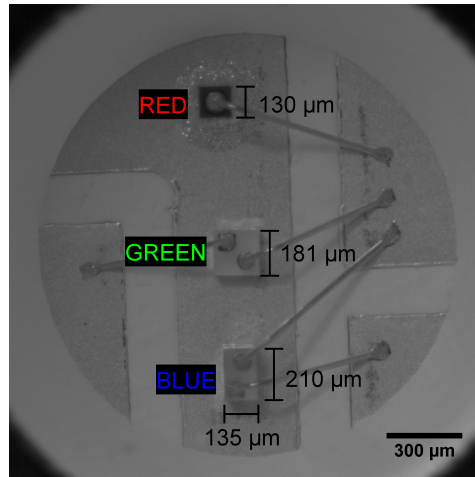
Figure 4.2: Close-up image of one of the RGB LEDs on the LED matrix, located on the 17th column and the 13th row, counting from the upper left corner. The red, green and blue LEDs are indicated, and relevant dimensions are shown. For the red and green regions, only one dimension is shown, since the emitting areas are square.

4.1.1 LED Illumination

The varied illumination angles are implemented using an LED matrix, which is a common method to control illumination angles for FP [1, 6, 50]. The matrix contains 32×32 RGB LED elements, meaning that each of the 1024 elements contain both red, green and blue LEDs. To control the LEDs, 12 FD9802 LED drivers are used. To power the LED board, a $5\,\mathrm{V}\ 1\,\mathrm{A}$ power supply is used.

The distances between each RGB LED element is $6.0\,\mathrm{mm}$, center-to-center. One of the RGB LEDs is shown in figure 4.2, also showing the dimensions of the emitting regions. The characteristics of the LED elements are shown in Table 4.1. As the supplier of the LED matrix does not provide any specifications of the individual RGB LED elements, the $\bar{\lambda}$ values listed in the table are based on regular values for similar RGB LEDs. The wavelength spread, $\Delta\lambda$, was measured in an earlier project, using a Michelson interferometer and Equation (2.38). The results indicate that for all three different LEDs, $\Delta\lambda \ll \bar{\lambda}$, and the illumination may be modeled as quasimonochromatic, with $\lambda = \bar{\lambda}$.

Table 4.1: Characteristics of the LEDs. The coherence areas in the sample plane have been calculated with Equation (2.39) assuming a source distance of $140\,\mathrm{mm}$.

Color	Nominal $\bar{\lambda}$ (nm)	A_{s} (µm × µm)	A_{c} (µm × µm)
Red	625	130×130	670×670
Green	520	181×181	402×402
Blue	470	135×210	487×313

The LED matrix is controlled using an Arduino Due, with a corresponding shield: a
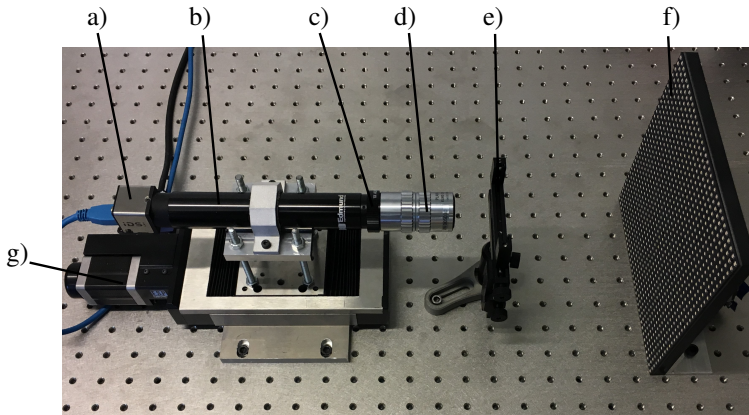
Figure 4.3: The imaging system. a) detector, b) optical extension tube, c) tube lens, d) objective, e) sample holder, f) LED matrix, and g) stepper motor.

plug-in board simplifying the connections to the LED matrix. The Arduino Due is based on a AT91SAM3X8E microcontroller, incorporating an ARM Cortex-M3 CPU, with a clock speed of $84\,\mathrm{MHz}$ [60]. The high clock speed is important to allow high imaging speed. The microcontroller has $512\,\mathrm{kB}$ of flash memory and $96\,\mathrm{kB}$ of SRAM [60]. The software running on the Arduino is written so that each RGB LED can display 3-bit colors, meaning that each of the colored LEDs can either be *on* or *off*.

The LED board is not able to light up all the 1024 RGB LEDs at full power at the same time, due to the intense current requirement. Therefore, the default operation of the LED matrix lights up the LEDs in a sequential manner, only powering 2 of the 32 rows at a time. With fast cycling through the rows, this results in the appearance of lighting up the entire board. Thus, in the standard operation mode, the LEDs are only lit $1/16$ of the time, vastly reducing the intensity of the illumination. A high-intensity mode was implemented in the Arduino code, that circumvents the intensity limitation of the scanning operation, at the cost of only being able to light up a single RGB LED at a time. Using this mode, the required exposure time of the camera was vastly reduced, speeding up the imaging process by a factor ≥ 10.

4.1.2 Optical Components

The imaging system is built of four principal components: an objective lens, a tube lens, an optical extension tube and a detector (camera). The system and the components are shown in Figure 4.3.

The objective lens is infinity corrected with long working distances and plan apochromatic aberration correction [61], and is delivered by Edmund Optics. The specifications of the lens are given in Table 4.2.

The objective lens is connected to a 1X tube lens, serving as a connection to the optical extension tube and focusing the light onto the image plane. The tube reduces noise in the system while fixing the distance between the tube lens and the camera, to ensure correct

Table 4.2: Properties of the employed objective lens. The information is gathered from [61] and [62]. Explanation of abbreviations: M = magnification, FoV = Field of View with image sensor, DoF = depth of field, WD = working distance, RP = resolving power and FL = focal length.

M	NA	FoV (μm^2)	WD (mm)	DoF (μm)	RP (μm)	FL (μm)
2X	0.055	2.8×2.1	34	91.0	5.0	100.0

magnification.

The camera employed is IDS UI-3480CP Rev. 2 [62], a monochrome camera based on an MT9P031STM CMOS sensor manufactured by ON Semiconductor, delivering a resolution of $2560 \, \text{pixels} \times 1920 \, \text{pixels}$. The optical class of the sensor is $1/2''$, meaning that the sensor width is $6.40 \, \text{mm}$ an the height is $4.80 \, \text{mm}$. The pixel size is $2.20 \, \mu\text{m}$. The sensor has 12-bit color depth, but 8-bit values are used in this project. The camera is connected to the computer using an USB cable.

To shield the imaging system from ambient light, a cardboard box is put on top of the setup. This measure is important for noise reduction in the dark field (DF) images, since the intensity is much lower for these angles. A rectangular aperture is placed between the sample and the objective, preventing noise from stray light.

4.1.3 Mechanical Control

To be able to adjust the z-position of the plane of focus, the imaging system is mounted on top of a movable stage, as seen in Figure 4.3. The stage is a Newport UTS50PP stepper motor, controlled using a Newport SMC-100PP stepper motor driver, connected to the computer using an RS-232 (serial) cable. The stepper motor has $\pm 2.5 \, \mu\text{m}$ guaranteed accuracy, and a $\pm 1.2 \, \mu\text{m}$ typical accuracy, with a minimum step size of $0.30 \, \mu\text{m}$ [63].

The height of the microscope may be adjusted using four screws, seen in Figure 4.3. In addition, the screw holes used to fasten the microscope to the optical table have been widened, providing possibility for motion in the horizontal direction perpendicular to the optical axis. These two measures provide the possibility of moving the imaging system around in the plane perpendicular to the optical axis.

4.1.4 Camera Control

As seen from Figure 4.1, a central computer controls and coordinates the different components. As with the physical setup, the software is based upon the work of Kringeland in ref. [59], and adapted to fit the requirements of this project. Important new features implemented as a part of this thesis are:

- Varied exposure time for the camera. The software can use a different exposure time for high-angle LEDs than for low-angle LEDs, in the same acquisition round.

- An option of using the high-intensity mode of the LED board.

- Compression of images. Images may be saved in a lossless compressed format, drastically reducing the required data storage space.

- Parallelization of the software. Image acquisition and compression/saving is handled in parallel, speeding up the acquisition process.

- Automatic generation of setup file containing all relevant parameters for the acquisition.

in addition to multiple less important feature upgrades.

The software is developed in LabVIEW, using instrument drivers provided by Newport and IDS for their equipment.

4.2 Noise reduction

Various sources of noise exist in the collected datasets, and multiple measures were taken in order to circumvent the limitations caused by the noise.

4.2.1 Ignoring BF edge images

The regions of the images close to the edge between bright field (BF) and DF regions were ignored in the reconstructions, as they tended to introduce substantial low-frequent noise to the reconstructed field. An image appears as a BF image if the zero-frequency of the Fourier spectrum is collected by the imaging system [11], i.e. when

$$NA_m^{\text{LED}} = \frac{\sqrt{k_{xm}^2 + k_{ym}^2}}{k_0} < NA_{\text{obj}}, \tag{4.1}$$

where $NA_m^{\text{LED}} = \sin \theta_m$, and θ_m is the angle of illumination from the mth LED with respect to the optical axis. It was found that ignoring the sections where

$$S_m = \frac{NA_m^{\text{LED}}}{NA_{\text{obj}}} \in (0.94, 1.15) \tag{4.2}$$

removed the low-frequent noise. The interval in (4.2) was determined by systematically varying the upper and lower limits of the interval and observing the quality of the reconstruction. All image sections falling into this region were left out of the reconstructions. S_m is a dimensionless number, being < 1 for BF images and > 1 for DF images.

4.2.2 Processing of DF images

DF images often exhibit poor contrast due to the low intensity of high-angle scattering. To cope with this, multiple steps are taken. The contrast is vastly increased by shielding the microscope and inserting an aperture between sample and objective, but further measures are still needed.

One solution is increasing the acquisition time for the higher illumination angles to acquire necessary information, as was done by for example Tian and Waller [6].

Another step to provide a higher contrast in the DF images is by introducing a noise reduction step before performing the reconstruction. In this project, two noise reduction

steps are applied. The first step is based on subtracting a dark image, I_D [64], i.e. an image acquired with no illumination. This step is meant to remove the influence of the dark current in the detector [64]. Each intensity measurement, I_m is modified according to [64]

$$I'_m(x, y) = I_m(x, y) - \alpha_m I_D(x, y),$$ (4.3)

where α_m is given by [64]

$$\alpha_m = \frac{\left\langle \sum_{x,y} I_m(x, y) I_D(x, y) \right\rangle_R}{\left\langle \sum_{x,y} I_D(x, y)^2 \right\rangle_R},$$ (4.4)

with the sum over x, y indicating a sum over all pixels in a subregion, and $\langle \cdot \rangle_R$ meaning the average over multiple subregions, with two regions normally being sufficient [64].

This second step is only performed when the dataset is particularly noisy. It is based on a thresholding method, to remove residual noise after the first step [64], as random noise arising from the stochastic process of photon counting[1] [45]. The method used, is based on the *conventional method* presented in ref. [65]. First, the average intensity value over multiple subregions, ϵ_n is calculated:

$$\epsilon_n = \left\langle \langle I'_m(x, y) \rangle_{x,y} \right\rangle_R,$$ (4.5)

where $\langle \cdot \rangle_{x,y}$ indicate the average over all pixels in one region. Thereafter, the average is subtracted from each intensity measurement [65]:

$$I''_m(x, y) = I'_m(x, y) - \epsilon_n,$$ (4.6)

where I''_m denotes the intensity measurement that is used for recombination. Any negative values are set to 0 [65].

4.3 Alignment

Correct alignment is vital for the FP procedures to produce good results, as the position of the LEDs with respect to the optical axis are used to find the shift in the frequency domain (through Equation (3.4)). Incorrect alignment produces incorrect k-vectors, and the foundation for the FP algorithms break down. Note that the important quantity is the positions of the LEDs — the LED matrix does not have to be centered on the optical axis.

An alignment method was developed, relying on the bright field criterion given by Equation (4.1). As the angle of illumination will vary with the position in the object plane, the substitution given in Equation (3.5) was performed before calculating the expected k-vector using (3.4), for each point in the FoV. The BF criterion was validated for each point, and the value was set to 1 if the condition was fulfilled, and 0 otherwise. This

---

[1]Photon detectors measure the light intensity by *counting the number of photons* that arrive at each pixel [45]. The number of photons received over a certain time is modeled as a Poisson process [45], resulting in a signal-to-noise ratio proportional to the *mean photon number*, before other noise terms, such as gain and circuit noise, are introduced [45].
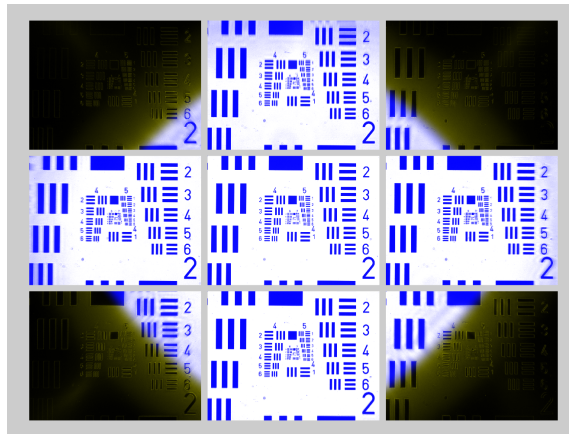
Figure 4.4: Verification of correct alignment. The red and green channels (i.e. yellow color) correspond to actual images, while the blue channel is the simulated BF region.

procedure generates a binary image describing where the BF regions are expected given a set of coordinates of the LEDs.

In Figure 4.4, the simulated binary BF maps are superimposed on actual measurements through an RGB image, where the collected images are displayed as yellow, while the simulated BF maps are blue, such that the overlap between the images and simulations will appear white. The figure demonstrates good alignment, as the edge between BF and DF regions appears in the same positions in both the blue and the yellow color channels of the image. However, a weak yellow region can be observed around the white region, indicating a less abrupt change between BF and DF than what is predicted by Equation (4.1). Note that (4.1) assumes that the Fraunhofer imaging model is valid. A simulation using the Fresnel imaging model would yield a more realistic result. Reflections from within the LED element could also affect the BF edge in a way similar to the observed result, since the effective source size would be larger, but still with most of the intensity originating from the real source.

4.4 Numerical and computational aspects

The theory that has been presented until now has relied on analytical functions to represent the different quantities. However, the algorithms will need to operate on discretely sampled images, introducing practical concerns.

The algorithms are implemented in Matlab R2018a, on a computer with an Intel Core i7-8700 processor and 32 GB RAM. The algorithms have not been optimized for speed, but rather readability, as the microscope is in an experimental stage of development. To increase the speed of the algorithms, a re-implementation using the graphics card of the computer could be considered.

4.4.1 Sampling optical fields

Following the Nyquist sampling theorem, as briefly presented in subsection 2.5.2, the required sampling grid period for coherent images is [50]

$$\Delta p \leq |M| \frac{\lambda}{2NA_{\text{obj}}},$$
(4.7)

where M is the magnification and Δp the detector plane pixel size. Given $\Delta p = 2.2\,\mu\text{m}$, and the specifications of the objectives given in Table 4.2, this criterion is easily fulfilled for both objectives.

The synthetically increased numerical aperture introduces a requirement for the chosen pixel size of the high resolution image[2] [50]

$$\Delta x \leq \frac{\lambda}{4NA_{\text{sys}}},$$
(4.8)

where Δx is the pixel size in the object plane. As $NA_{\text{sys}} \gg NA_{\text{obj}}$ for high-angle illumination, this criterion is easily violated if Δx is chosen as the raw pixel size, and consequently a smaller pixel size needs to be chosen to correctly sample the reconstructed field.

4.4.2 Sampling of quadratic phase factors

Using the Fresnel-3D algorithm, a quadratic phase factor in the object plane, $\exp[i\phi(x,y)]$, where

$$\phi(x,y) = \frac{k}{2z_1}(x^2 + y^2),$$
(4.9)

is multiplied with the exit field in Equation (3.37). $\exp(j\phi)$ will need to be sampled correctly in order to get the desired result. Following the sampling criterion of ref. [66], based on the requirement that the phase must not change by more than π between two sampling points, the required maximum pixel size becomes[3]

$$\Delta x \leq \frac{\lambda z_1}{L_x},$$
(4.10)

where L_x is the width of the sampled field in the x-direction. An equivalent criteria may be derived for Δy.

Considering a numerical example, with $z_1 = 40\,\text{mm}$, $\lambda = 520\,\text{nm}$ and a reconstructed area of $400\,\mu\text{m} \times 400\,\mu\text{m}$, the requirement would be $\Delta x, \Delta y \leq 52\,\mu\text{m}$. In practice, (4.10) will easily be fulfilled, as the sampling criteria presented in the previous subsection are much more stringent.

---

[2]The extra factor of 2 in the denominator is introduced since the reconstructed intensity should be possible to display. As $I = UU^*$, the Fourier spectrum of the intensity has twice the bandwidth of the complex field, as a multiplication in the spatial domain corresponds to a convolution in the frequency domain

[3]An equivalent criterion is derived from a bandwidth analysis in ref. [17].

4.4.3 Padding of arrays

In the multislice model, the angular spectrum propagation scheme is applied to propagate the exit field of one slice to the next slice. However, on a computer, a Fourier transform is replaced with a discrete Fourier transform (DFT), commonly implemented as a fast Fourier transform (FFT). For a discretely sampled function f, defined on an $M \times N$ grid, the 2D DFT is defined as [37]

$$\text{DFT}\{f(m,n)\} = \sum_{m=-M/2}^{M/2-1} \sum_{n=-N/2}^{N/2-1} f(m,n) \exp\left[-i2\pi \left(\frac{pm}{M} + \frac{qn}{N}\right)\right], \qquad (4.11)$$

with (m,n) being the indices in the real plane, and (p,q) being the indices in the Fourier plane.

An important difference between the discrete and analytical Fourier transforms is that the infinite limits of the analytical integral are replaced with finite limits in the sums. Thus, it is implicitly assumed that the value of f outside the limits of the sampling grid is zero. When applying the propagation scheme, this deviation will result in edge-defects. To overcome this limitation, a solution is padding the arrays, adding P new points around the original array, so that the $M \times N$ array is extended to an $(M + 2P) \times (N + 2P)$ array. In the case of propagating plane wave-like fields, as is done in both 3D FP algorithms, it is convenient to pad the absorption of the slices with 1's, ensuring that the computed field is surrounded by a plane wave on all sides. Thus, the region actually corresponding to the sample transmittance will not be affected by the edge defects.

4.4.4 Computational cost

The computational cost of a single 2D FFT operation is $2K^2 \log_2(K)$, when the input is a $K \times K$ complex array [17]. The additional operations have a negligible contribution compared to the FFT, so the analysis is based on the number of FFTs required to perform the algorithm. Assuming that there are M different illumination angles, and remembering that two FFTs are needed for each angle the cost of one iteration will be

$$\text{2D-COST} = 4MK^2 \log_2(K), \qquad (4.12)$$

for a single $K \times K$ section. In the supplement of ref. [1], an expression for the computational cost equivalent to (4.12) is derived.

The computational cost of the 3D FP algorithms is much larger than for 2D FP, due to multiple FFTs being performed when propagating the field between the slices. The pixel scaling factor, i.e. how much the pixel size is scaled in the high-resolution reconstruction is also of importance. Given a scaling factor of s, the cost of one sub-iteration (only one illumination angle) becomes

$$\text{3D-SUBCOST} = 4(2N - 1)s^2 K^2 \log_2(sK) + 4K^2 \log_2(K), \qquad (4.13)$$

for a $K \times K$ section of the image, using N layers in the multislice model. Each propagation operation is associated with two FFTs, and the propagation is performed on the scaled array, with size $sK \times sK$. Two additional FFTs are needed to model the imaging process, one of

which is performed on the reduced $K \times K$ array. In the updating steps, the same FFTs are performed in reverse order, so the cost must be multiplied by 2, resulting in the expression given in Equation (4.13). To follow the high-resolution sampling criterion, one typically needs $s \geq 2$, so the result may be simplified as the second term will be small compared to the first one. Completing M sub-iterations will then have a cost of

$$3\text{D-COST} = 4M(2N-1)s^2K^2\log_2(sK), \tag{4.14}$$

for a $K \times K$ pixels in the raw images.

Note that all pure multiplication operations are ignored in this analysis. The updating step of the 3D algorithms, for example, will involve multiple complex multiplication operations, and will also cause a significant cost. However, this analysis is merely an attempt to get an estimate of the time consumption for the different algorithms, and provide an approximate relationship between the selected section size and the expected time consumption. The impact of array padding by P pixels around the original array can be found by replacing K with $K + 2P$.

4.5   Sample description

To test the performance of the FPM, multiple samples are imaged: A United States Air Force (USAF) 1951 resolution target, a phase calibration target, a $4\,\mu\text{m}$ thick bone and cartilage slice, and a solution of $10\,\mu\text{m}$ (nominal) polystyrene beads in water.

4.5.1   USAF target

The USAF target, delivered by Edmund Optics [67], consists of a glass plate with deposited metal lines, decreasing in size closer to the center of the sample, and thus serves as a sample to quantify the resolution enhancement obtained with the FPM. To verify that the increased resolution is not limited to the center of the FoV, the USAF target was also imaged with the target center located in the upper left corner of the FoV.

Figure 4.5a displays an example layout of a USAF target. The target is divided in groups and elements, with the numbers above the lines (e.g. -2 and -1 in the figure) denoting the group numbers, and the numbers on the sides denoting the element number. Each group consists of six elements. The spatial frequency, $f_{G,N}$ (in lp/mm, where lp is short for line pair, i.e. a full period), of the line pattern in group number G and element number E can be found from the formula [68]

$$f_{G,N} = 2^{G + (N-1)/6}. \tag{4.15}$$

The finest element of the target is element 3 of group 9, meaning that the highest measurable spatial frequency is $645\,\text{lp}/\text{mm}$, which corresponds to a full-pitch resolution of $1.56\,\mu\text{m}$.

4.5.2   Phase calibration target

The phase calibration target, delivered by Phase Focus [69, 70], is $1\,\text{mm}$ thick plate of fused silica with etched rectangular features, as depicted in Figure 4.5b. The numbers are
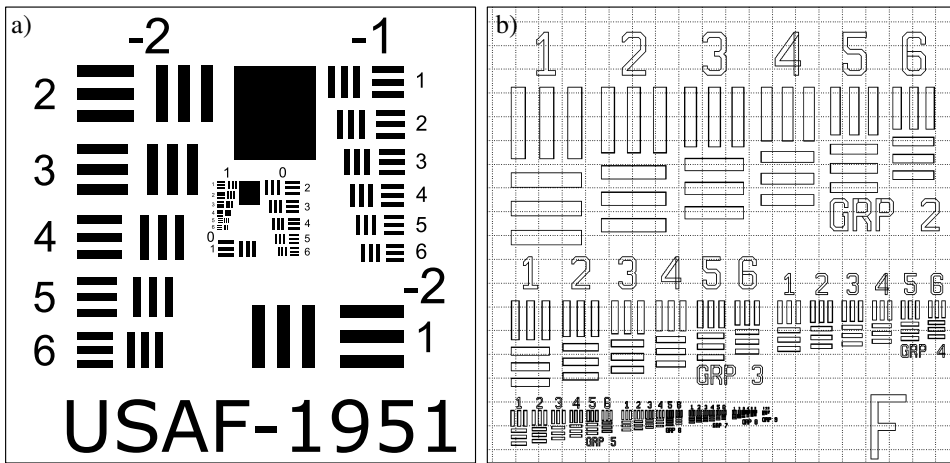
Figure 4.5: Layout of USAF target and phase calibration target. a) USAF target. Figure by Itzhak Baum, licensed under CC BY-SA 3.0. b) Phase calibration target. Ref. [69] is accredited for the sketch.

deposited metal. The etch depth is $(303 \pm 3)\,\mathrm{nm}$, and the refractive index of the fused silica is $n_{\mathrm{sil.}} = 1.467$ for $\lambda = 635\,\mathrm{nm}$. As the refractive index of fused silica is expected to change by less than 0.01 between the wavelengths of the different LEDs (470 to $625\,\mathrm{nm}$) [71], it will be assumed to be constant for calculations.

Since the glass is transparent, the etched depth is not directly measurable as the amplitude of the light is not changed with respect to the non-etched regions. However, the phase of a transmitted field will be different for the etched and non-etched regions, as the refractive index of air[4], $n_{\mathrm{air}} = 1$, is different from the refractive index of the quartz.

Similarly to the USAF target, the phase target is also divided into elements and groups. The feature sizes do not follow the same formula as for the USAF target. The highest spatial frequency of the phase target is $250\,\mathrm{lp/mm}$, corresponding to a full-pitch resolution of $4\,\mathrm{\mu m}$.

4.5.3 Polystyrene spheres

The polystyrene sphere sample consists of spherical beads of polystyrene with a nominal diameter of $10\,\mathrm{\mu m}$, diluted in water. The polystyrene spheres were delivered by Beckman Coulter [72]. Polystyrene has a refractive index of $n_{\mathrm{PS}} = 1.60$ for $\lambda = 520\,\mathrm{nm}$ [73], and the refractive index of water is $n_{\mathrm{wat}} = 1.33$ for the relevant wavelength range [74].

4.5.4 Bone and cartilage sample

The bone and cartilage sample consists of growth cartilage and subchondral bone from the femur of an 80 days old pig. The entire femur was formalin-fixed and stored in $70\,\%$ ethanol. The sample was cut into a block with sides of roughly $6\,\mathrm{mm} \times 4\,\mathrm{mm} \times 3\,\mathrm{mm}$,

---

[4]The refractive index of air is actually slightly larger than 1, but the value is so close that 1 is used.
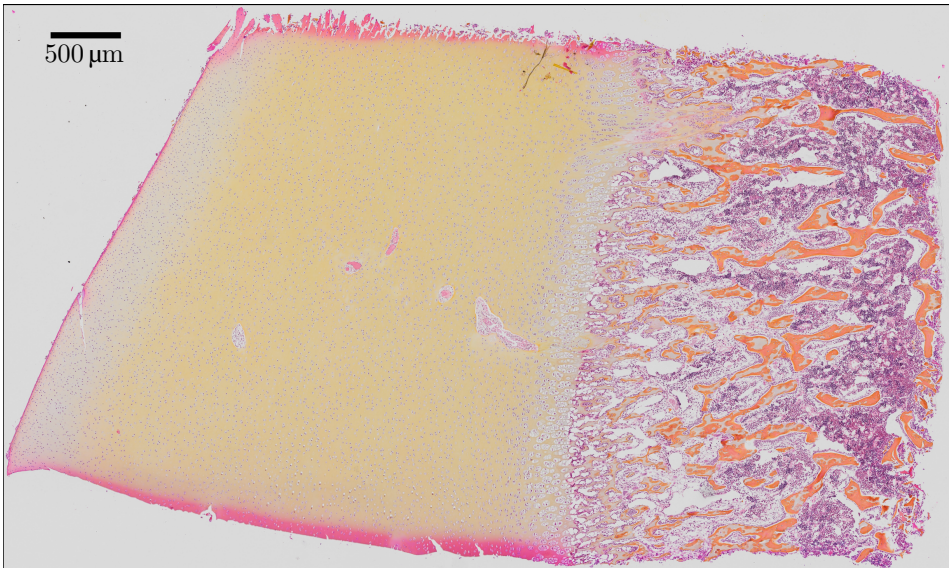
Figure 4.6: WSI image of a HES-stained bone and cartilage sample. The region to the left is the cartilage, while the right region is the bone

and prepared for finer cutting by decalcination and embedding in paraffin wax. The block was cut in $4\,\mu\text{m}$ thick slices, and the paraffin was removed. The slice was mounted on a glass slide with a cover slip.

The slice being studied in this thesis has not undergone further treatment. However, the neighboring slice was HES[5]-stained, in order to provide amplitude-contrast. Staining treatments are a common way to study such samples [75]. The stained slice was imaged in a WSI microscope, and the resulting image is shown in Figure 4.6.

4.6 FP imaging

The 2D datasets were acquired using the setup described in this chapter. For 3D FP, open source datasets acquired with a different setup is used.

4.6.1 Image acquisition

A single round of FP acquisition consists of capturing 293 images, each with a single LED turned on. The 293 LEDs correspond to a circular area on the LED matrix, with a diameter of $19d$ LEDs, d being the LED pitch. The LED matrix was positioned $z_{\text{LED}} = 140\,\text{mm}$ from the focus plane of the objective, corresponding to a maximum illumination angle of $21.1°$, resulting in an illumination NA of $NA_{\text{illu}} = 0.36$. An illustration of the sampling pattern in Fourier space can be found in Figure 4.7.

---

[5]HES: hematoxylin eosin saffron
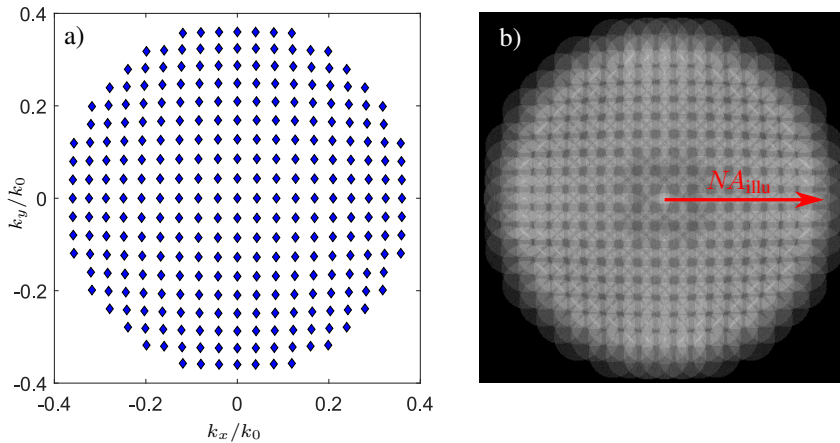
Figure 4.7: Sampling pattern in the Fourier domain. a) The frequencies of the 293 LEDs. b) Overlap in Fourier space.

With the 0.055 NA of the 2X objective, most of the acquired images are DF images. The intensity of the DF signals are typically much lower than the BF images, so in order to get an appreciable signal-to-noise ratio (SNR) the exposure time is increased for the DF images.

Two rounds of image acquisitions are done for each LED, with different exposure times, to create a high dynamic range (HDR) image[6]. The HDR combination process reduces noise, and avoids artifacts resulting from saturation of the detector. The exposure times were varied for the different experiments, due to differences in absorption between different samples. However, a general rule of thumb is that BF images were acquired with exposure times of roughly $40\,\mathrm{ms} + 15\,\mathrm{ms}$ and DF with $150\,\mathrm{ms} + 50\,\mathrm{ms}$. Acquiring a full set of images takes a total of 2-3 minutes.

Unless otherwise noted, the green LEDs, with $\lambda = 520\,\mathrm{nm}$ were used in the imaging process.

The relevant variables of the acquisitions are summarized in Table 4.3

4.6.2   2D Reconstruction

The reconstructions were performed for a total of 10 iterations, and convergence was quantified by calculating the sum of square errors (SSE) error between simulated images and acquired images,

$$\mathrm{SSE} = \sum_{m} \sum_{x,y} \left[|U_m(x,y)| - \sqrt{I_m(x,y)} \right]^2 , \tag{4.16}$$

where U_m is the simulated field for the mth illumination angle and I_m is the actual measurement.

---

[6]The HDR requirement may be circumvented by applying a binary mask in the updating step, as decribed in ref. [58].

Table 4.3: Imaging parameters

Parameter	Value
z_{LED}	$140\,\text{mm}$
LED diameter	19
LED pitch	$6\,\text{mm}$
Number of images	293
NA_{obj}	0.055
NA_{illu}	0.36
Typical BF exposure	$40+15\,\text{ms}$
Typical DF exposure	$150+50\,\text{ms}$
FoV	$2.8\,\text{mm} \times 2.1\,\text{mm}$

To fulfill the coherence requirements as well as the plane wave assumption, a limited section of the images, typically $256\,\text{pixels} \times 256\,\text{pixels}$, equivalent to $282\,\mu\text{m} \times 282\,\mu\text{m}$, was chosen since the FFT algorithm is the fastest when the size of the input is a power of 2 [37]. The coherence areas, A_c, cf. Equation (2.39), of both R, G and B LEDs, given in Table 4.1, are larger than the section selected. The illumination was treated as monochromatic, with λ as given in Table 4.2.

The images are processed in the NA order [76], i.e. the images with the lowest illumination angles are treated first, and the widest angles last. In order to fulfill the sampling requirements, a scaling factor of 4 is used when initializing the high-resolution image, meaning that a single pixel in the raw images will be equivalent to $4 \times 4 = 16$ pixels in the synthesized image.

For large FoV reconstructions, the total area is divided into smaller segments, each fulfilling the coherence requirement and where the plane wave assumption holds. A 10 pixel overlap between neighboring segments is used, and in the overlapping area, a weighted combination of the two segments forms the final image, as described in the appendix of ref. [1]. The overlap method ensures smooth edges between the different segments, as opposed to what is obtained when no overlap is used.

Digital defocus correction was tested, using a scheme similar to that presented in ref. [10], where the defocus distance was found by performing multiple reconstructions with different known defocus aberrations, with a limited data set to speed up the process, and the regular FP algorithm. To simulate a defocus aberration, the angular spectrum propagation scheme, see subsection 2.2.1, was used to modify the pupil. With the angular spectrum transfer function, given by Equation (2.20), the generalized pupil function used in the reconstruction was

$$\mathcal{P}(f_x, f_y) = P(f_x, f_y) \exp\left(ikz_{\text{d}}\sqrt{1 - (\lambda f_x)^2 - (\lambda f_y)^2}\right), \qquad (4.17)$$

where z_{d} is the defocus distance. The correct value of z_{d} was found by minimizing the error metric given by Equation (4.16). To test the validity of this scheme, a stack of images were collected with the sample placed at a defocus distance $z_{\text{d}} = 100\,\mu\text{m}$ from the focus plane.

4.6.3 3D reconstructions

For the 3D reconstructions, the dataset used in ref. [6] is used as input to the reconstruction algorithms. The dataset is provided by the authors, Tian and Waller, as open source data[7]. The quasi-3D sample consists of two stacked USAF targets, separated by a distance of $110\,\mu m$, with one target slightly rotated with respect to the other.

The experimental setup is described in ref. [6], as well as in a text file accompanying the open source dataset: The images were captured using a Nikon TE300 inverted microscope with a PCO.edge camera with a bit depth of 16 . The objective has a 4X magnification and $NA_{obj} = 0.1$. The angled illumination is provided using an LED matrix with a $4\,mm$ LED pitch, and the red LEDs with a wavelength of $\lambda = 643\,nm$ is used. The matrix is placed $z_{LED} = 75.5\,mm$ from the sample. The emitting region of the LEDs are $120\,\mu m \times 120\,\mu m$, leading to a coherence area of $405\,\mu m \times 405\,\mu m$, following Equation (2.39). Factoring in magnification, the object plane pixel size is $0.813\,\mu m$, clearly fulfilling the raw image sampling criterion specified by Equation (4.7). 293 images are captured, corresponding to a circle of radius 19 on the LED matrix, resulting in $NA_{illu} = 0.41$. A $390\,\text{pixels} \times 390\,\text{pixels}$ section of the full FoV was selected, corresponding to $317\,\mu m \times 317\,\mu m$ in the object plane, which is within the coherence area. The section size was chosen to mimic the reconstructed section in ref. [6].

No dark image, I_D is given in the open source data, so the noise reduction step described by Equation (4.3) was ignored for these images. The thresholding step, described by Equations (4.5) and (4.6) were performed for all the DF images.

Reconstructions were performed using both of the described 3D algorithms, and the results were compared to determine the relative performances of the algorithms.

As for the 2D reconstructions, the illumination angles are treated in the NA order. 5 iterations were performed for both algorithms. For the Fresnel-3D algorithm, knowledge of the z_1 parameter is required. As z_1 was unknown, a method analogous to the defocus correction previously described was employed: reconstructions are performed for a range of z_1 values, and the selected value is the one that minimizes the SSE. It is also noted that the Fresnel model assumes single lens imaging, while a complex microscope objective is used in the experiments.

---

[7]As of May 2019, the datasets are available at `http://www.laurawaller.com/opensource/` or `http://sites.bu.edu/tianlab/open-source/`.

FPM results and discussion

This chapter presents the obtained results from the experimental FP microscope, as well as the results from reconstructions of the open source data of a 3D sample.

5.1 Resolution enhancement

To quantify the resolution enhancement, the reconstructions involving the USAF target are used as a basis. Figure 5.1 displays the reconstructed amplitude compared to both coherent and incoherent images. Both when the target is positioned in the center of the FoV (Figure. 5.1b) and in the corner of the FoV (Figure 5.1c), the reconstruction shows completely resolved lines in element 3 of group 9 on the target, corresponding to a full-pitch resolution of $1.56\,\mu m$. Note that the achieved resolution is the finest resolution that can be measured with the USAF target, so the real resolution of the system may be even better.

The resolution enhancement may also be expressed by the increased cutoff frequency in the Fourier domain of the sample transmittance. Using equation (2.62), the synthetic NA of the system is 0.33. Assuming that the resolution gain is constant across the entire FoV, which is a reasonable assumption as this has been demonstrated both in the center and the corner of the FoV, the observed SBP enhancement factor is 9 compared to incoherent imaging, and 36 compared to coherent imaging, using Equations (3.15) and (3.14). The theoretical enhancement factors are 14 and 57, respectively. Note that the discrepancy between measured and theoretical values may be attributed to the resolution target limit.

Figure 5.2 displays the achieved resolution as a function of illumination NA, compared to the theoretical value given by Equation (3.13). The observed resolution is seen to strongly correlate with the theoretical model for $NA_{\mathrm{illu}} < 0.3$. For higher NA_{illu} the measured resolution is constant, since the limit of the resolution target is reached. However, the strong correlation for lower NA_{illu} demonstrates that the obtained resolution enhancement is close to the theoretical prediction.
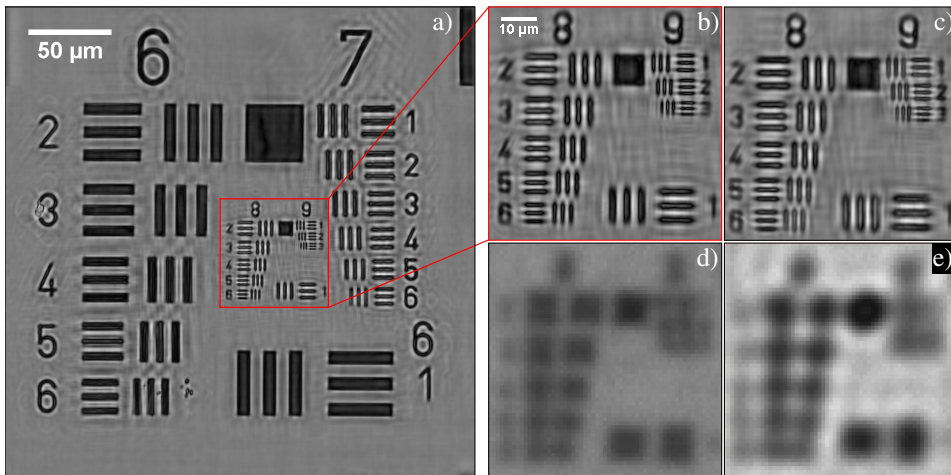
Figure 5.1: Reconstruction of USAF target. a) The full reconstructed section, displaying groups 6 and higher. b) The central part of the reconstruction, showing that all elements are perfectly resolved. c) The same reconstructed section of a USAF target, imaged with the target in the corner of the FoV. d) The same section of an incoherent image captured with the same equipment, and e) a coherent image. The differences in color tone is a result of different scaling of the images, and should not be interpreted as a physical difference.
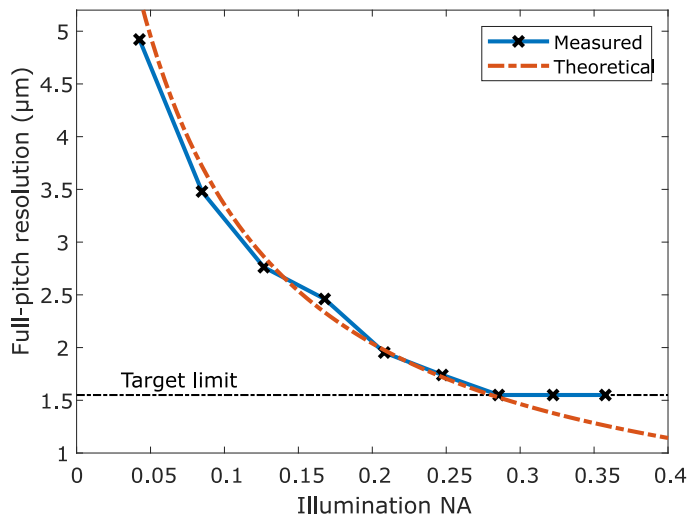
Figure 5.2: Measured resolution compared to theoretical resolution for EPRY-FP, using $NA_{\mathrm{obj}} = 0.055$ and $\lambda = 520\,\mathrm{nm}$.
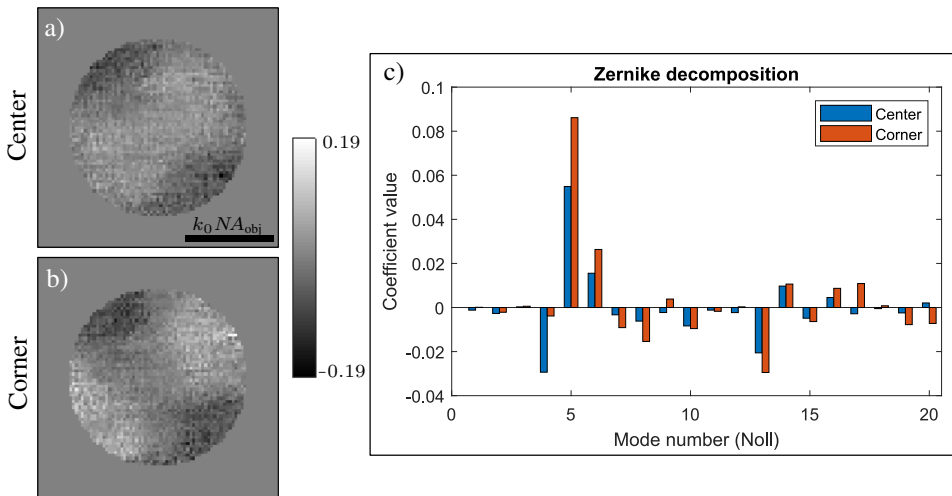
Figure 5.3: Recovered phase aberrations in the center and the corner of the FoV. a) The center pupil. b) The corner pupil. The unit of the colorbar is radians, and the radius of the pupil is $k_0 NA_{obj}$. c) Zernike coefficients for the two pupil functions shown in a) and b). The mode number refers to Noll's sequential ordering scheme [46].

5.1.1 Pupil recovery

The EPRY algorithm simultaneously recovers the aberrations of the imaging system and the complex transmittance of the sample. For the USAF target, the recovered wavefront aberrations are shown in Figure 5.3. The images show the phase of the recovered pupil. With the basis in the generalized pupil function, stated in Equation (2.61), the phase is expressed as kW.

The aberrations of an imaging system are expected to be more significant towards the center of the FoV than near the edge [9], and the same result is obtained when recovering the pupil function in the center and the corner of the FoV. Figure 5.3a shows the recovered center pupil, which can be seen to be quite flat, as is expected for a high-quality microscope objective. The corner pupil, displayed in Figure 5.3b, shows a significant increase in aberrations, especially towards the upper right and lower left regions of the pupil.

To further study the recovered pupil functions, a Zernike decomposition was performed, displayed in Figure 5.3c. The coefficients were found using matrix inversion. As the strength of the aberration is relatively weak (cf. the colorbar in Figure 5.3), the values of the Zernike coefficients are small in absolute value, but the relative contributions from the different modes vary strongly. For the center reconstruction, mode number 4, corresponding to a defocus term [46], has a significant contribution, indicating that the sample was slightly out of focus when acquiring the images. The contributions from astigmatism terms, mode number 5 and 6 [46], is significant for both the center and corner pupil. However, the astigmatism coefficients are significantly higher for the corner pupil, which is reasonable, as the astigmatic difference increases with larger distances to the optical axis [21]. There is also a notable coefficient value for mode number 13 for both of the recovered pupils.
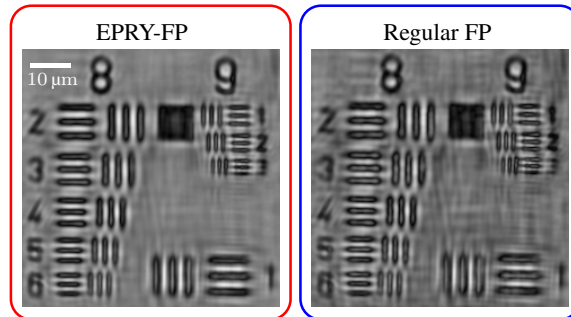
Figure 5.4: Comparison of the reconstructed amplitude using EPRY-FP and regular FP.

Recovering the pupil also positively affects the reconstructed transmittance. In Figure 5.4, reconstructions of the USAF target placed in the corner of the FoV is shown, both using EPRY-FP and regular FP algorithms. While both reconstructions demonstrate perfectly resolved elements in groups 8 and 9, the EPRY-result demonstrates less background noise, as well as more clearly resolved element numbers.

Provided the EPRY algorithm recovers the aberrations correctly, the recovered pupils could be saved and used as input pupils for subsequent reconstructions, in order to speed up the convergence. While the added steps in the EPRY algorithm compared to the regular FP algorithm have an insignificant contribution to the time consumption, fewer iterations may be needed to reach convergence. This measure has not been taken in this thesis, as the added time consumption from the EPRY-modifications is negligible when only recovering single sections.

5.1.2 Defocus correction

Figure 5.5a displays a plot of SSE as a function of defocus distance for a set of images of the USAF sample manually displaced $100\,\mu m$ from the focus plane. The minima of the SSE is found for $z_d = 105\,\mu m$, indicating that the defocus distance is $105\,\mu m$, which is close to the known offset. Due to the large depth of field (DoF) of the microscope, i.e. $91\,\mu m$ (see Table 4.2), the $5\,\mu m$ difference is not significant, as it is difficult to manually find the exact plane of focus.

A reconstruction of the defocused dataset led to the resulting amplitude shown in Figure 5.5b, displaying a clearly degraded reconstruction, where the overall quality of the reconstructed image is bad, and the features appear quite different from the known amplitude distribution (cf. Figure 5.1b). Using the pupil given by Equation (4.17), with $z_d = 105\,\mu m$ as input pupil to the EPRY algorithm, the result, shown in Figure 5.5c, demonstrate clearly resolved lines in all elements, with the expected amplitude distribution.
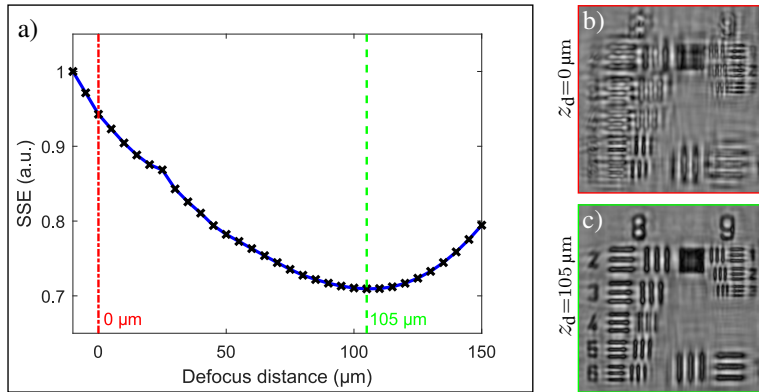
Figure 5.5: Defocus correction with FP. a) SSE plotted against defocus distance. b) and c) recovery performed with $z_\mathrm{d} = 0\,\mu m$ and $z_\mathrm{d} = 105\,\mu m$, respectively. The scale bar in Figure 5.4 may be consulted for scale.

5.2 Quantitative phase imaging

5.2.1 The phase target

To verify the quantitativity of the reconstructed optical phase, the phase calibration target, presented in subsection 4.5.2, was imaged.

The reconstructed phase of the phase target is shown in Figure 5.6a, demonstrating a phase map similar to the expected depth distribution. The Figure shows groups 7 through 9 of the target, with spatial periods ranging from 4 to $18\,\mu m$. The etched regions (the vertical and horizontal bars in the figure) have a negative phase compared to the surrounding region, indicating that the optical path length when passing through the etched regions is shorter than for the pristine regions.

The finest feature of the target, i.e. element 3 of group 9, the rightmost bars in Figure 5.6a, have a period of $4\,\mu m$, demonstrating the the FPM has a full-pitch resolution of at most $4\,\mu m$ for pure phase elements. From Figure 5.6a, it appears as all of the elements in image is resolved correctly, indicating that the phase reconstruction technique is suitable for this range of spatial frequencies.

Figure 5.6b displays a line plot of the computed height profile across element 1 of group 9 (the red arrow in Figure 5.6a). The plot is computed by interpreting the phase as an optical path difference (cf. subsection 2.1.3 and specifically Equation (2.12)), setting the zero level at the pristine region and using the known $n_\mathrm{sil.} = 1.467$ of the material. The plot clearly demonstrates the correct trend for both red, green and blue LEDs. However, the known height profile is a square wave that alternates between $0\,nm$ and $-303\,nm$ (the dashed lines in the figure).

The reconstructed shape is similar to correct profile, albeit with notable deviations, for example the far-from-zero values of the reconstructed plots between the etched wells. A possible source for this error can be Fresnel reflection off the sidewalls of the wells, due to the illumination forming an angle towards the wall of 0 to $21°$. In Figure 5.6a it can be seen
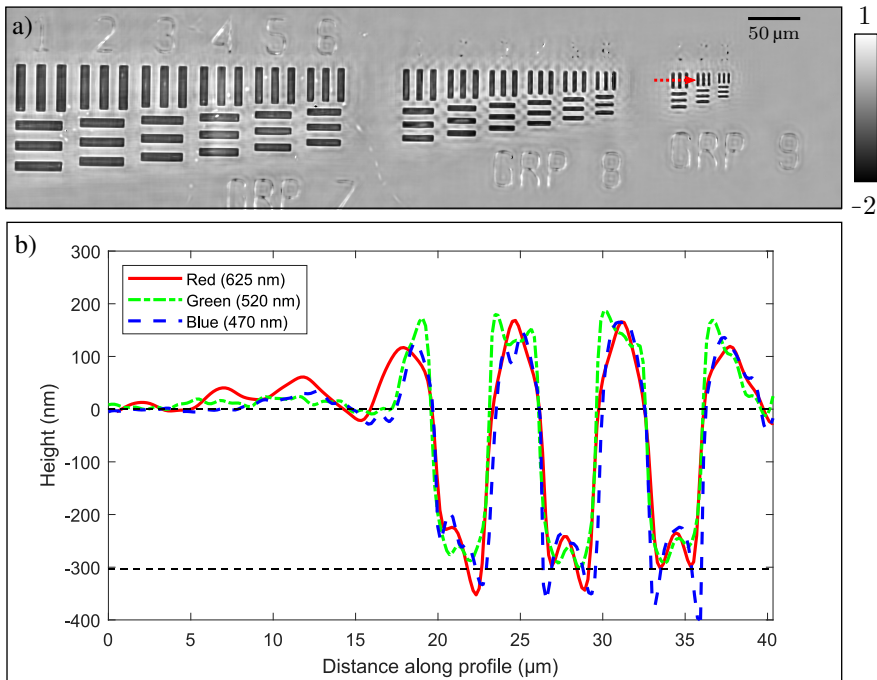
Figure 5.6: Reconstructed section of the phase target. a) The reconstructed phase of groups 7 through 9 of the phase target, using $\lambda = 520\,\text{nm}$. The red arrow indicates the direction of the profile plot displayed in b), i.e. through element 1 of group 9. The profile plot in b) displays the reconstructed height profile for both red, green and blue LEDs. The unit of the colorbar is radians.

that this *overshooting* is observed for lower frequency elements as well, seen as a bright border around the rectangles, making edge effects, such as reflection, a likely source of this error. Another possible error source is the extended path difference perceived by the angled rays; a ray passing through the sample with an angle θ towards the optical axis will have to travel an extra distance inside the glass of $d/\cos\theta \geq d$, where d is the etch depth. Note that refraction when entering and exiting the glass plate has been ignored in this simple explanation.

The plot in Figure 5.6b also demonstrates how ripples are observed in the computed height profile beside the elements. The height profile tend towards 0 as the distance from the etched wells increases, but close to the element, large deviations from the ideal profile is observed. The ripples appear to be stronger for red illumination, which corresponds to the largest wavelength, and thus the lowest cutoff frequency, indicating that the ripples may be due to the abrupt coherent cutoff. The abrupt cutoff may also be a reason for the observed overshooting.

Ignoring the artifacts of the reconstruction, the computed depth of the etched wells are close to the known level (relative to the zero-level). For all $\lambda =$, the computed depths are in the range 250 to $350\,\text{nm}$ for all three wells, which is close to the expected value of $303\,\text{nm}$. This example highlights the usefulness of QPI techniques; using a wavelength of $\sim 0.5\,\mu\text{m}$,
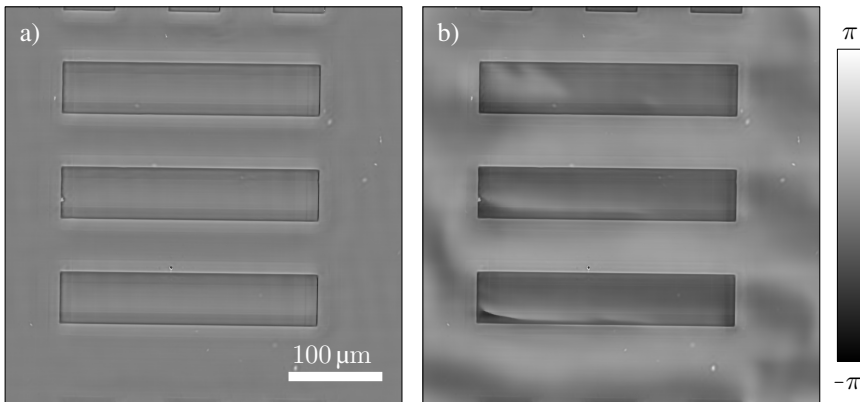
Figure 5.7: Low-frequent phase recovery of element 3 in group 3 on the phase target. a) Reconstruction when ignoring the BF edge sections. b) reconstruction when including the BF edge section. The color bar is in unit of radians.

one is able to reconstruct a phase profile with a height resolution $\sim 100\,\text{nm}$.

5.2.2   Low-frequent phase recovery

The phase target also contains larger features than those displayed in Figure 5.6a, as displayed in the schematic layout presented in Figure 4.5b. Reconstructing low-frequent phase information has proved to be difficult task, an example of which can be seen in Figure 5.7a, displaying an ordinary reconstruction of the horizontal bars of element 3 in group 3 of the phase target. These bars have a width of $55\,\mu\text{m}$, corresponding to a spatial frequency of $9.1\,\text{lp/mm}$. In the figure, the contour of the bars are clearly visible, but the phase *inside* the bars is seemingly the same as the phase of the outside region.

The reconstruction in Figure 5.7a has been performed following the method described in subsection 4.6.2, i.e. ignoring the sections of images close to the BF edge. However, when the BF edge region is included in the reconstruction, the low-frequent components reappear, as shown in Figure 5.7b. The latter figure also illustrates why the BF edge images commonly are left out of the reconstructions, as the image contains a lot of noise.

The problem of low-frequent phase reconstructions has been investigated by Sun et al. [11], under the assumption of a weak object[1], with the result that BF edge LEDs are essential for FP recovery of low-frequency phase information. More specifically, the phase transfer function (PTF), describing how phase information is transferred to the spectrums of the measured intensities, will not allow low frequencies to pass through the filtering process unless the angle of illumination exactly matches the BF angle of the objective [11].

The low-frequent information loss is further investigated in simulations, to verify if the weak object results also hold for more general objects. For a pure phase object, the complex transmission function is $t(x,y) = \exp[i\phi(x,y)]$, where ϕ describes the phase distribution. Following the derivation in ref. [11], the spectrum of the collected bright field intensity

---

[1]An object with low absorption, A, and a small phase shift, ϕ, so the transmission function may be approximated as $t = \sqrt{A}\exp\{i\phi\} = \exp\left(\frac{1}{2}a + i\phi\right) \approx 1 + \frac{1}{2}a + i\phi$, where $a = \ln A$ [11].

Phase spectrum, $|\Phi|$ Weak approximation, $\left|G_{I_m}^{\text{weak}}\right|$ Strong object, $\left|G_{I_m}\right|$
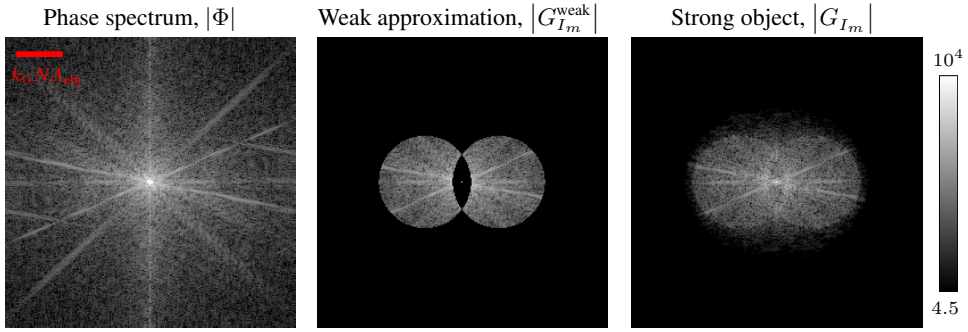
Figure 5.8: Simulation of phase information transfer for a pure phase object when imaging with tilted illumination from a single LED with $k_{xm} = 0.8k_0 NA_{\text{obj}}$ and $k_{ym} = 0$. The figure shows how parts of the phase spectrum is transferred to the collected intensity images under the weak approximation, Equation (5.1), and for a general object, Equation (5.2). The colorbar is logarithmic, in arbitrary units.

image, $G_{I_m}^{\text{weak}}$, is

$$G_{I_m}^{\text{weak}}(\mathbf{k}) = \delta(\mathbf{k}) + i\Phi(\mathbf{k})[\mathcal{P}(\mathbf{k} + \mathbf{k}_m) - \mathcal{P}(\mathbf{k} - \mathbf{k}_m)], \qquad (5.1)$$

where a vector notation has been adopted for the 2D frequency coordinates, $\mathbf{k}_m$ denotes the 2D wave vector of the mth LED, and $\Phi = \mathcal{F}\{\phi\}$. For a general object without the weak approximation, described in subsection 3.1.1, the intensity spectrum, G_{I_m} is

$$G_{I_m}(\mathbf{k}) = \mathcal{F}\{I_m(\mathbf{x})\}, \qquad (5.2)$$

with I_m given by Equation (3.3), and $\mathbf{x}$ is the 2D spatial coordinate.

For a strong phase object ($\phi : \mathbf{x} \mapsto [-\pi/2 , \pi/2]$ has been used in the simulations), Equations (5.1) and (5.2) have been evaluated assuming an aberration free system, $\mathcal{P} = P$, and $S_m = 0.8$ in the x-direction, adopting the notation from Equation (4.2). The results are shown in Figure 5.8. The upper and lower limits of the intensity scale have been adjusted to highlight the interesting features, making weaker signals less visible in the figure.

In terms of phase information transfer, it is clear that under the weak approximation, the two pupil function components in (5.1) cancel out near the center, blocking low-frequent components of the phase spectrum. Assuming multiple BF LEDs are used, the region of Φ where

$$\frac{|\mathbf{k}|}{k_0} < NA_{\text{obj}}(1 - S_{\text{max}}) \qquad (5.3)$$

will not be transferred to the intensity images, and the reconstructed amplitude will lack important information regarding the low-frequency components of Φ. S_{max} is the maximum value of S_m. To faithfully recover Φ, LEDs with S_m equal or very close to 1 must be included in the reconstruction[2].

Considering the spectrum for the strong object, also shown in Figure 5.8, it is evident that strong similarities with the weak approximation spectrum is observed. A notable

---

[2]Note that the direction of the LED wave vectors are also of importance, which is not accounted for in (5.3).

difference is the relatively bright region in the overlap between the two circles, in the strong object spectrum. This observation indicates that the result obtained for a weak object can not be generalized to a strong object. On the other hand, the observations do not prove that low-frequent phase information is transferred for the given illumination angle; the observed intensity in the center of G_{I_m} may occur due to higher order terms (cf. ref. [11]), and may not be a direct map of the phase spectrum, Φ. To determine the phase information transfer for strong objects, further studies are needed.

Revisiting the recovered phase displayed in Figure 5.7, it is evident that the low-frequent information is not recovered correctly in a) when the BF edge LEDs are ignored. Considering the criteria specified in Equation (4.2), i.e. ignoring LEDs with $S_m \in (0.94, 1.15)$, the remaining BF LEDs have $S_{\max} = 0.86$. It is expected from (5.3) that frequencies below $15\,\mathrm{lp/mm}$ are unaccounted for. Thus, it is reasonable that the lines, with a frequency of $9.1\,\mathrm{lp/mm}$, are not resolved correctly without including the BF edge images. For the phase target, the expected phase shift between the etched and pristine regions is $1.81\,\mathrm{rad}$, meaning that the phase target does not qualify as a weak object. However, the criterion developed for a weak object successfully predicts which frequencies that can and can not be recovered.
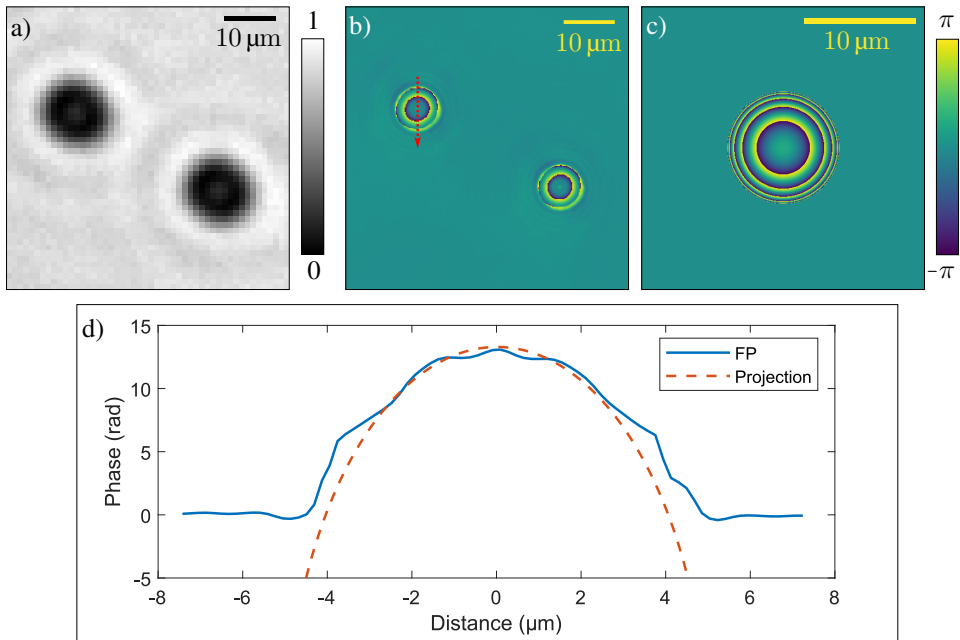
5.2.3 Polystyrene beads

The sample of polystyrene beads ($n_{\mathrm{PS}} = 1.60$), with a diameter of $10\,\mu\mathrm{m}$, immersed in water ($n_{\mathrm{wat}} = 1.33$), was imaged with the FPM. The resulting phase profile, accompanied by a simulated theoretical phase profile, is shown in Figure 5.9. In Figure 5.9b, the phase of two neighboring spheres are shown. It is evident that the phase has *wrapped*: the phase has increased beyond $+\pi$, leading to it being interpreted as $-\pi$, since $\exp[i(\phi + 2\pi n)] = \exp[i\phi]$ for any integer n. The reconstructed phase map is compared with a theoretical model, termed the projection model.

The projection model is based on the OPD of different paths through the sphere with respect to a path outside the sphere, assuming linear propagation through the sphere and no reflection or refraction. From the projection method, displayed in Figure 5.9c, it is evident that the polymer bead is a strong phase object, providing a large phase shift over a short distance near the edge of the sphere, resulting in the phase wrapping 3 times over this short distance. In the FP result, seen in Figure 5.9b, these outer wrappings are lost. The loss of the observable phase wrap does not mean that the optical path length through the center of the sphere is reduced, it is simply a result of a large difference in optical path length, and the inability to distinguish whether a multiple of 2π has been added or not.

The line plot displayed in Figure 5.9d compares the phase profile of the reconstruction to the simulated model. A phase unwrapping technique[3] has been used to unwrap the phases. Note that 6π has been subtracted from the projection model phase, to compensate for the loss of three phase wraps in the measured phase. It can be seen that the FP reconstruction correlates well with the projection model close to the center of the sphere, but the deviation between the two curves increases close to the edge of the beads, where the projection model has a steep gradient.

Consulting the thickness criteria for the 2D approximation, plotted in Figure 3.4, the

---

[3]The built-in `unwrap` function in Matlab was used. $\pm 2\pi$ was added whenever the difference between two subsequent points is $> \pi$.

Figure 5.9: Phase reconstruction of $10\,\mu m$ polystyrene beads in water compared to theoretical model. a) Section of a raw intensity image used for the reconstruction, b) The reconstructed phase of two polystyrene beads, with the red arrow indicating the direction and location of the profile plot. c) Theoretical phase profile from a projection model. d) Line plot of the unwrapped phase across the reconstructed sphere, compared to the projection model. Note that 6π has been subtracted from the profile of the projection model to line it up with the measured profile. The intensity colorbar is in arbitrary units, while the phase colorbar is in radians.

maximum thickness for $NA_{\mathrm{illu}} = 0.36$ is 7.5λ and 30λ, for the Lee and Thibault thickness criteria, respectively. Given the illumination wavelength of $\lambda = 520\,\mathrm{nm}$, it is clear that the former criterion is violated for a $10\,\mu m$ sphere, while the latter criterion holds. Thus, the failure to resolve the steepest part of the phase may be a result of the multiplicative approximation breaking down. The large difference in refractive index between the medium and the spheres will cause a significant contribution from reflection, which is not accounted for in the projection model.

The reconstructed phase appears less smooth than the projection model. This difference may originate from a defocus error. In practice, a defocus error is equivalent to propagating the field over a short distance, leading to interference, and the formation of peaks. Another source for this mismatch may be the low-pass filtering of the signal: Even though FP vastly extends the synthetic aperture, the aperture still acts as a low pass filter, but the cutoff frequency is increased. A hard phase object, such as the $10\,\mu m$ sphere, will contain high-frequent components that will not be recovered in the FP reconstruction process, a concept that is further investigated in the next subsection.

5.2.4 Phase gradient limit

The highest reconstructed frequency of the FPM is $k_c^{\mathrm{FP}} = k_o NA_{\mathrm{sys}}$, with NA_{sys} given by Equation (3.11). Considering a 1D phase distribution, $\phi(x)$, the highest frequency of the wave, $\exp[i\phi(x)]$, is

$$k_{\mathrm{max}} = \left| \frac{\mathrm{d}\phi}{\mathrm{d}x} \right|, \tag{5.4}$$

and in order to faithfully recover ϕ, the maximum phase frequency must be smaller than the cutoff frequenc: $k_{\mathrm{max}} \leq k_c^{\mathrm{FP}}$, or equivalently.

$$\left| \frac{\mathrm{d}\phi}{\mathrm{d}x} \right| \leq k_0 NA_{\mathrm{sys}}. \tag{5.5}$$

Relating the phase gradient to an optical path difference, the criterion can be reformulated in terms of a thickness gradient,

$$\left| \frac{\mathrm{d}t}{\mathrm{d}x} \right| \leq \frac{NA_{\mathrm{sys}}}{\Delta n}, \tag{5.6}$$

where t is the thickness of an object immersed in a medium, and $\Delta n = n_{\mathrm{object}} - n_{\mathrm{medium}}$.

For spherical objects, the thickness gradient will be infinite at the edge of the object. This is, however, not a fundamental concern, as the analytical limit is not reached in a digital representation of the phase. The discrete gradient, will be finite, as long as the pixel size is larger than zero.

For the $10\,\mu\mathrm{m}$ polystyrene beads, the thickness gradient limit is 1.54, given $NA_{\mathrm{sys}} = 0.41$ and $\Delta n = 0.27$. For a perfectly spherical bead with radius $a = 5\,\mu\mathrm{m}$, this limit is reached when the distance from the center of the sphere exceeds $0.61a = 3.1\,\mu\mathrm{m}$. Thus, the FPM is not expected to correctly resolve the phase of the light passing through the $10\,\mu\mathrm{m}$ beads near the edge of the beads, a result that can explain the difference between the measured phase and the OPD-based model. Consulting the plot in Figure 5.9d, it can be seen that the recovered phase is similar to the theoretical model in the center of the bead, and until a distance from center of $\sim 3\,\mu\mathrm{m}$, which is close to the theoretically predicted limit of $3.1\,\mu\mathrm{m}$.

5.3 Bone and cartilage sample

A full FoV reconstruction of the $4\,\mu\mathrm{m}$ thick bone and cartilage slice is shown in Figure 5.10, with some regions enlarged and compared to an incoherent image of the same sample. It is evident that the FPM radically increases the contrast and resolution in the images. The enlarged features are barely visible in the incoherent intensity images, likely due to the low absorption of the sample. However, the phase reconstructions show clearly defined features with high resolution, across the entire FoV of the microscope.

The full FoV reconstruction clearly demonstrates how the FPM can be used to image real samples with a large SBP. With the specified setup, the SBP of the imaging system is, according to Equation (2.63), $14.8\,\mathrm{MPix}$, assuming the bandwidth is determined by the system NA, as given by (3.11). This is not extraordinary, but a vast increase when
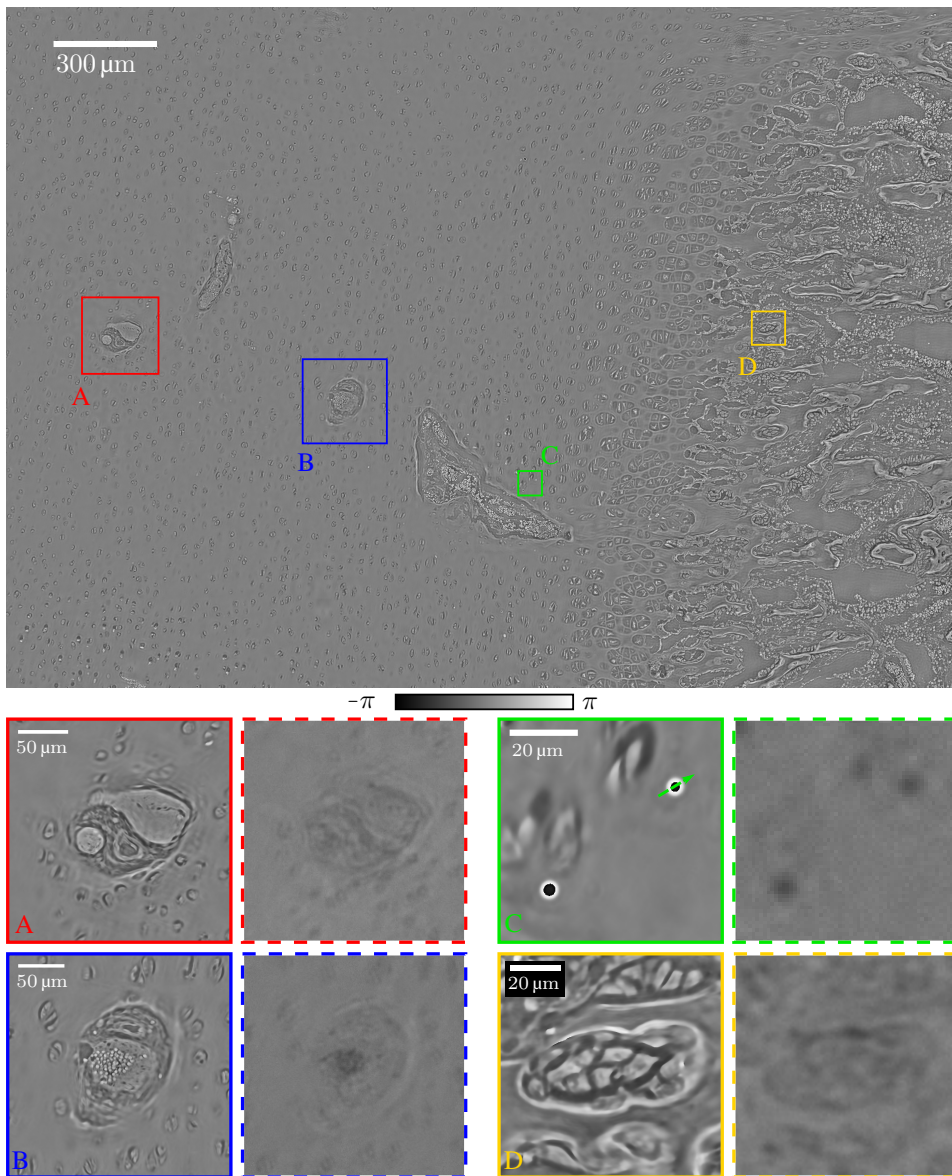
Figure 5.10: Full FoV phase reconstruction of bone and cartilage sample. The upper part of the figure shows the entire FoV of the microscope. The marked regions are enlarged and shown separately in the bottom region, compared to incoherent intensity images of the same sections, shown in dashed frames. The colorbar is only valid for the phase reconstructions, and the unit is radians.
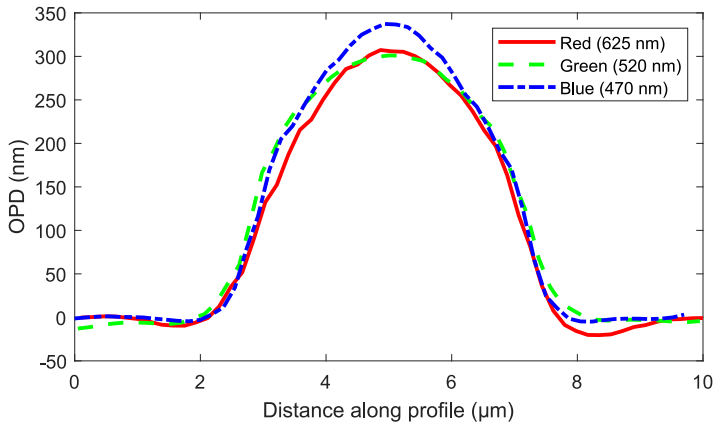
Figure 5.11: OPD along line trace of a circular object in the cartilage sample. The direction of the line trace is shown by the arrow in Figure 5.10, in the zoom-in of section C.

comparing with the SBP of the microscope when it is simply used for incoherent imaging: $1.1\,\text{MPix}$. The SBP of the FPM is limited by the physical size of the imaging sensor, which is small compared to the potential FoV of the objective. Replacing the $1/2''$ image sensor with a larger sensor could drastically increase the FoV. If the FoV was of similar size to that presented in ref. [1], namely $\sim 120\,\text{mm}^2$, the achieved SBP would be $0.21\,\text{GPix}$, assuming the resolution gain remained constant.

To demonstrate the usefulness of the QPI aspect of the FPM, a line trace is performed along the circular object displayed in region C of Figure 5.10. The phase is reinterpreted as an optical path difference, with a reference phase being the phase value of the extracellular matrix, i.e. the material surrounding the object. Equation (2.12) is used to translate the phase difference into an OPD. The resulting plot is shown in Figure 5.11, demonstrating the OPD profile for all three wavelengths of the LEDs. While all three profiles are similar, the profile resulting from the reconstruction with $470\,\text{nm}$ shows a significantly different peak value. For the blue illumination, the peak value is $337\,\text{nm}$, while the red and green LEDs demonstrate peak values of $307\,\text{nm}$ and $301\,\text{nm}$, respectively. As the thickness of the sample is a constant between the different datasets, the OPD difference is likely to be a result of the refractive index of the object, or the surrounding matrix, being wavelength-dependent. Combined with knowledge of the refractive index of the media and exact thickness, this result could be used to quantify how the refractive index of the object depends on wavelength, i.e. (chromatic) dispersion [21], using Equation (2.11). The dispersive behavior of the object could then be determined for a range of wavelengths by fitting a Cauchy equation [21], for example.

The recovered phase distribution may also be used to determine important optical parameters, through the scattering-phase theorem [24]. Knowledge of the scattering parameters for biological tissue can have important applications in both diagnostics and therapeutic techniques [23].

Another important benefit of FP imaging, is that no staining is needed to image transpar-

ent samples. Various staining methods are common ways of achieving amplitude contrast for transparent objects (for example HES-staining, see subsection 4.5.4). The staining level may be uneven or varying between different samples [77], and will thus introduce an extra element of uncertainty to the measurements. Other techniques may be used to image similar samples without staining, e.g. second harmonic generation techniques [78]. However, such techniques require expensive equipment, whereas an FPM may be built from a standard optical microscope using relatively cheap hardware extensions.

5.4 3D imaging

The 3D imaging results are based on experimental data of a sample consisting of two USAF targets placed on top of each other with a separation of $110\,\mu m$, as described in ref. [6]. The term *quasi-3D* will be used to describe the sample, to emphasize that it is not a continuous 3D sample, but rather a stack of two 2D samples.

5.4.1 TW-3D reconstruction

The result of a reconstruction using $N = 2$ and the TW-3D algorithm is shown in Figure 5.12. The raw image, displayed in Figures 5.12a, shows the two stacked targets, while 5.12b and d display the reconstructed slice amplitudes. Most of the out-of-plane blur has been removed, indicating a good numerical separation between the two slices has been achieved. A strongly enhanced lateral resolution is also observed, best seen in the zoomed-in sections in Figures 5.12c and e.
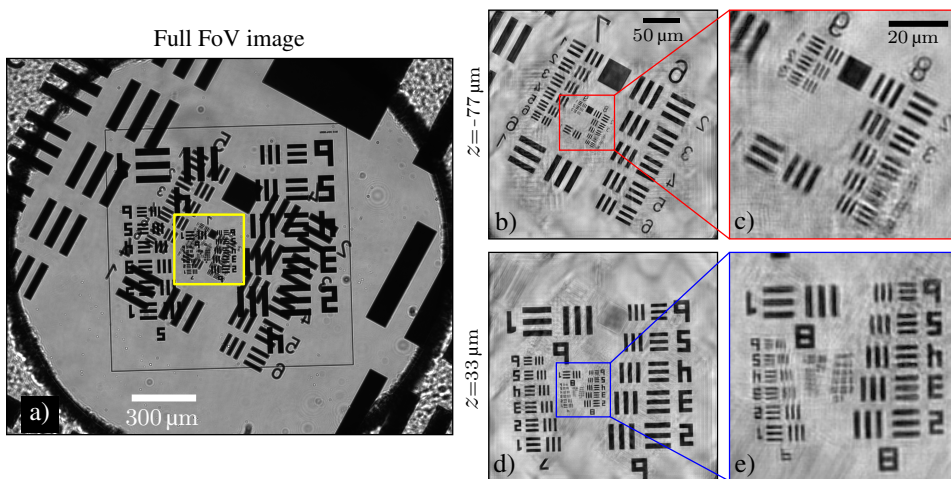
Figure 5.12: TW-3D reconstruction of stacked USAF targets. a) Full FoV raw image with low resolution. The yellow square indicates the region studied in the reconstructions. b) and d) The reconstructed slices at two different depths, $-77\,\mu m$ and 33 um, respectively. c) and e) Magnified selections of the two slices. The scalebars in b) and c) are also valid for d) and e), respectively. Ref. [6] is accredited for the full FoV image.

The results are similar to those presented in the original article, ref. [6], with minor differences. The original figure from ref. [6] is included in Appendix C for reference. A notable difference is that while the finest resolvable feature in Tian and Waller's results was element 4 of group 9, the reconstructions obtained in this work shows resolvable lines even in element 5 of group 9. The achieved full-pitch resolution is thus $1.23\,\mu\text{m}$, compared to $1.38\,\mu\text{m}$ in ref. [6]. The differences may be attributed to different noise correction schemes or different implementations of the algorithms. The authors of ref. [6] do not state the number of iterations performed, so a mismatch between number of iterations is another possible source of the observed difference.

The transversal resolution of 3D FP should be the same as for 2D FP, i.e. given by Equation (3.13). For the $0.41\,NA_{\text{illu}}$, and $0.1\,NA_{\text{obj}}$, the theoretically predicted full-pitch resolution is $1.26\,\mu\text{m}$. This is a slightly larger value than the measured resolution, with a difference of $0.03\,\mu\text{m}$. The close correlation with the expected result indicates that the single scattering approximation in the resolution analysis is appropriate, at least for a low number of slices.

Due to the relatively large spacing between the two slices ($110\,\mu\text{m}$), the derived formula for z-resolution of 3D FP, given by Equation (3.42), is not validated compared to theory in this work, as the expected z-resolution is much less than the slice separation, $\delta z \ll \Delta z$. The results do, however, indicate that δz is at most $110\,\mu\text{m}$.

Going forward, an important area in which better understanding is needed is the convergence requirements for multislice FP. The convergence requirement should incorporate important experimental quantities, such as the DoF, the NA, and volumetric overlap between neighboring illumination angles in the Fourier domain.

5.4.2 Fresnel-3D reconstructions

Evaluating the SSE resulting from multiple reconstructions obtained at different values for z_1 revealed that the value which minimized the error was $z_1 = 40\,\text{mm}$. Subsequent reconstructions using the Fresnel-3D algorithm use this value.

The results of the Fresnel-3D algorithm is displayed in Figure 5.13. The TW-3D reconstruction is also reprinted in the figure, to simplify the direct comparison of the two results. Overall, the resulting slices are similar between the two algorithms. A notable difference is that the Fresnel-3D results, Figure 5.13d–f, display a more even or flat background, compared to the TW-3D results, Figure 5.13a–c. As the gray regions of the slices correspond to glass in the actual sample, a flat background is the expected result, and the Fresnel-3D results may be seen as an improvement wrt. correct background reconstruction.

In terms of resolution, the same number of elements are resolved using both methods, an indication that the Ewald sphere-based resolution analysis is applicable also for the Fresnel imaging model, even though the analysis is based on Fraunhofer imaging and single scattering.

Figures 5.13b and e show the same section of one of the USAF targets, respectively reconstructed with Fresnel-3D and TW-3D. The figures are similar, with a notable difference at the 4th and 5th elements of group 8: while the lines in sub-figure b are severely blurred, they are perfectly resolved in sub-figure e. The blurred elements in the Fraunhofer-based
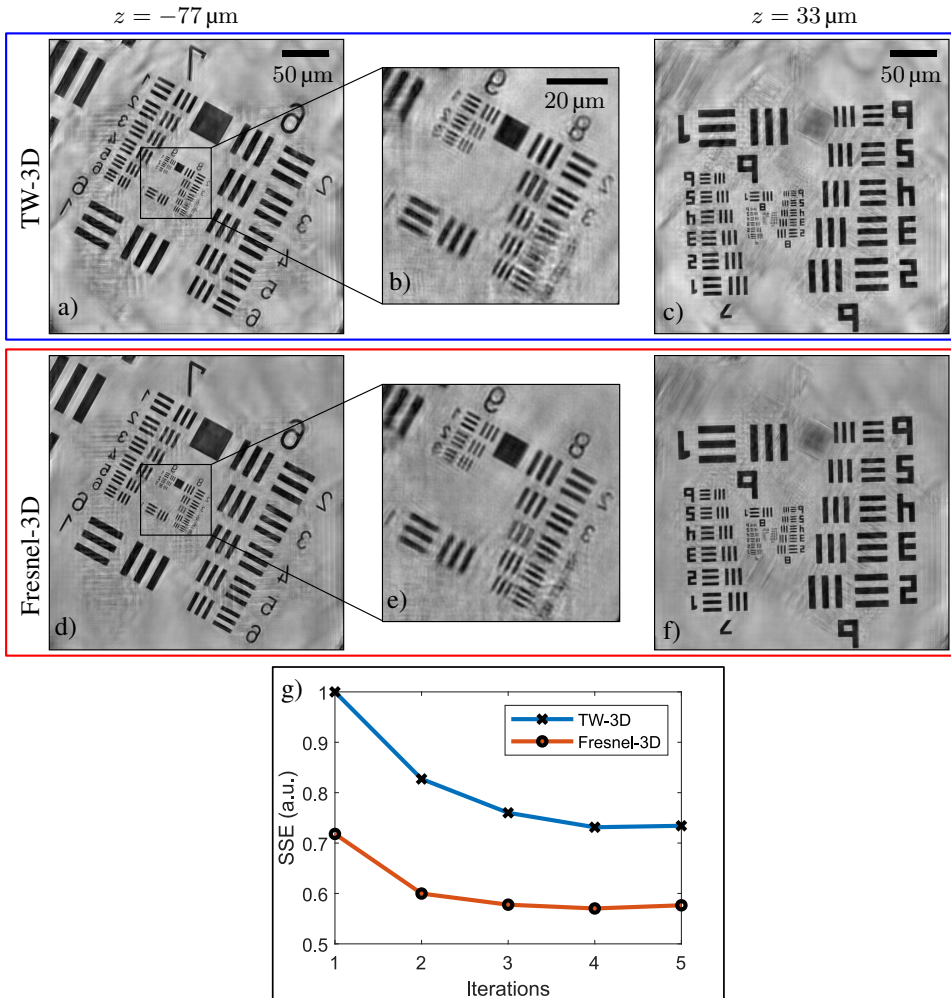
Figure 5.13: Reconstruction using Fresnel-3D compared to TW-3D. a)–c) Reconstructed amplitude using TW-3D. d)–f) Reconstructed amplitude using Frensel-3D. g) Plot of the SSE of the two 3D FP algorithms as a function of number of iterations.

reconstruction in Figure 5.13b also appear blurred in the original results in ref. [6] (cf. Appendix C).

Figure 5.13g displays the SSE, computed using Equation (4.16), as a function of number of iterations. After a single iteration, the error of the Fresnel-3D method is smaller than after five iterations of TW-3D. When both algorithms have reached convergence (after 4 iterations), the error of the Fresnel-3D method is $< 80\,\%$ of the TW-3D error, indicating that the result achieved with the Fresnel-3D algorithms is closer to the ground truth than the TW-3D results. This is expected, as the Fresnel-3D algorithm is based on Fresnel imaging model, and thus makes fewer approximations than the TW-3D algorithm. Especially for a large section area, or far from the optical axis, the Fraunhofer approximation will be too rough.

Note that computing the SSE involves simulating the imaging process. The Fresnel imaging model is applied to simulate imaging of the Fresnel-3D result, while the Fraunhofer model is used for TW-3D. However, similar differences in SSE is also found when the Fraunhofer model is used to simulate imaging of both reconstructions.

5.4.3 Multislice FP compared to other 3D FP techniques

Other 3D imaging techniques based on FP have recently been developed, sharing the advantage of no mechanically moving parts with multislice FP. An example being Fourier ptychographic tomography (FPT) [16], developed by Horstmeyer et al., applying the first Born approximation and a scattering potential to model the interaction between the 3D sample and the illuminating field. The approximation is only valid for weakly scattering samples without multiple scattering events, so the method is not suitable for samples with large absorption or phase shifts [16]. However, in FPT the 3D Fourier space of the sample is updated directly, instead of distributed on a rather arbitrary number of slices.

A more recent method, Fourier ptychographic diffraction tomography (FPDT) (arXiv: [79]), that makes use of the Rytov approximation in place of the first Born approximation, has been demonstrated to achieve better results for thicker samples [79]. However, a small phase gradient and single scattering is still required for the approximation to hold [80, 81]. The notable advantage of the Rytov approximation compared to the Born approximation is that the former does not require the total phase shift through the sample to be small [80], which explains the increased performance of the Rytov approximated FP approach for thicker samples.

The multislice FP model does not assume single or weak scattering; the entire exit field resulting from one slice is treated as the incoming field onto the next slice. However, the model does not include backscattered light, which can be included in the FPT framework [16]. For biological tissue, the mean free path between scattering events is typically $\leq 100\,\mu\text{m}$ [23], indicating that for thicker biological samples, multiple scattering events are likely. For such samples, a multislice algorithm would probably be a better fit than FPT.

Both FPT and FPDT employ the Fraunhofer imaging model; the algorithms are directly coupled to the 3D Fourier domains of the samples. It has been demonstrated in this thesis that the multislice FP approach may be modified to use the Fresnel imaging model, with improved performance. No such modification, to the best of the author's knowledge, has been demonstrated for FPT or FPDT.

Conclusion

A Fourier ptychographic microscope has been demonstrated, capable of resolution enhancement beyond the classical limits of the applied optics, quantitative phase imaging and aberration correction.

Using a 0.055 NA objective to capture the images, the FP reconstruction provided a full-pitch resolution $1.56\,\mu m$, corresponding to a synthetic NA of 0.33. The measured resolution of the FPM was shown to correlate well with the theoretical resolution, until the limit of the resolution target was reached. The improvement in resolution corresponds to an SBP enhancement factor of 9 compared to incoherent imaging and 36 compared to coherent imaging.

Verification of the microscope's QPI capabilities was done by imaging known phase samples: a dedicated phase target and a solution of polymer beads in water, with known refractive index. The reconstructions revealed that the microscope was able to quantitatively determine the phase of the test samples, however with notable errors for low-frequent phase information and steep phase gradients. Low-frequent phase information is not recovered correctly without including the LEDs positioned near the edge of the BF region, but including these illumination angles will also introduce noise artifacts in the reconstruction. Steep phase gradients correspond to high frequencies, and even though the cutoff frequency is increased in the FP procedure, large differences in refractive indices can lead to spatial frequencies beyond the cutoff, and thus failure to correctly recover the phase gradient.

A bone and cartilage sample was imaged and reconstructed, demonstrating the usage of the FPM on a realistic sample, with both large FoV and high resolution.

Three-dimensional FP reconstructions were performed for a quasi-3D sample, consisting of two 2D layers, using an existing multislice-based algorithm, termed TW-3D. The results demonstrated a lateral resolution gain equivalent to that of 2D FP in both planes. The out-of-plane blur was almost completely removed.

The TW-3D algorithm relies on the Fraunhofer imaging model. A modified version of the algorithm, termed Fresnel-3D, was proposed, based on Fresnel imaging theory, where the object space quadratic phase factor is not ignored. Reconstructions performed with Fresnel-3D demonstrated less noisy results, as well as a reduced error, compared to TW-3D.

The SSE of the Fresnel-3D algorithm was smaller after a single iteration than after five iterations of the TW-3D algorithm, indicating that acceptable results can be reached much faster using the new algorithm.

6.1 Further work

The challenge of recovering low-frequent phase information is understood under the assumption of a weak object. However, the simulations presented in this thesis revealed that the same conclusions cannot straightforwardly be made for strong objects. Phase information transfer for a strong object needs to be studied in further detail in order to understand the observed behavior, and possibly break the current trade-off between noisy reconstructions and missing frequency information.

The Fresnel-3D algorithm has been shown to work well for a quasi-3D sample, so the next step would be testing the algorithm on a continuous 3D sample. Doing so would yield valuable results that may determine if the algorithm is useful in practical microscopy applications.

Another possible improvement to the multislice FP method is modifying the updating step to use an adaptive step size optimization algorithm. Adaptive step size methods have been demonstrated for 2D FP [82], with increased robustness to noise.

To increase the axial resolution of 3D FP, an approach of combining FP with tomography may be tried out. A similar combination of ptychography and tomography is proposed in ref. [27], and could serve as a source of inspiration.

Bibliography

[1] G. Zheng, R. Horstmeyer, and C. Yang. "Wide-field, high-resolution Fourier ptychographic microscopy". *Nature Photonics* **7**(9), pp. 739–745 (2013). DOI: 10.1038/nphoton.2013.187.

[2] G. Zheng, C. Kolner, and C. Yang. "Microscopy refocusing and dark-field imaging by using a simple LED array". *Optics Letters* **36**(20), pp. 3987–3989 (2011). DOI: 10.1364/OL.36.003987.

[3] J. M. Rodenburg and H. M. L. Faulkner. "A phase retrieval algorithm for shifting illumination". *Applied Physics Letters* **85**(20), pp. 4795–4797 (2004). DOI: 10.1063/1.1823034.

[4] A. M. Maiden and J. M. Rodenburg. "An improved ptychographical phase retrieval algorithm for diffractive imaging". *Ultramicroscopy* **109**(10), pp. 1256–1262 (2009). DOI: 10.1016/j.ultramic.2009.05.012.

[5] A. M. Maiden, M. J. Humphry, and J. M. Rodenburg. "Ptychographic transmission microscopy in three dimensions using a multi-slice approach". *JOSA A* **29**(8), pp. 1606–1614 (2012). DOI: 10.1364/JOSAA.29.001606.

[6] L. Tian and L. Waller. "3D intensity and phase imaging from light field measurements in an LED array microscope". *Optica* **2**(2), pp. 104–111 (2015). DOI: 10.1364/OPTICA.2.000104.

[7] L. Tian, X. Li, K. Ramchandran, and L. Waller. "Multiplexed coded illumination for Fourier Ptychography with an LED array microscope". *Biomedical Optics Express* **5**(7), pp. 2376–2389 (2014). DOI: 10.1364/BOE.5.002376.

[8] X. Ou, R. Horstmeyer, C. Yang, and G. Zheng. "Quantitative phase imaging via Fourier ptychographic microscopy". *Optics Letters* **38**(22), pp. 4845–4848 (2013). DOI: 10.1364/OL.38.004845.

[9] X. Ou, G. Zheng, and C. Yang. "Embedded pupil function recovery for Fourier ptychographic microscopy". *Optics Express* **22**(5), pp. 4960–4972 (2014). DOI: 10.1364/OE.22.004960.

[10] Z. Bian, S. Dong, and G. Zheng. "Adaptive system correction for robust Fourier ptychographic imaging". *Optics Express* **21**(26), pp. 32400–32410 (2013). DOI: 10.1364/OE.21.032400.

[11] J. Sun, C. Zuo, J. Zhang, Y. Fan, and Q. Chen. "High-speed Fourier ptychographic microscopy based on programmable annular illuminations". *Scientific Reports* **8**(1), p. 7669 (2018). DOI: 10.1038/s41598-018-25797-8.

[12] L. Tian, Z. Liu, L.-H. Yeh, M. Chen, J. Zhong, and L. Waller. "Computational illumination for high-speed in vitro Fourier ptychographic microscopy". *Optica* **2**(10), pp. 904–911 (2015). DOI: 10.1364/OPTICA.2.000904.

[13] J. Sun, Q. Chen, J. Zhang, Y. Fan, and C. Zuo. "Single-shot quantitative phase microscopy based on color-multiplexed Fourier ptychography". *Optics Letters* **43**(14), pp. 3365–3368 (2018). DOI: 10.1364/OL.43.003365.

[14] S. Dong, P. Nanda, R. Shiradkar, K. Guo, and G. Zheng. "High-resolution fluorescence imaging via pattern-illuminated Fourier ptychography". *Optics Express* **22**(17), pp. 20856–20870 (2014). DOI: 10.1364/OE.22.020856.

[15] P. Li, D. J. Batey, T. B. Edo, and J. M. Rodenburg. "Separation of three-dimensional scattering effects in tilt-series Fourier ptychography". *Ultramicroscopy* **158**, pp. 1–7 (2015). DOI: 10.1016/j.ultramic.2015.06.010.

[16] R. Horstmeyer, J. Chung, X. Ou, G. Zheng, and C. Yang. "Diffraction tomography with Fourier ptychography". *Optica* **3**(8), pp. 827–835 (2016). DOI: 10.1364/OPTICA.3.000827.

[17] J. W. Goodman. *Introduction to Fourier Optics*. 4th ed. New York, NY, USA: W. H. Freeman (2017). ISBN: 1-319-11916-6.

[18] N. Farahani, A. V. Parwani, and L. Pantanowitz. "Whole slide imaging in pathology: advantages, limitations, and emerging perspectives". *Pathology and Laboratory Medicine International* **7** (2015). DOI: 10.2147/PLMI.S59826.

[19] R. Horstmeyer, X. Ou, G. Zheng, P. Willems, and C. Yang. "Digital pathology with Fourier ptychography". *Computerized Medical Imaging and Graphics*. Breakthrough Technologies In Digital Pathology **42**, pp. 38–43 (2015). DOI: 10.1016/j.compmedimag.2014.11.005.

[20] V. C. Abraham, D. L. Taylor, and J. R. Haskins. "High content screening applied to large-scale cell biology". *Trends in Biotechnology* **22**(1), pp. 15–22 (2004). DOI: 10.1016/j.tibtech.2003.10.012.

[21] E. Hecht. *Optics*. 5th ed. Essex, England: Pearson Education Limited (2017). ISBN: 978-1-292-09693-3.

[22] Z. Wang, L. Millet, M. Mir, H. Ding, S. Unarunotai, J. Rogers, M. U. Gillette, and G. Popescu. "Spatial light interference microscopy (SLIM)". *Optics Express* **19**(2), pp. 1016–1026 (2011). DOI: 10.1364/OE.19.001016.

[23] S. L. Jacques. "Optical properties of biological tissues: a review". *Physics in Medicine and Biology* **58**(11), R37–R61 (2013). DOI: 10.1088/0031-9155/58/11/R37.

[24] Z. Wang, H. Ding, and G. Popescu. "Scattering-phase theorem". *Optics Letters* **36**(7), pp. 1215–1217 (2011). DOI: 10.1364/OL.36.001215.

[25] P. Thibault, M. Dierolf, A. Menzel, O. Bunk, C. David, and F. Pfeiffer. "High-Resolution Scanning X-ray Diffraction Microscopy". *Science* **321**(5887), pp. 379–382 (2008). DOI: 10.1126/science.1158573.

[26] K. Lee, H.-D. Kim, K. Kim, Y. Kim, T. R. Hillman, B. Min, and Y. Park. "Synthetic Fourier transform light scattering". *Optics Express* **21**(19), pp. 22453–22463 (2013). DOI: 10.1364/OE.21.022453.

[27] P. Li and A. Maiden. "Multi-slice ptychographic tomography". *Scientific Reports* **8**(1), p. 2049 (2018). DOI: 10.1038/s41598-018-20530-x.

[28] S. Kawata, O. Nakamura, and S. Minami. "Optical microscope tomography. I. Support constraint". *JOSA A* **4**(1), pp. 292–297 (1987). DOI: 10.1364/JOSAA.4.000292.

[29] A. M. Larson. "Multiphoton microscopy". *Nature Photonics* **5**, p. 1 (2010). DOI: 10.1038/nphoton.an.2010.2.

[30] C. J. Engelbrecht and E. H. Stelzer. "Resolution enhancement in a light-sheet-based microscope (SPIM)". *Optics Letters* **31**(10), pp. 1477–1479 (2006). DOI: 10.1364/OL.31.001477.

[31] D. B. Murphy and M. W. Davidson. "Confocal Laser Scanning Microscopy". In: *Fundamentals of Light Microscopy and Electronic Imaging*. 2nd ed. Hoboken, NJ, USA: John Wiley & Sons (2012), pp. 265–305. ISBN: 978-1-118-38290-5.

[32] T. M. Godden, R. Suman, M. J. Humphry, J. M. Rodenburg, and A. M. Maiden. "Ptychographic microscope for three-dimensional imaging". *Optics Express* **22**(10), pp. 12513–12523 (2014). DOI: 10.1364/OE.22.012513.

[33] Inkscape Project. *Inkscape*. Version 0.92 (2017). URL: https://inkscape.org.

[34] C. A. Schneider, W. S. Rasband, and K. W. Eliceiri. "NIH Image to ImageJ: 25 years of image analysis". *Nature Methods* **9**, pp. 671–675 (2012). DOI: 10.1038/nmeth.2089.

[35] The MathWorks, Inc. *MATLAB Release 2018a*. Natick, Massachusetts, USA.

[36] E. Kreyszig. *Advanced Engineering Mathematics*. 9th ed. Hoboken, NJ, USA: John Wiley & Sons, Inc. (2006). ISBN: 978-0-471-72897-9.

[37] D. Voelz. *Computational Fourier Optics: A MATLAB Tutorial*. 1st ed. Bellingham, WA, USA: SPIE (2011). ISBN: 978-0-8194-8204-4.

[38] K. Rottmann. *Matematisk Formelsamling*. Norwegian translation. Original title: Mathematische Formelsammlung. Oslo, Norway: Spektrum forlag (2003). ISBN: 978-82-7822-005-4.

[39] J. W. Goodman. *Statistical Optics*. 2nd ed. Hoboken, NJ, USA: John Wiley & Sons, Inc. (2015). ISBN: 978-1-119-00946-7.

[40] Z. Huang. "Brightness and coherence of synchrotron radiation and FELs". In: International Particle Accelerator Conference. Shanghai, China: SLAC National Accelerator Laboratory (2013).

[41] M. Born and E. Wolf. *Principles of Optics: Eletromagnetic Theory of Propagation, Interference and Diffraction of Light*. 6th ed. Oxford, England: Pergamon Press (1980). ISBN: 0-08-026482-4.

[42] J. M. Cowley. *Diffraction Physics*. Amsterdam, Netherlands: North-Holland Publishing Company (1975). ISBN: 0-7204-0311-1.

[43] K. Li, M. Wojcik, and C. Jacobsen. "Multislice does it all; calculating the performance of nanofocusing X-ray optics". *Optics Express* **25**(3), pp. 1831–1846 (2017). DOI: 10.1364/OE.25.001831.

[44] P. C. Konda. "Multi-Aperture Fourier Ptychographic Microscopy: development of a high-speed gigapixel coherent computational microscope". PhD thesis. University of Glasgow (2018).

[45] B. E. A. Saleh and M. C. Teich. *Fundamentals of Photonics*. 2nd ed. Hoboken, NJ, USA: John Wiley & Sons, Inc. (2007). ISBN: 978-0-471-35832-9.

[46] R. J. Noll. "Zernike polynomials and atmospheric turbulence". *JOSA* **66**(3), pp. 207–211 (1976). DOI: 10.1364/JOSA.66.000207.

[47] R. Horstmeyer, R. Heintzmann, G. Popescu, L. Waller, and C. Yang. "Standardizing the resolution claims for coherent microscopy". *Nature Photonics* **10**, pp. 68–71 (2016). DOI: 10.1038/nphoton.2015.279.

[48] D. Claus, D. Iliescu, and P. Bryanston-Cross. "Quantitative space-bandwidth product analysis in digital holography". *Applied Optics* **50**(34), H116–H127 (2011). DOI: 10.1364/AO.50.00H116.

[49] A. W. Lohmann, R. G. Dorsch, D. Mendlovic, Z. Zalevsky, and C. Ferreira. "Space–bandwi dth product of optical signals and systems". *JOSA A* **13**(3), pp. 470–473 (1996). DOI: 10.1364/JOSAA.13.000470.

[50] G. Zheng. *Fourier Ptychographic Imaging: A MATLAB Tutorial*. 2054-7307. San Rafael, CA, USA: Morgan & Claypool Publishers (2016). ISBN: 978-1-68174-272-4.

[51] M. A. Neifeld. "Information, resolution, and space–bandwidth product". *Optics Letters* **23**(18), pp. 1477–1479 (1998). DOI: 10.1364/OL.23.001477.

[52] X. Ou. "Computational Microscopy: Breaking the Limit of Conventional Optics". PhD thesis. California Institute of Technology (2016). DOI: 10.7907/Z9M32SRZ.

[53] J. Sun, C. Zuo, L. Zhang, and Q. Chen. "Resolution-enhanced Fourier ptychographic microscopy based on high-numerical-aperture illuminations". *Scientific Reports* **7**(1), p. 1187 (2017). DOI: 10.1038/s41598-017-01346-7.

[54] E. H. R. Tsai, I. Usov, A. Diaz, A. Menzel, and M. Guizar-Sicairos. "X-ray ptychography with extended depth of field". *Optics Express* **24**(25), pp. 29089–29108 (2016). DOI: 10.1364/OE.24.029089.

[55] X. Ou, R. Horstmeyer, G. Zheng, and C. Yang. "High numerical aperture Fourier ptychography: principle, implementation and characterization". *Optics Express* **23**(3), pp. 3472–3491 (2015). DOI: 10.1364/OE.23.003472.

[56] C. Kittel. *Introduction to Solid State Physics*. 8th ed. Hoboken, NJ, USA: John Wiley & Sons, Inc. (2005). ISBN: 978-0-471-41526-8.

[57] N. Streibl. "Three-dimensional imaging by a microscope". *Journal of the Optical Society of America A* **2**(2), pp. 121–127 (1985).

[58] S. Dong, Z. Bian, R. Shiradkar, and G. Zheng. "Sparsely sampled Fourier ptychography". *Optics Express* **22**(5), pp. 5455–5464 (2014). DOI: 10.1364/OE.22.005455.

[59] T. Kringeland. "Developing Methods and Tools for Three-Dimensional Computational Reconstructions in X-ray and Visible Light Microscopy". Master's thesis. NTNU (2015).

[60] Arduino. *Arduino Due* (2018). URL: https://store.arduino.cc/arduino-due (visited on Dec. 3, 2018).

[61] Edmund Optics Inc. *EO Infinity Corrected Long Working Distance Objectives* (2018). URL: https://www.edmundoptics.com/f/eo_infty_lwd/13506/ (visited on Dec. 4, 2018).

[62] IDS Imaging Development Systems. *UI-3480CP Rev. 2* (2018). URL: https://en.ids-imaging.com/store/ui-3480cp-rev-2.html (visited on Dec. 6, 2018).

[63] Newport Corporation. *UTS Mid-Range Travel Steel Linear Stage, 50 mm Travel, Stepper Motor* (2018). URL: https://www.newport.com/p/UTS50PP (visited on Dec. 4, 2018).

[64] Y. Zhang, A. Pan, M. Lei, and B. Yao. "Data preprocessing methods for robust Fourier ptychographic microscopy". *Optical Engineering* **56**(12), p. 123107 (2017). DOI: 10.1117/1.OE.56.12.123107.

[65] L. Hou, H. Wang, J. Wang, and M. Xu. "Background-noise Reduction for Fourier Ptychographic Microscopy Based on an Improved Thresholding Method". *Current Optics and Photonics* **2**(2), p. 7 (2018).

[66] D. G. Voelz and M. C. Roggemann. "Digital simulation of scalar optical diffraction: revisiting chirp function sampling criteria and consequences". *Applied Optics* **48**(32), pp. 6132–6142 (2009). DOI: 10.1364/AO.48.006132.

[67] Edmund Optics Inc. *2" x 2" Positive, 1951 USAF Hi-Resolution Target* (2018). URL: https://www.edmundoptics.com/p/2-x-2-positive-1951-usaf-hi-resolution-target/15108/ (visited on Dec. 6, 2018).

[68] Edmund Optics Inc. *1951 USAF Resolution Calculator* (2018). URL: https://www.edmundoptics.com/resources/tech-tools/1951-usaf-resolution/ (visited on Dec. 19, 2018).

[69] T. M. Godden, A. Muñiz-Piniella, J. D. Claverley, A. Yacoot, and M. J. Humphry. "Phase calibration target for quantitative phase imaging with ptychography". *Optics Express* **24**(7), pp. 7679–7692 (2016). DOI: 10.1364/OE.24.007679.

[70] Phase Focus Ltd. *Quantitative Phase Imaging of the Phasefocus Phase Calibration Target* (2019). URL: https://www.phasefocus.com/resources/tech-notes/quantitative-phase-imaging-phasefocus-phase-calibration-target (visited on May 16, 2019).

[71] I. H. Malitson. "Interspecimen Comparison of the Refractive Index of Fused Silica". *JOSA* **55**(10), pp. 1205–1209 (1965). DOI: 10.1364/JOSA.55.001205.

[72] Beckman Coulter, Inc. *Flow-Check Fluorospheres* (2019). URL: https://www.beckman.com/reagents/coulter-flow-cytometry/antibodies-and-kits/clinical-research-systems-and-kits/6605359 (visited on June 7, 2019).

[73] N. G. Sultanova, S. N. Kasarova, and I. D. Nikolov. "Characterization of optical properties of optical polymers". *Optical and Quantum Electronics* **45**(3), pp. 221–232 (2013). DOI: 10.1007/s11082-012-9616-6.

[74] G. M. Hale and M. R. Querry. "Optical Constants of Water in the 200-nm to 200-μm Wavelength Region". *Applied Optics* **12**(3), pp. 555–563 (1973). DOI: 10.1364/AO.12.000555.

[75] I. R. Hellings, N. I. Dolvik, S. Ekman, and K. Olstad. "Cartilage canals in the distal intermediate ridge of the tibia of fetuses and foals are surrounded by different types of collagen". *Journal of Anatomy* **231**(4), pp. 615–625 (2017). DOI: 10.1111/joa.12650.

[76] K. Guo, S. Dong, P. Nanda, and G. Zheng. "Optimization of sampling pattern and the design of Fourier ptychographic illuminator". *Optics Express* **23**(5), pp. 6171–6180 (2015). DOI: 10.1364/OE.23.006171.

[77] S. Uttam, R. K. Bista, Y. Liu, D. J. Hartman, and R. E. Brand. "Correction of stain variations in nuclear refractive index of clinical histology specimens". *Journal of Biomedical Optics* **16**(11), p. 116013 (2011). DOI: 10.1117/1.3650306.

[78] A. Finnøy, K. Olstad, and M. B. Lilledahl. "Non-linear optical microscopy of cartilage canals in the distal femur of young pigs may reveal the cause of articular osteochondrosis". *BMC Veterinary Research* **13**(1), p. 270 (2017). DOI: 10.1186/s12917-017-1197-y.

[79] C. Zuo, J. Sun, J. Li, A. Asundi, and Q. Chen. "Wide-field high-resolution 3D microscopy with Fourier ptychographic diffraction tomography". *arXiv [physics.optics]* (2019). arXiv: 1904.09386v2.

[80] A. J. Devaney. "Inverse-scattering theory within the Rytov approximation". *Optics Letters* **6**(8), pp. 374–376 (1981). DOI: 10.1364/OL.6.000374.

[81] D. Jin, R. Zhou, Z. Yaqoob, and P. T. C. So. "Tomographic phase microscopy: principles and applications in bioimaging [Invited]". *JOSA B* **34**(5), B64–B77 (2017). DOI: 10.1364/JOSAB.34.000B64.

[82] C. Zuo, J. Sun, and Q. Chen. "Adaptive step-size strategy for noise-robust Fourier ptychographic microscopy". *Optics Express* **24**(18), pp. 20724–20744 (2016). DOI: 10.1364/OE.24.020724.

[83] J. R. Fienup. "Phase retrieval algorithms: a comparison". *Applied Optics* **21**(15), pp. 2758–2769 (1982). DOI: 10.1364/AO.21.002758.

[84] M. Guizar-Sicairos and J. R. Fienup. "Phase retrieval with transverse translation diversity: a nonlinear optimization approach". *Optics Express* **16**(10), pp. 7264–7278 (2008). DOI: 10.1364/OE.16.007264.

[85] A. Tripathi, I. McNulty, and O. G. Shpyrko. "Ptychographic overlap constraint errors and the limits of their numerical recovery using conjugate gradient descent methods". *Optics Express* **22**(2), pp. 1452–1466 (2014). DOI: 10.1364/OE.22.001452.

[86] G. B. Arfken, H.-J. Weber, and F. E. Harris. *Mathematical Methods for Physicists: A Comprehensive Guide*. Academic Press (2012). ISBN: 978-0-12-384655-6.

Appendix A

Conference paper

A conference paper was written and submitted to the Imaging and Applied Optics Congress (June 24 – June 27, 2019), hosted by the Optical Society (OSA). The conference paper submission was titled "Fresnel Imaging Model for Improved Multislice Fourier Ptychography", and describes the Fresnel-3D algorithm and the obtained results.

The conference paper is attached in the following pages. Requirements for submission were a short abstract (< 35 words) and maximum two pages, hence the short format.

Fresnel Imaging Model for Improved Multislice Fourier Ptychography

Knut Olav Schnell[1], Mojde Hasanzade[2],
Muhammad Nadeem Akram[2], and Dag Werner Breiby[1,2*]

[1]*PoreLab, Department of Physics, Norwegian University of Science and Technology, Trondheim, Norway*
[2]*Department of Microsystems, University of South-Eastern Norway, Borre, Norway*

Author e-mail address: dag.breiby@ntnu.no

Abstract: Multislice Fourier ptychography (MFP) uses angularly diverse illumination to compute a three-dimensional image of the sample. We present an improved MFP algorithm, demonstrating better convergence properties and reduced noise in reconstructions. © 2019 The Author(s)

1. Introduction

Fourier ptychography (FP) is a recently developed computational imaging technique, using a dataset of multiple low-resolution images obtained under different illumination angles to recover one single high-resolution, wide field of view (FoV) image containing both amplitude and quantitative phase information [1]. A conventional microscope may be modified to an FP platform by replacing the illumination unit with a LED matrix [1, 2]. The concept of FP can been extended to 3D imaging by using a multislice approach to model light transmission through a 3D sample [2, 3]. Compared to other 3D imaging techniques, multislice FP (MFP) has the advantage of no moving parts, removing the uncertainty and time delay introduced by motors and actuators, allowing high-speed 3D imaging.

In a multislice model of a 3D sample, the sample is divided into a set of thin slices, each of which are sufficiently thin for the interaction with the incoming wave field to be treated as multiplicative [4]. To transfer the exit field of one slice to the input plane of the next slice, a propagation scheme is employed [4]. The imaging operation is modeled as a low-pass filter with cutoff frequency determined by the numerical aperture (NA) of the objective, including aberrations. Using the collected images as intensity constraints, MFP proceeds to iteratively update each of the slices of the 3D object, using a steepest-gradient based optimization procedure [2, 3].
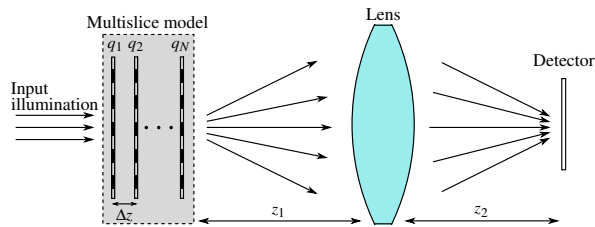

Fig. 1. Illustration of the imaging model. q_n denotes the complex slices of the multislice model, and Δz is the distance between slices. The sketch is not to scale.

Image formation may be expressed as a superposition integral, where the point-spread function h expresses the relationship between the input field and the image [5]. Using Fresnel propagation and a single lens model of the imaging system, h can be expressed as [5]

$$h(x,y;\xi,\eta) = \exp\left[i\frac{k}{2z_2}(x^2+y^2)\right]\exp\left[i\frac{k}{2z_1}(\xi^2+\eta^2)\right]\widehat{h}(x-M\xi,y-M\eta) \qquad (1)$$

where (x,y) and (ξ,η) are the image, and object plane coordinates, respectively. z_1 and z_2 are defined in Fig. 1, and $M = -z_2/z_1$ denotes the magnification. k is the angular wave number of the illumination and $\widehat{h}$ is the Fraunhofer diffraction pattern of the lens pupil, multiplied with a constant factor. The lens law is assumed to be fulfilled, which is the condition for imaging [5]. Assuming the quantity of interest is the image-plane intensity, the first quadratic phase factor (QPF) in eq. (1) may be ignored.

Commonly, the object space QPF in (1) is also ignored in the point-spread function [1–3], which is equivalent to using the Fraunhofer approximation to propagate the exit field of the sample to the lens, and the resulting imaging formalism is thus termed *Fraunhofer imaging*. Here, we propose the usage of the *Fresnel imaging* formalism to model the imaging process in MFP, i.e. keeping the object space QPF, thus retaining the Fresnel approximation.

2. Methods and Results

An open source dataset (see ref. [2]) was used to determine the performance of the Fresnel imaging formalism for MFP. The datasets consist of 293 images, each corresponding to a unique illumination angle, collected with illumination of wavelength $\lambda = 643$ nm and a 4X/0.1 NA objective [2]. The sample being imaged consists of two stacked resolution targets, separated by a distance of 110 μm.

The MFP algorithm described in ref. [2], henceforth termed *Fraunhofer MFP*, was used as a basis for the *Fresnel MFP* algorithm, the difference being the propagation model, as described above. Five iterations of the algorithms were carried out. The z_1 parameter, which is required for the Fresnel MFP algorithm but not given in ref. [2], was determined to be $z_1 = 40$ mm by selecting the value that minimized the sum of squared errors (SSE) between simulated images and actual measurements.
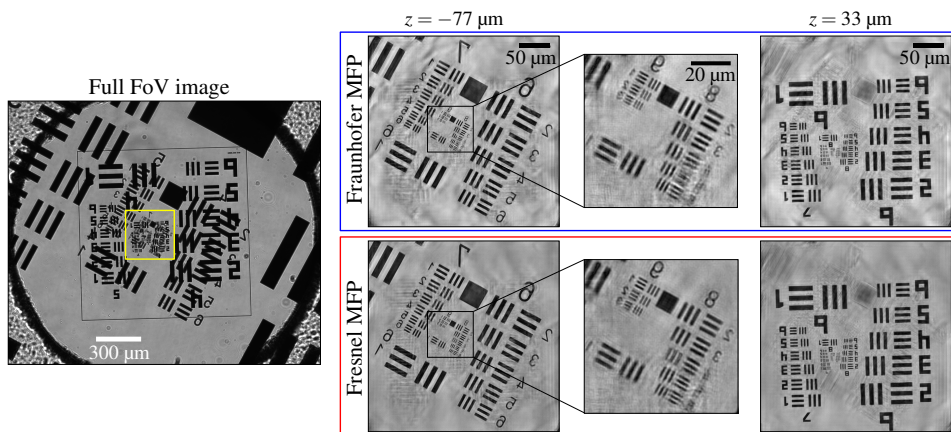

Fig. 2. (Left) Full FoV image of the stacked targets. The yellow square indicates the region studied in the reconstructions. (Right) Reconstructed slices using both Fraunhofer and Fresnel MFP algorithms. Ref. [2] is accredited for the full FoV image and the dataset used to perform the reconstructions.

The obtained results are displayed in Fig. 2. Both MFP algorithms are able to achieve a resolution far beyond the cutoff frequency of the objective in both planes, in line with the theoretically expected results. Both algorithms also remove most of the out-of-plane blur. The Fresnel MFP reconstructions display a reduction in the background noise level, compared to the Fraunhofer MFP results. In addition, the SSE for the Fresnel MFP result is $< 80\,\%$ of the SSE for the Fraunhofer result. A single iteration of Fresnel MFP demonstrates lower SSE than five Fraunhofer MFP iterations. It is also observed that the lines in element 4 and 5 of group 8 in the zoom-in of Fig. 2 are nicely recovered with the Fresnel MFP algorithm, while they appear blurry in the Fraunhofer MFP reconstruction.

Based on these observation, our conclusion regarding the performance of the Fresnel imaging model for MFP, is that by avoiding the questionable approximation of ignoring the object space QPF in (1), the results obtained with MFP show enhanced convergence properties and less noisy reconstructions.

References

1. G. Zheng, R. Horstmeyer, and C. Yang, "Wide-field, high-resolution Fourier ptychographic microscopy," Nat. Photonics **7**, 739–745 (2013).
2. L. Tian and L. Waller, "3D intensity and phase imaging from light field measurements in an LED array microscope," Optica **2**, 104–111 (2015).
3. P. Li, D. J. Batey, T. B. Edo, and J. M. Rodenburg, "Separation of three-dimensional scattering effects in tilt-series Fourier ptychography," Ultramicroscopy **158**, 1–7 (2015).
4. J. M. Cowley, *Diffraction physics* (North-Holland Publishing Company, 1975), Chap. 11.
5. J. W. Goodman, *Introduction to Fourier Optics* 4th ed. (W. H. Freeman, 2017), Chap. 6.

Appendix B

The gradient descent procedure

The gradient descent procedure, also known as steepest-descent, is a computational optimization method, relying on trying to minimize some error metric [83], E. For a given set of parameters, the gradient of the error metric is computed, and the parameters are changed in a direction opposite of the gradient [83]. The process is repeated until a minimum is reached.

In phase retrieval algorithms, it is common that the error metric is related to the functions to be updated by a Fourier transform [83, 84], and that will therefore be the basis of the derivation performed here. The following derivation is based on a similar derivation in ref. [83]. Assuming a standard FP setup, with angularly diverse illumination, intensity measurements $\{I^{(m)}\}$, and Fourier spectra of $\{C^{(m)}\}$, such that $I^{(m)} = \left| \mathcal{F}^{-1}\{C\} \right|^2$, a least square error metric for a the mth illumination angle is

$$E(C^{(m)}) = \int\!\!\!\int\limits_{-\infty}^{\infty} \left[\left| U_o^{(m)}(x,y) \right| - \sqrt{I^{(m)}(x,y)} \right]^2 \mathrm{d}x\,\mathrm{d}y\,, \tag{B.1}$$

where $U_o^{(m)}(x,y) = \mathcal{F}^{-1}\left\{ C^{(m)}(f_x, f_y) \right\}$, (x,y) are detector plane coordinates and (f_x, f_y) are the corresponding linear frequency coordinates. A similar discrete formulation of the same error measure may also be used. For ease of notation, the superscript $^{(m)}$ as well as the subscript $_o$ will be dropped onwards in the derivation.

B.1 Computation of the complex gradient

The next step of the gradient descent procedure is computing the complex gradient of E with respect to C, $\nabla_C E$, as [84],

$$\nabla_C E(C) = \left[\frac{\partial}{\partial C_R(f_x, f_y)} + i \frac{\partial}{\partial C_I(f_x, f_y)} \right] E(C), \tag{B.2}$$

where $C = C_R + iC_I$, i.e. C_R and C_I denote the real and imaginary parts of C, respectively. First computing the real part of the gradient yields

$$\frac{\partial E}{\partial C_R(f_x, f_y)} = 2 \iint\limits_{-\infty}^{\infty} \left[|U(x,y)| - \sqrt{I(x,y)} \right] \frac{\partial |U(x,y)|}{\partial C_R(f_x, f_y)} \, \mathrm{d}x \, \mathrm{d}y \,, \qquad \text{(B.3)}$$

where the chain rule has been used to remove the squaring operation. The partial derivative can be found using the trick [83]

$$\frac{\partial |U(x,y)|}{\partial C_R(f_x, f_y)} = \frac{\partial \{ [|U(x,y)|^2]^{1/2} \}}{\partial C_R(f_x, f_y)} = \frac{\frac{\partial U(x,y)}{\partial C_R(f_x, f_y)} U^*(x,y) + \frac{\partial U^*(x,y)}{\partial C_R(f_x, f_y)} U(x,y)}{2|U(x,y)|},$$
$$\text{(B.4)}$$

where $|U|^2 = U^*U$ and the product rule of differentiation has been used, and * denotes the complex conjugate.

The remaining unsolved term of (B.3) is the derivative of an inverse Fourier transform with respect to the function being transformed, or

$$\frac{\partial U(x,y)}{\partial C_R(f_x, f_y)} = \frac{\partial \mathcal{F}^{-1} \{C\}(x,y)}{\partial C_R(f_x, f_y)}. \qquad \text{(B.5)}$$

Inserting the definition of the inverse Fourier transform the equation becomes

$$\frac{\partial \mathcal{F}^{-1} \{C\}(x,y)}{\partial C_R(f_x, f_y)} = \frac{\partial}{\partial C_R(f_x, f_y)} \iint\limits_{-\infty}^{\infty} C(f_\xi, f_\eta) \exp[2\pi i (f_\xi x + f_\eta y)] \, \mathrm{d}f_\xi \, \mathrm{d}f_\eta \,, \quad \text{(B.6)}$$

where (f_ξ, f_η) are integration variables in the frequency domain. Switching the order of integration and derivation, and using

$$\frac{\partial C(f_\xi, f_\eta)}{\partial C_R(f_x, f_y)} = \frac{\partial}{\partial C_R(f_x, f_y)} \left[C_R(f_\xi, f_\eta) + i C_I(f_\xi, f_\eta) \right] = \delta(f_\xi - f_x, f_\eta - f_y), \quad \text{(B.7)}$$

where δ represents the Dirac delta function, the differentiated inverse Fourier transform may finally be expressed as

$$\frac{\partial U(x,y)}{\partial C_R(f_x, f_y)} = \mathcal{F}^{-1} \{ \delta(f_\xi - f_x, f_\eta - f_y) \}(x,y) = \exp[2\pi i (f_x x + f_y y)], \qquad \text{(B.8)}$$

where the integral property of the δ function, $\int_{-\infty}^{+\infty} \delta(x - a) f(x) dx = f(a)$, has been used. Similarly, the derivative of the conjugate U^* can be shown to be the conjugate of the derivative stated in Equation (B.8).

Inserting Equations (B.8) and (B.4) into the gradient expression (Equation (B.3)) leads to

$$\frac{\partial E}{\partial C_R(f_x, f_y)} =$$

$$\iint\limits_{-\infty}^{\infty} \left[U(x,y) - \sqrt{I(x,y)} \frac{U(x,y)}{|U(x,y)|} \right] \exp[-2\pi i (f_x x + f_y y)] \, \mathrm{d}x \, \mathrm{d}y \, +$$

$$\iint\limits_{-\infty}^{\infty} \left[U^*(x,y) - \sqrt{I(x,y)} \frac{U^*(x,y)}{|U(x,y)|} \right] \exp[2\pi i (f_x x + f_y y)] \, \mathrm{d}x \, \mathrm{d}y \,. \quad \text{(B.9)}$$

Recognizing the integrals in Equation (B.9) as Fourier and inverse Fourier transforms, as well as $\widehat{U} = \sqrt{I}\, U/|U|$ per Equation (3.26), this simplifies to

$$\frac{\partial E}{\partial C_R(f_x, f_y)} = \mathcal{F}\left\{U(x,y) - \widehat{U}(x,y)\right\} + \mathcal{F}^{-1}\left\{U^*(x,y) - \widehat{U}^*(x,y)\right\}. \quad \text{(B.10)}$$

The same method may be applied for the imaginary part of the gradient. The main difference being the derivative of C. Now,

$$\frac{\partial C(f_\xi, f_\eta)}{\partial C_I(f_x, f_y)} = i\delta(f_x, f_y), \quad \text{(B.11)}$$

and the derivative of the conjugate is

$$\frac{\partial C^*(f_\xi, f_\eta)}{\partial C_I(f_x, f_y)} = -i\delta(f_x, f_y). \quad \text{(B.12)}$$

Following the same approach as for the real part of the gradient, one arrives at

$$\frac{\partial E}{\partial C_I(f_x, f_y)} = -i\mathcal{F}\left\{U(x,y) - \widehat{U}(x,y)\right\} + i\mathcal{F}^{-1}\left\{U^*(x,y) - \widehat{U}^*(x,y)\right\}, \quad \text{(B.13)}$$

Inserting Equations (B.13) and (B.10) into the definition of the complex gradient, Equation (B.2), the inverse Fourier transform components cancel out, arriving at

$$\nabla_C E(C) = 2[C(f_x, f_y) - \widehat{C}(f_x, f_y)]. \quad \text{(B.14)}$$

B.2   Gradient step

To minimize the error specified by the error metric, E, a step is taken in the opposite direction of the gradient, $-\nabla_C E$. The step can be expressed as

$$C_{k+1}(f_x, f_y) = C_k(f_x, f_y) + \beta(f_x, f_y)[\widehat{C}_k(f_x, f_y) - C_k(f_x, f_y)] \quad \text{(B.15)}$$

where k indicates the step number and β the step size.

Comparing the step derived from a gradient descent approach, described by Equation (B.15), with the updating function presented in this theses (see Equation (3.22)) reveals notable similarities. Using that $C = G\mathcal{P}$, assuming no defocus term, the updating step is

$$G_{k+1} = \mathcal{U}\left(G_k, \mathcal{P}, C_k, \widehat{C}_k\right) = G_k + \frac{|\mathcal{P}|\,\mathcal{P}^*(\widehat{C}_k - C_k)}{|\mathcal{P}|_{\max}(|\mathcal{P}|^2 + \delta)}. \quad \text{(B.16)}$$

Multiplying Equation (B.16) with $\mathcal{P}$ results in

$$C_{k+1} = C_k + \frac{|\mathcal{P}|}{|\mathcal{P}|_{\max}} \frac{|\mathcal{P}|^2}{|\mathcal{P}|^2 + \delta}(\widehat{C}_k - C_k), \quad \text{(B.17)}$$

where it has been assumed that $G_{k+1}\mathcal{P}$ is equal to C_{k+1}. δ is a regularization constant, usually chosen as a small value [84], such that $|\mathcal{P}|^2\big/(|\mathcal{P}|^2 + \delta) \approx 1$. Then, one can realize that Equation (B.17) is equal to Equation (B.15) with a variable step size defined by

$$\beta(f_x, f_y) = \frac{|\mathcal{P}(f_x, f_y)|}{|\mathcal{P}(f_x, f_y)|_{\max}},\tag{B.18}$$

and an equivalent result, with the roles of $\mathcal{P}$ and G reversed, may be found for the updating step for $\mathcal{P}$. Note that similar step sizes are commonly used [3, 7].

B.3 Analysis of the updating step

It is evident from the derivations in this appendix that the updating step presented in subsection 3.2.2 is closely related to a gradient descent optimization method, given that the direction of the updating step is equal to the direction of the steepest descent of the error metric. However, gradient descent approaches can result in a local minima of the error function, instead of a global minima [85].

One may also note that the derivation of the updating step is performed only for an error metric defined in the Fourier space of the functions being updated, which is not the case for all the uses of $\mathcal{U}(\cdot)$, as it is also used for updating the slices of the multislice object being imaged. However, the error metric may be rewritten as [83]

$$\begin{aligned}E(C^{(m)}) &= \iint\limits_{-\infty}^{\infty} \left|U(x,y) - \widehat{U}(x,y)\right|^2 \mathrm{d}x\,\mathrm{d}y \\ &= \iint\limits_{-\infty}^{\infty} \left|C(f_x,f_y) - \widehat{C}(f_x,f_y)\right|^2 \mathrm{d}f_x\,\mathrm{d}f_y\,,\end{aligned}\tag{B.19}$$

where it has been used that $\arg U = \arg \widehat{U}$ and Parseval's theorem [86] has been used to provide the second equality. Interpreting the reformulated error metric, it is evident that minimizing the least square error in the Fourier domain of C minimizes the least square error of C as well.

Equivalent updating steps are derived in the appendix of [7], based on a second order Newton's method approach to reducing a least square error metric, indicating that the updating function is robust and suitable also for updating the slices of a multislice object. The suitability of the updating step is further backed up by referring to multiple publications that demonstrate successful usage of updating steps, equivalent or similar to $\mathcal{U}(\cdot)$, for recovery of 3D objects [5, 6, 15].

Appendix C

Multislice results by Tian and Waller

The figure displaying the 3D FP results of the stacked USAF targets from ref. [6] is reprinted here as Figure C.1 on the following page.

The finest resolvable element is element 4 og group 9 on the USAF target, corresponding to a full-pitch resolution of $1.38\,\mu$m. The raw images were collected using $\lambda = 643\,$nm and $NA_{\mathrm{obj}} = 0.10$ with angularly diverse illumination resulting in $NA_{\mathrm{illu}} = 0.41$ [6].
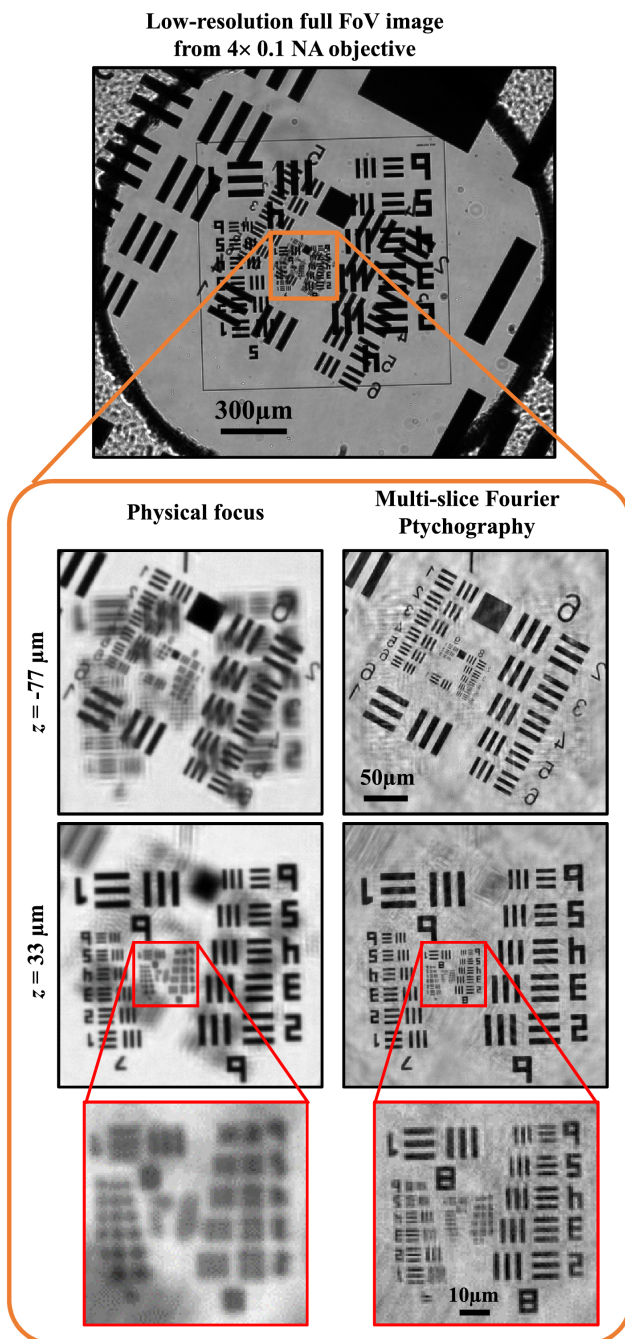
Figure C.1: Results obtained by Tian and Waller. Reprinted with permission from ref. [6], OSA publishing. The top part displays the full FoV of the microscope, and the lower part compares the multislice FP results with physical focusing.